University of Nottingham
UK | CHINA | MALAYSIA

Constraints on Primordial Black Hole Dark Matter from Wide Binaries in the Galactic Halo

Emily Sarah Tyler
Student ID: **14303635**

Thesis submitted to the University of Nottingham
for the degree of Doctor of Philosophy

November 2021

Acknowledgements

Firstly a big, big thank you to my supervisor Anne Green. I couldn't have done this without your support and compassion. Thank you for being encouraging on my slow weeks and assuring me that everything would come together. You taught me to trust my instincts and to be critical of everyone's reasoning, especially my own. Thank you also to Simon Goodwin, your advice and enthusiasm were invaluable.

A huge thanks to Tom Clarke, my inspiration. You have become one of my closest friends over the last few years, thank you for your endless emotional support and encouragement. You convinced me that this was possible.

Thank you to my family for never doubting that I could achieve anything I set out to do. Thank you Mum for your unwavering faith and infinite love. Dad, thank you for reminding me that space is actually interesting and trying to understand my work. Laura, thank you for being my best friend, my life is much brighter from having you in it.

James, thank you for everything you do. You've provided me with peace, comfort and understanding during an incredibly difficult few years. Thank you for all the fun and happiness you bring into my life.

Finally, Nanny and Grandad, this thesis is dedicated to you. I miss you both more and more every day. You have always been proud of me just as I am, and knowing how proud you would be of me now gives me so much courage. Thank you for your unconditional love.

Declaration

No part of this thesis has previously been submitted for a degree or other qualification at this or any other university.

Supervisors:	Prof. Anne Green
	Dr. Adam Moss
Examiners:	Dr. Will Sutherland (Queen Mary University of London)
	Prof. Clare Burrage (University of Nottingham)
Submitted:	15$^{\text{th}}$ November 2021
Examined:	14$^{\text{th}}$ January 2022
Final Version:	21$^{\text{st}}$ April 2022

Abstract

Primordial black holes (PBHs), black holes that are formed in the early Universe from the collapse of over-densities, are a candidate for non-baryonic cold dark matter. The fraction of dark matter made up of PBHs has been constrained using multiple mechanisms including evaporation, gravitational lensing, gravitational waves from mergers, large-scale structure, accretion and the disruption of wide binaries. In this thesis we review the work on wide binaries and improve the reliability of these constraints, primarily by introducing a more physically motivated initial semi-major axis distribution for our simulated binaries.

We used Monte Carlo simulations to implement halo wide binary encounters with PBHs over a period of 10Gyr. The binaries are placed in a sea of perturbers and encounters are calculated using the impulse approximation. Broken binaries are kept in the simulations and used to calculate constraints, since their peculiar velocities are similar enough to be mistaken for binary stars. Our simulation results are consistent with previous work for a log flat initial semi-major axis distribution, and when broken binaries are removed from the simulations.

We calculate constraints by using a modified χ^2 test to compare the simulated binary distribution with a catalog of observed binaries. A χ^2 test provides p-values whilst also quantifying the goodness of the best fit parameters. We use a modified version in order to correct for the small number of binaries used in the comparison. Our constraints are re-scaled to take into account the non-uniform dark matter density along the binary Galactic orbits. To find the value by which to re-scale the constraints, we calculate the time-averaged dark matter density along each binary orbit for which we have sufficient data.

Our final constraints are much weaker than those calculated previously, primarily due to the inclusion of unbound binaries and a more physically motivated semi-major axis distribution. These constraints are subdominant to previously calculated constraints from other effects such as microlensing, gravitational waves and accretion in the PBH mass range $1M_{\odot} - 1000M_{\odot}$, allowing PBHs to make up at least 20% of dark matter.

More detailed simulations are needed to find tighter constraints on the PBH mass fraction: simulations of the Galactic potential would take into account the Galactic tide and disk and the variable dark matter density. These constraints could also be made more reliable by using a larger catalog of binary stars, such as a subset of GAIA DR2.

Contents

List of Figures

List of Tables

Chapter 1

Introduction

In 1932, Oort measured the velocity dispersion of the stars in our local neighbourhood and estimated there to be almost twice as much mass than is visible, hypothesising the existence of dark matter [1]. Shortly after, in 1933, Fritz Zwicky estimated the mass of the Coma cluster using the viral theorem and, due to the constituent galaxies having too large peculiar velocities for the cluster to be gravitationally bound, found there to be around 400 times more mass than is observable, coining the term 'dark matter' to describe this invisible mass [2]. This ratio was confirmed in 1936 by Smith who measured the mass of the Virgo cluster [3]. Although we are certain that either dark matter exists, or Newtonian gravity is incorrect, almost 100 years later the exact nature of dark matter is still unknown.

The physics of the early Universe can provide some insight into the properties of dark matter by allowing us to calculate the fraction of matter that is made up of baryons. The nuclei of the light elements: deuterium, helium-3, helium-4, and lithium-7 were formed approximately 5 minutes after the Big Bang, once the Universe was cool enough for deuterium to survive and still hot enough for fusion to happen, this process is called Big Bang Nucleosynthesis (BBN). The abundance of these elements is dependent on multiple factors including the baryon-photon ratio. When the reaction rate of neutron-proton interactions became lower than the rate of expansion of the Universe, neutrons were no longer created but continued to decay with a mean life of ~ 880 seconds [4] before forming nuclei. This resulted in a final neutron-proton ratio of

1 : 7. From the primordial abundances of the light elements and the photon number density, which is calculable from the cosmic microwave background (CMB), it's possible to calculate the baryon density.

As well as being either baryonic or non-baryonic, dark matter can also be categorised as either hot (free streaming length much larger than a protogalaxy) or cold (free streaming length much smaller than a protogalaxy). The large free streaming length of hot dark matter (HDM) predicts top-down structure formation, i.e. large galaxy clusters first. However, predictions for cold dark matter (CDM) and simulations of structure formation with CDM [5, 6], where small structures form first, are consistent with the structure formation that we observe [7, 8]. Warm dark matter (WDM) has a free streaming length similar to the size of a protogalaxy, but while there are possible particle candidates for WDM and CDM (e.g. sterile neutrinos and Weakly Interacting Massive Particles, respectively), no particles that are known to exist qualify as either WDM or CDM.

The structure of this thesis is as follows, in this chapter I will briefly discuss the current evidence for dark matter, possible dark matter candidates, the formation of primordial black holes (PBHs), and in more detail the current constraints on PBH dark matter, the subject of this thesis. In Chapter 2 I cover necessary theory of wide binary disruption and orbital mechanics and the previous work on which we intend to improve. In Chapter 3 I describe our simulations in detail, starting with our approximations, stating our parameters and method, and finishing with our simulation results. Our final constraints are given in Chapter 4, along with how they were calculated and the details of the observational data we used. Our conclusions and suggestions for expanding on this work are summarised in Chapter 5.

1.1 Dark matter

In Sec. 1.1.1 I discuss the main evidence for the discovery of, and subsequent research on, dark matter, followed in Sec. 1.1.2 by a brief overview of the

current dark matter candidates.

1.1.1 Evidence for dark matter

Some of the earliest evidence for dark matter comes from the rotation curves of spiral galaxies [9, 10]. In this section I give the basic theory behind this evidence and describe some of the other evidence for dark matter that derives from gravitational interactions.

Galaxies

The orbital speed of stars and gas clouds can be measured from the Doppler shift of the Hydrogen 21cm line, which we can compare to predicted speeds calculated using Newton's laws of gravity. Newton's laws give a circular speed at radius r,

$$v_c = \sqrt{\frac{GM(<r)}{r}}, \tag{1.1}$$

where G is the gravitational constant and $M(<r)$ is the mass within radius r. At large r, luminosity density is observed to drop exponentially, so if stars dominate, the mass $M(<r)$ should be constant and we would expect to find $v_c \propto r^{-1/2}$. However, in reality, we find that the circular velocity is actually constant at large r, this implies that $M(<r) \propto r$ and therefore the mass density $\rho \propto r^{-2}$, if Newtonian gravity is correct. This invisible mass is dark matter. More evidence for dark matter from galaxies comes from the stability of spiral galaxies; self-gravitating disks require a spherical halo with a large velocity dispersion in order to form bars and remain stable [11].

Galaxy clusters

We can estimate the total mass of galaxy clusters using the virial theorem, which tells us that in a self-gravitating system the kinetic energy T and potential energy V are related by [see e.g. Ref. 12],

$$2T + V = 0. \tag{1.2}$$

We can measure the kinetic energy of the galaxies from their velocities by application of the Doppler effect, allowing us to estimate the mass of the cluster from its potential energy. This gives a mass-luminosity ratio of approximately,

$$\frac{M}{L} \sim 400 \frac{M_\odot}{L_\odot}, \tag{1.3}$$

where $M_\odot$ is the solar mass and $L_\odot$ is the solar luminosity. This ratio is equivalent to a mass density parameter (fractional density of matter in the universe relative to the critical density for a flat universe see Eq. (1.4)) $\Omega_\mathrm{m} \sim 0.3$ [e.g. Ref. 13].

The baryon fraction can be estimated from X-ray spectra and surface brightness measurements by assuming the gas is spherically symmetric and in hydrostatic equilibrium. This gives an estimated baryon fraction of $f_b \sim 0.144 \pm 0.005$ [14].

We can also find the mass distribution in a galaxy cluster by observing gravitational lensing from background galaxies. The positions and intensities of the images lensed by the galaxy cluster give information on the clusters' mass distribution [15]. In merging clusters, like the bullet cluster, hot X-ray emitting gas from the colliding subcluster interacts with the main cluster and lags behind. This gas is the dominant baryonic matter component, so in the absence of dark matter, the gravitational potential of the cluster is expected to follow the distribution of the gas. However, if the cluster mass is dominated by non-baryonic dark matter, which is assumed to be collisionless and therefore follows the galaxies during the collision, the cluster potential will also follow the distribution of the galaxies. Clowe et al. [16] find that the mass is concentrated around the galaxies in the cluster and subcluster implying that they must contain a significant amount of non-baryonic dark matter.

CMB anisotropies

Once the temperature of the Universe dropped sufficiently for protons and electrons to form neutral Hydrogen atoms, the Universe became transparent. The

photons from this time are still propagating through the Universe, although their wavelength has increased due to its expansion. This background radiation is called the Cosmic Microwave Background (CMB) and it encodes a large amount of information about the early Universe in the amplitude and angular power spectrum of its temperature fluctuations. The temperature anisotropies allow us to measure the matter and baryon density parameters. The density parameter for component i is defined as,

$$\Omega_i \equiv \frac{\rho_i}{\rho_c} = \frac{8\pi G\rho_i}{3H^2}, \tag{1.4}$$

where ρ_i is the mass density or equivalent energy density of component i, ρ_c is the critical density: the total density required for the Universe to be flat, G is the gravitational constant, and H is Hubble's constant.

It is possible to conclude that there must be non-baryonic dark matter from the amplitude of the CMB temperature fluctuations. Baryons are tightly coupled to photons until decoupling so baryon perturbations can only grow after decoupling. Non-baryonic dark matter perturbations, however, can start growing sooner, and for temperature fluctuations to grow enough from their initial value, there must be some non-baryonic dark matter.

The angular power spectrum of the CMB is a measure of how correlated any two given points are as a function of their angular separation in the sky. We can infer different information about the early Universe by studying different features in the power spectrum, such as the acoustic peaks which relate to the scale of primordial fluctuations. This scale is related to the baryon acoustic oscillations (BAOs), which are a measure of how far sound waves were able to travel in the baryon-photon plasma. BAOs are caused by the competing forces of gravity and pressure.

Table 1.1 gives the density parameters for the total matter (Ω_{m}), baryonic matter (Ω_{b}) and cold dark matter (Ω_{c}), measured by the Planck Collaboration [17]. These parameters are found by combining CMB temperature, polarisation and gravitational lensing data. By comparing the values of Ω_{c} and Ω_{b} we

Parameter	68% limits
$\Omega_{\rm m}h^2$	0.1430 ± 0.0011
$\Omega_{\rm b}h^2$	0.0224 ± 0.0001
$\Omega_{\rm c}h^2$	0.120 ± 0.001

Table 1.1: The density parameter Ω (defined in text) for the total matter (m) and separate baryonic (b) and cold dark matter (c) components, as measured by the Planck Collaboration [17]. The Hubble parameter is $H = 100h$ km s^{-1} Mpc^{-1}.

can see that the majority of dark matter must be non-baryonic.

Large scale structure

The DES Collaboration [18] [as well as e.g. Refs. 19–21] analysed data from the first three years of the Dark Energy Survey to constrain structure formation in the late Universe. By combining the effects of cosmic shear, galaxy clustering and galaxy-galaxy lensing they were able to determine that the mass density parameter is $\Omega_{\rm m} = 0.34 \pm 0.03$. Cosmic shear is the distortion of the shapes of background galaxies because of weak gravitational lensing of light between the sources and observer [22, 23], the galaxy two-point correlation function measures the spatial clustering of galaxies [24, 25], and galaxy-galaxy lensing is the cross-correlation of lensed galaxy positions and source galaxy shapes [26]. Combining these three effects calibrates many of the systematic parameters in the model allowing constraints on cosmological parameters to be calculated.

Modified gravity

All of this evidence relies on Newtonian gravity. While Newton's laws are thoroughly tested on small scales [e.g. Ref. 27] they could be different on cosmological scales and these differences could explain the above measurements without the need for dark matter.

The first theory of modified gravity, Modified Newtonian Dynamics (MOND), was formulated by Milgrom in 1983 [28]. This theory was introduced in order to explain galaxy rotation curves without dark matter. Since then, MOND has been found to explain several galactic phenomena, such as the core-cusp problem (inferred DM density profiles of low-mass galaxies are inconsistent

with N-body simulations) [29] and the missing baryons problem (the present-day density of baryons is much smaller than that predicted by BBN) [30], that currently have no solution in the current CDM cosmological model (ΛCDM). Recent tests have found that the tidal forces of neighbouring galaxies in ΛCDM aren't strong enough to explain external field effects, the external force felt by a self-gravitating system, predicted by MOND [31]. However, one large issue with MOND is its inability to explain all unseen mass in galaxy clusters [32]. See [e.g. Refs. 33, 34] for more information on MOND.

The first complete relativistic formulation of MOND is Tensor–vector–scalar gravity (TeVeS) [35]. Being relativistic allows TeVeS to accommodate gravitational lensing, however, recent gravitational wave observations from the merger of two neutron stars (GW170817) [36] and a gamma ray burst ~ 2 seconds later from the same location (GW170817a) [37] can be used to put constraints on TeVeS, which predicts a difference between the speed of gravity and the speed of light [38]. This doesn't rule out other modified gravity theories, including some based on TeVeS, that allow gravitational waves to propagate as they do in general relativity.

1.1.2 Dark matter candidates

There are a variety of different objects and particles that could make up some or all of the dark matter. These candidates include known astronomical objects, new particles and known particles that have sufficiently low interactivity.

Non-particle dark matter

Massive Compact Halo Objects (MACHOs) are massive, low luminosity objects that could make up the missing mass in galaxies while being dark enough to not have been detected. They consist of faint stellar remnants, brown dwarfs, planets, rocky debris or primordial black holes (PBHs). Since most of these objects are baryonic, the only MACHO that could make up a significant amount of dark matter is PBHs. PBHs are non-baryonic because they form

before matter-radiation equality. In 1985, Bahcall et al. [39] investigated the effect of MACHOs on wide binaries in the Galactic halo and found that the maximum allowed MACHO mass was $2M_\odot$. In this thesis we will be expanding on their work and the work that followed it.

There has been renewed interest in PBH dark matter since LIGO detected gravitational waves from merging black holes in 2016 [40, 41]. Sasaki et al. [42] found that if dark matter consists of black holes with the mass that was detected ($\sim 30M_\odot$), the merger rate of the black holes would be larger than the rate inferred by LIGO, but PBHs could make up a fraction of dark matter. See Sec. 1.2.1 for a brief overview of PBH formation methods and Sec. 1.2.2 for current PBH constraints.

WIMPs

Weakly Interacting Massive Particles (WIMPs) are heavy, stable, weakly coupled particles that are assumed to self-annihilate. The main motivation for WIMPs comes from the WIMP miracle: the relic dark matter density estimated from the time of WIMP freeze-out is consistent with the measured dark matter density [43–46]. Supersymmetry requires that the lightest supersymmetric particle must be stable in order for protons to be stable, making this particle an excellent WIMP candidate [47]. As of today, however, WIMPs have not been detected, see Arcadi et al. [48] for the current state of WIMP research.

Neutrinos

The small interaction cross-section of neutrinos makes them a possible HDM candidate. Current limits from experiments that constrain the neutrino mass place an upper limit on the density parameter of neutrinos, $\Omega_\nu \lesssim 0.14$ [49]. A tighter bound has also been found using Planck CMB temperature anisotropies and baryon acoustic oscillations data, while assuming the ΛCDM model in a flat universe: $\Omega_\nu h^2 \lesssim 0.0016$ [50, 51].

Another type of neutrino, sterile neutrinos, are semi-relativistic making them a WDM candidate. They are a fourth, heavier species of neutrino with no electroweak interaction. WDM forms large scale structure more consistent with observations than HDM. Possible formation mechanisms for sterile neutrinos exist, such as the freeze-in mechanism [52], where coupling to a particle in the thermal bath results in a gradual increase in the sterile neutrino abundance. The random motions of WDM erase perturbations smaller than the free streaming length and therefore structure formation on scales smaller than,

$$M_{\rm h} \sim 10^{10} \left(\frac{M_{\rm wdm}}{1{\rm keV}} \right)^{-3.33} M_{\odot}, \tag{1.5}$$

where $M_{\rm h}$ is the minimum halo mass and $M_{\rm wdm}$ is the mass of the WDM particles. The power spectrum for semi-relativistic dark matter can be probed with the Lyman-α forest which gives constraints on the mass of WDM. See Ref. [53] for details on the constraints on WDM.

Axions

Axions are another particle dark matter candidate, they are slow-moving low-mass bosons with multiple formation mechanisms that are consistent with the known dark matter abundance, such as early Universe phase transitions [54]. They can be detected by a coupling to electromagnetism that converts them to photons. Axions arise naturally from a solution to the strong CP problem: the upper limit on the neutron electric dipole moment predicts that very little charge-parity violation happens, but there is no known physical reason for this to be the case. Requiring that charge-parity symmetry is conserved solves the strong CP problem and results in a new particle: the axion. The non-detection of WIMPS has lead to axions becoming a popular particle dark matter candidate. See e.g. Ref. [55] for more details.

1.2 PBHs as Dark Matter

PBHs are black holes which may form in the early Universe through multiple mechanisms including the collapse of over-dense regions, cosmic string loops and collisions of bubbles formed in phase transitions [see e.g. Refs. 56–59]. Unlike black holes formed due to astrophysical processes, which form with a minimum mass of order $1M_\odot$, PBHs can form with much smaller masses, in principle down to the Planck mass $\sim 10^{-5}$g. The most straightforward method for PBH formation, from the collapse of large overdensities, is described in Sec. 1.2.1 and the current constraints on the PBH abundance are summarised in Sec. 1.2.2.

1.2.1 PBH formation

The simplest PBH formation method is the collapse of density perturbations during radiation domination. The following theory is from Carr [60]. Primordial density perturbations are produced during inflation from the quantum fluctuations of scalar fields. The value above which an over-density $\delta \equiv \delta\rho/\rho$ will form a PBH in the comoving gauge is δ_c, where δ_c is equal to the sound speed squared. During radiation domination, $\delta_c = 1/3$. The mass of the PBH, $M_{\rm PBH}$, formed by this method is of order the mass within the Hubble radius at the time of collapse, this mass, called the Horizon mass, is given by,

$$M_H = \frac{4\pi}{3}\rho(H^{-1})^3 = \frac{1}{2GH}, \tag{1.6}$$

where the second equality comes from the Friedmann equations: $H^2 = \frac{8\pi G}{3}\rho$. During radiation domination, the scale factor $a \propto t^{1/2} \Rightarrow H = 1/(2t)$, which gives,

$$M_{\rm H} \sim \frac{t}{G} \sim 10^{15}{\rm g}\left(\frac{t}{10^{-23}s}\right). \tag{1.7}$$

A PBH with mass of order one solar mass ($M_\odot = 2 \times 10^{30}$g) would be formed around the QCD phase transition ($t \sim 10^{-6}$s). Simulations such as those by Nadezhin et al. [61] have confirmed this result.

Carr [60] also calculated the initial abundance of PBHs,

$$\begin{aligned}\beta(M_{\rm H}) &\equiv \frac{\rho_{\rm PBH}}{\rho_{\rm tot}},\\ &= \int_{\delta_c}^{\infty} P(\delta)\mathrm{d}\delta,\\ &= \mathrm{erfc}\left(\frac{\delta_{\rm c}}{\sqrt{2}\sigma(\mathrm{M_H})}\right),\\ &\approx \sigma(M_{\rm H})\exp\left(-\frac{\delta_c^2}{2\sigma^2(M_{\rm H})}\right),\end{aligned} \tag{1.8}$$

by assuming that the probability distribution of the primordial density perturbations, $P(\delta)$, is Gaussian with variance $\sigma^2(M_{\rm H})$. In order to satisfy the constraints on the initial abundance of PBHs, $\sigma^2(M_{\rm H}) \ll \delta_c^2$.

The variance of the density perturbations, $\sigma^2(M)$, is a measure of the typical size of matter density fluctuations at a mass scale M, and is given by,

$$\sigma^2(M) = \frac{1}{2\pi^2}\int \mathrm{d}k\ k^2\tilde{W}(kR(M))P(k), \tag{1.9}$$

where $\tilde{W}(kR(M))$ is the Fourier transform of the window function with size $R(M)$, containing mass M, used to smooth the density contrast and $P(k)$ is the power spectrum of the primordial perturbations. The mass variance on cosmological scales is measured to be of order 10^{-5} [62]. For a scale invariant power spectrum this leads to an extremely small initial PBH abundance, $\beta(M_{\rm PBH}) \sim \exp(-10^8)$.

The initial PBH mass function is related to the current PBH density parameter, $\Omega_{\rm PBH}$, by,

$$\beta(M_{\rm PBH}) \equiv \frac{\rho^i_{\rm PBH}}{\rho^i_c} = \frac{\rho^{\rm eq}_{\rm PBH}}{\rho^{\rm eq}_c}\left(\frac{a_i}{a_{\rm eq}}\right) \approx \Omega_{\rm PBH}\left(\frac{a_i}{a_{\rm eq}}\right), \tag{1.10}$$

where a is the scale factor, 'i' refers to the time at which PBHs formed and 'eq' refers to matter-radiation equality. The equality in this equation comes from the fact that the density of PBHs is proportional to a^{-3}, and before matter-radiation equality, the critical density is proportional to a^{-4}. In terms of the

fraction of dark matter made up of PBHs, this approximately evaluates to,

$$f_{\rm PBH} \equiv \frac{\Omega_{\rm PBH}}{\Omega_{\rm CDM}} \sim 2\beta_{\rm eq}(M_{\rm PBH}), \tag{1.11}$$

where $\beta_{\rm eq}(M_{\rm PBH})$ is the abundance of PBHs with mass $M_{\rm PBH}$ at matter-radiation equality.

1.2.2 Current PBH constraints

The current constraints on the fraction of dark matter made up of PBHs as a function of their mass are summarised in Fig. 1.1 and briefly described in this section.

Evaporation

PBHs evaporate by emitting Hawking radiation, and would have evaporated by the present day if their initial mass $M_{\rm PBH}$ is less than $M_* \approx 5 \times 10^{14}$g [63, 64]. More constraints have been made based on the expected evaporation products [65], the damping of CMB anisotropies due to energy injection during recombination [66, 67], heating of neutral hydrogen [68] and heating of the interstellar medium in dwarf galaxies [69]. One of the tighter constraints due to evaporation is from the extragalactic gamma-ray background, $f_{\rm PBH} \lesssim 2 \times 10^{-8}(M_{\rm PBH}/M_*)^{(3+\epsilon)}$, where $\epsilon \sim 0.1 - 0.4$ is a parameter for the energy dependence of the gamma-ray intensity [58, 70]. This constraint can be made tighter by a factor of $\mathcal{O}(10)$ by considering the effects of blazars and other known astrophysical sources [71].

Gravitational lensing

When a compact object crosses the line of sight of a background object, distorted images of the background object can be observed. The brightness of these images and the duration of the lensing event is dependent on the mass of the foreground object and the relative velocity between the background and foreground objects. PBHs would provide gravitational lenses for observations of stars, the number and durations of the observed lensing events can provide

constraints on the halo fraction of PBHs.

The strongest constraints in the $\sim 1M_\odot$ mass range are from microlensing surveys of stars in the small and large Magellanic clouds: the EROS survey gives an upper limit on the density fraction of compact objects of $f_{\rm PBH} < 0.1$ for objects with mass $10^{-6} \lesssim M_{\rm CO}/M_\odot \lesssim 1$ and a stronger limit on PBHs with mass $< 10M_\odot$, which cannot make up more than 40% of dark matter [72]. Alcock et al. [73] searched for long duration (> 150 days) microlensing events in the MACHO data, after finding no such events they conclude that compact objects with mass $M_{\rm CO} \lesssim 30M_\odot$ cannot make up the bulk of dark matter. The more recent microlensing surveys OGLE-III and OGLE-IV give tighter constraints for slightly smaller mass objects, with the mass fraction of compact objects limited to $f_{\rm PBH} \lesssim 10^{-2}$ for objects with mass $M_{\rm CO} \sim 10^{-3}M_\odot$ [74, 75].

Niikura et al. [76] made observations of lensing events with duration $0.1-1$ hours in Andromeda with the Subaru Hyper Suprime-Cam (HSC). They only found one candidate lensing event in their 7 hour observation, which provides a strong constraint on PBHs with mass $10^{-11} < M_{\rm PBH}/M_\odot < 10^{-6}$, only allowing 1% of dark matter to be made up of PBHs with masses in this range. Niikura et al. [76] use a source size of one solar radius, but Smyth et al. [77] point out that sources are likely to be larger than this. Taking source size into account weakens the constraints from Niikura et al. [76], allowing PBHs to make up dark matter for masses below $10^{-10}M_\odot$ rather than $10^{-11}M_\odot$.

Gravitational waves from mergers

PBHs can form binaries when two of them decouple from the Hubble expansion before matter-radiation equality. These PBH binaries can be made highly eccentric by three body interactions, and when the black holes coalesce they produce gravitational waves that can be detected by LIGO-Virgo [78–80]. Using these measurements and assuming that the PBH binaries aren't disrupted, constraints on the density fraction of PBHs have been calculated,

$f_{\rm PBH} < \mathcal{O}(10^{-3})$ for $10 \lesssim M_{\rm PBH}/M_\odot \lesssim 300$ [42, 81–83].

Dynamical

Wide binaries in the Galactic halo are susceptible to disruption by PBHs, their survival provides constraints on the mass fraction of PBHs in the halo [84–86]. This thesis focuses on making these constraints more reliable through more detailed models of binary disruption.

Brandt [87] gives a limit based on observations of a star cluster near the centre of the ultra-faint dwarf galaxy Eridanus II which has not been disrupted by halo objects, this constraint excludes objects with mass larger than $5M_\odot$ making up all of dark matter. The stars in ultra-faint dwarf galaxies would also be subject to dynamical heating from MACHOs, increasing the size and velocity dispersion of the galaxies. The sizes of these galaxies puts an independent limit on MACHO dark matter with mass $\gtrsim 10M_\odot$.

The existence of PBHs in dwarf galaxies would alter their stellar distribution, leading to a reduction in the number of stars at the centre of the galaxy and a ring in the projected stellar surface density profile, from this effect Koushiappas and Loeb [88] find that $f_{\rm CO} < 0.6$ for compact objects with mass $M_{\rm CO} = 30M_\odot$.

Large-scale structure

Poisson fluctuations in the PBH number density would affect the formation of large-scale structure. Observations of the Lyman-α forest provide constraints on the mass of PBHs in the range $10^4 - 10^{10}M_\odot$ using this effect [89, 90].

Accretion

Radiation from accreting black holes deposits energy into the photon-baryon plasma in the early universe, this affects the statistical properties of the CMB allowing constraints on the abundance of black holes to be calculated. The main effect of the energy injections is to increase the free electron fraction, this is visible in the CMB power spectrum as a damping of fluctuations on

small angular scales due to photon scattering out of the line of sight [91–94]. These constraints are very tight for PBH masses above $\sim 10^2 M_\odot$, effectively ruling out PBHs in this mass range, but they are much less tight for masses $\sim 1 M_\odot$.

See Fig. 1.1 for a summary of the current constraints. Solar mass black holes are ruled out as all of dark matter, assuming a delta-function mass distribution and that they are smoothly distributed. Since PBHs are discrete objects there will be Poisson fluctuations in their distributions, it has also been shown that local non-Gaussianity in the primordial perturbations can cause increased clustering in the initial PBH distribution [95–97]. The mass of a PBH depends on multiple factors including the size of the fluctuation from which it forms [98, 99] and the horizon mass at formation time. If the primordial power spectrum has a finite width peak, PBHs could form at a range of times leading to a range of formation masses. Figure 1.1 assumes that all PBHs have the same mass, this assumption is unrealistic but practical, and it is possible to convert single mass constraints into extended mass function constraints [57]. The constraints from a log normal PBH mass function [See Ref. 57, Fig. 20] are more spread out, reducing the amount of parameter space that is allowed for PBHs to make up all of DM, but less restrictive at their tightest point. The largest open window in Fig. 1.1 is the asteroid-mass window ($5 \times 10^{-16} < M_{\rm PBH}/M_\odot < 5 \times 10^{-11}$), which cannot be constrained by the disruption of wide binaries.

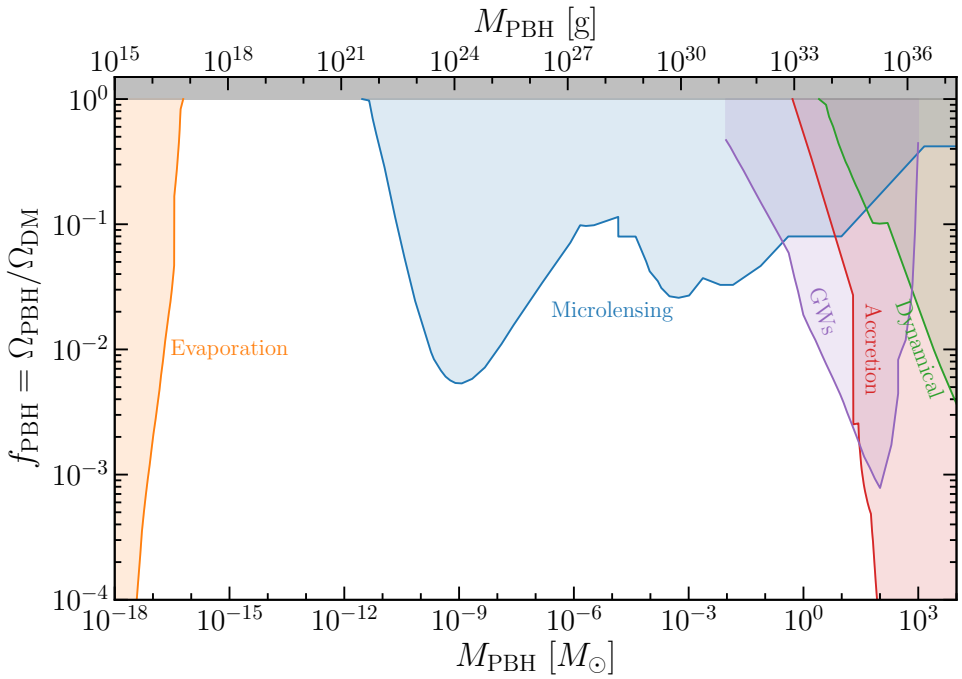

Figure 1.1: From Green and Kavanagh [56]. Current constraints on the fraction of dark matter made up of PBHs, $f_{\rm PBH}$, as a function of the PBH mass $M_{\rm PBH}$. Shaded regions are excluded. These constraints were calculated by multiple methods and sorted into evaporation, microlensing, GWs, accretion and dynamical constraints. See text for more information on these constraints.

Chapter 2

Background

In this chapter I will cover the basics of orbital mechanics (Sec. 2.1), how these theoretical quantities relate to measurable quantities that we can observe (Sec. 2.2), the relevant theory of the disruption of binary systems by perturbers (Sec. 2.3) and previous work on wide binary disruption (Sec. 2.4).

2.1 Orbital mechanics

Here I will give a brief overview of the equations of motion of binary stars. Most of the equations and methods in this section are from Chapter 2 of Murray and Dermott [100]. The binary equation of relative motion in the centre of mass frame is,

$$\frac{\mathrm{d}^2\mathbf{r}}{\mathrm{d}t^2} + \mu\frac{\mathbf{r}}{r^3} = 0, \tag{2.1}$$

where $\mathbf{r}$ is the relative position of the two stars at time t, $r = |\mathbf{r}|$ and $\mu = GM_\mathrm{b}$, where G is the gravitational constant and M_b is the total mass of the binary. This equation is derived using Newton's third law and Newton's law of gravitation,

$$\ddot{\mathbf{r}} = \ddot{\mathbf{r}}_2 - \ddot{\mathbf{r}}_1 = -\frac{GM_1}{r^3}\mathbf{r} + -\frac{GM_2}{r^3}\mathbf{r}. \tag{2.2}$$

where M_1 and M_2 are the masses of the two binary components and dots denote differentiation with respect to time.

We can take the cross product of $\mathbf{r}$ with Eq. (2.2) and integrate to find a constant vector,

$$\mathbf{h} = \mathbf{r} \times \dot{\mathbf{r}}. \tag{2.3}$$

The motion of the binary is therefore in a plane perpendicular to the vector **h**, which is related to the binary's angular momentum. Changing to polar coordinates and substituting in $u = 1/r$ and $h = r^2\dot{\theta}$ gives,

$$\frac{\mathrm{d}^2u}{\mathrm{d}\theta^2} + u = \frac{\mu}{h^2}, \tag{2.4}$$

which has the general solution,

$$u = \frac{\mu}{h^2}\left(1 + e\cos(\theta - \varpi)\right), \tag{2.5}$$

where e and ϖ are two constants of integration. Substituting for r we find the general solution for an orbit in polar coordinates,

$$r = \frac{p}{1 + e\cos(\theta - \varpi)}. \tag{2.6}$$

This is the equation of a conic section where e is the eccentricity and $p = h^2/\mu$ is the semilatus rectum. This equation can represent 4 differently shaped orbits [100]:

circle:	$e = 0$,	$p = a$;
ellipse:	$0 < e < 1$,	$p = a(1 - e^2)$;
parabola:	$e = 1$,	$p = 2q$;
hyperbola:	$e > 1$,	$p = a(e^2 - 1)$;

where a is the semi-major axis and q is the distance to the central mass at closest approach. Given the phase of the binary, $\theta - \varpi$, we can now calculate the separation of the binary r. The relation between Eq. (2.6) and the x and y coordinates of the binary stars is given in Sec. 3.3.5.

In this thesis we refer to 'bound' binaries and 'unbound' binaries. Bound binaries are those with $e < 1$ and are on periodic orbits, while unbound binaries have $e \geq 1$ and are on hyperbolic or parabolic orbits. Most work on wide binary disruption only considers bound binaries, however we will include unbound binaries and check whether or not they are necessary to simulate. They might be necessary if unbound binaries are likely to become rebound in

subsequent encounters with PBHs or if binaries that are unbound at the end of the simulation have very similar peculiar velocities and could be mistaken for bound binaries by observations.

The true anomaly is defined as $f = \theta - \varpi$, and the mean motion is $n = 2\pi/T$, where T is the period of the binary, making the mean motion the average angular velocity. Having defined the mean motion, we can write Kepler's third law as,

$$\mu = n^2 a^3. \tag{2.7}$$

and the constant of motion, h, can be written as,

$$h^2 = na^2\sqrt{1-e^2}. \tag{2.8}$$

in the case of an elliptical orbit. Differentiating Eq. (2.6) we find the relative velocity of the binary stars in an elliptical orbit,

$$V^2 = \mu\left(\frac{2}{r} - \frac{1}{a}\right). \tag{2.9}$$

This gives us an expression for the energy constant of the binary,

$$C = \begin{cases} -\frac{\mu}{2a}, & \text{for} \quad 0 \leq e < 1, \\ 0, & \text{for} \quad e = 1, \\ \frac{\mu}{2a}, & \text{for} \quad e > 0. \end{cases} \tag{2.10}$$

In order to create virtual binary stars we need to be able to randomise the phase, for this we need the mean anomaly. The mean anomaly is a 2π periodic function that is a linear function of time defined as,

$$M = n(t - \tau), \tag{2.11}$$

where τ is the time of pericentre passage. When we generate binaries for our simulations we will randomise the mean anomaly, M, uniformly between 0 and 2π, this will randomise the phase correctly, taking into account the fact that binaries on elliptical orbits are more likely to be found with separations larger

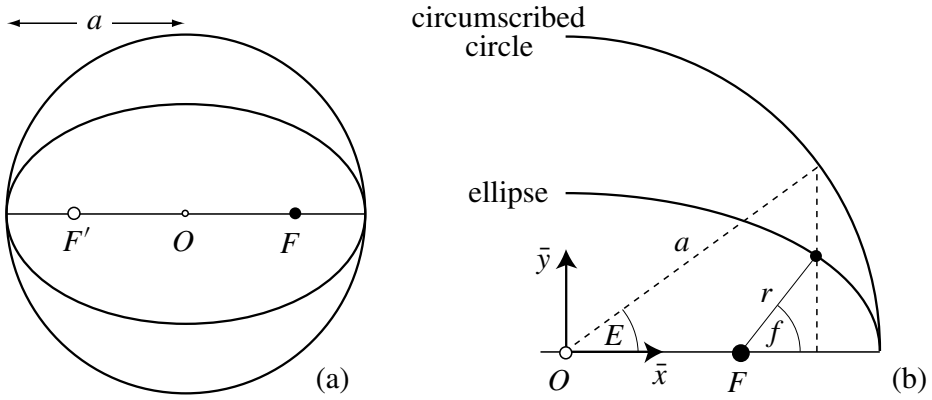

Figure 2.1: From Murray and Dermott [100]. (a) An elliptical binary orbit in the rest frame of one of the binary components. The stationary star is at the focus of the ellipse F, while the other binary star moves along the ellipse with semi-major axis a, equal to the radius of the concentric circle. (b) The relationship between the true anomaly f and the eccentric anomaly E.

than their semi-major axis. The mean anomaly is related to the eccentric anomaly, E, which is a physical angle, by Kepler's equation,

$$M = E - e \sin E, \tag{2.12}$$

and the true anomaly by,

$$\tan \frac{f}{2} = \sqrt{\frac{1+e}{1-e}} \tan \frac{E}{2}. \tag{2.13}$$

The relationship between the true and eccentric anomalies is shown in Fig. 2.1.

We will also need to calculate a binary's parameters after an encounter with a PBH by inverting some of the above equations. From Eq. (2.9), which gives the relation between the distance between the two binary stars r, and its rate of change V,

$$a = \left(\frac{2}{r} - \frac{V^2}{G M_\mathrm{b}} \right)^{-1}, \tag{2.14}$$

and from Eqs. (2.8) and (2.14),

$$e = \sqrt{1 - \frac{h^2}{G M_\mathrm{b} a}}. \tag{2.15}$$

The constants h and C (Eqs. (2.8) and (2.10)) are related to the total angular

momentum L and total energy of the system $\mathcal{E}$ by,

$$h = \left(\frac{1}{M_1} + \frac{1}{M_2}\right) L, \quad C = \left(\frac{1}{M_1} + \frac{1}{M_2}\right) \mathcal{E}, \tag{2.16}$$

Eq. (2.15) can be rewritten as,

$$e = \sqrt{1 + \frac{2M_{\rm b} L^2 \mathcal{E}}{G^2 M_1^3 M_2^3}}, \tag{2.17}$$

and we can find the semi-major axis using Eq. (2.10),

$$a = \frac{G M_1 M_2}{2|\mathcal{E}|}. \tag{2.18}$$

These equations allow us to calculate the new semi-major axis and eccentricity of a binary after an encounter with a PBH and also demonstrate the link between semi-major axis and energy; and the link between eccentricity and angular momentum. Note that an initial eccentricity distribution uniform in e^2 is equivalent to a uniform initial energy distribution.

2.2 Observable quantities

The directly measurable quantity for binary separation is the angular separation, Δs, the angle between the two binary stars in the sky. This can be converted into the projected separation, $r_{\rm proj}$, from the distance to the binary d,

$$\frac{r_{\rm proj}}{\rm au} = \frac{d}{\rm parsec} \times \frac{\Delta s}{\rm arcsec}. \tag{2.19}$$

The physical binary separation r can then be calculated from the projected separation by choosing a random orientation for the binary. I discuss which of these quantities is best for comparing observations with simulations in Sec. 4.4.

2.3 Wide binary disruption

The key approximation used in studies of wide binary disruption is the impulse approximation, described in Sec. 2.3.1, which is very accurate in the regime of large binary semi-major axes and provides a huge simplification to the gravi-

tational encounters between a compact object and binary star. In Sec. 2.3.2, I calculate estimates for the timescales over which we expect binaries to be disrupted and describe the two main regimes into which wide binary encounters with compact objects can be divided. Newtonian gravity is sufficient for these encounters because the impact parameter is always much larger than the Schwarzschild radius of the PBHs.

2.3.1 Impulse approximation

If the relative velocity between the PBH and the binary is much larger than the orbital velocities of the binary stars, we can assume that the stars are stationary during the encounter. This is the impulse approximation and it allows us to use simple equations to calculate the effect of an encounter rather than N-body simulations. The impulse approximation is used in all previous work on binary disruption that we discuss in this thesis [39, 84–86, 101, 102]. Note that this approximation is valid for any compact object but we are only interested in PBHs here.

When the impulse approximation is valid, only the velocities and not the positions of the stars are changed. The equations for the perpendicular and parallel velocity changes for star i ($i = 1, 2$) are given by Binney and Tremaine [12, Eq. (3.54)]:

$$\boldsymbol{\Delta V}_{\perp,i} = \frac{2M_{\rm p}V_{\rm rel}}{M_{\rm p}+M_i}\frac{b_i/b_{90,i}}{1+b_i^2/b_{90,i}^2}\frac{\mathbf{b}_i}{b_i}, \tag{2.20}$$

$$\boldsymbol{\Delta V}_{\parallel,i} = \frac{2M_{\rm p}V_{\rm rel}}{M_{\rm p}+M_i}\frac{1}{1+b_i^2/b_{90,i}^2}\frac{-\mathbf{V}_{\rm rel}}{V_{\rm rel}}, \tag{2.21}$$

where $M_{\rm p}$ is the PBH mass, M_i is the mass of star i, $\mathbf{V}_{\rm rel}$ is the velocity of the PBH, $\mathbf{b}_i$ is the impact parameter vector for star i and $b_{90,i}$ is the 90° deflection radius for star i,

$$b_{90,i} \equiv \frac{G(M_{\rm p}+M_i)}{V_{\rm rel}^2}, \tag{2.22}$$

the impact parameter at which the angle of deflection is 90°. For all encounters considered here,

$$\frac{b_i}{b_{90,i}} \gg 1, \tag{2.23}$$

therefore the change in velocity of star i parallel to the motion of the PBH, $\mathbf{\Delta V}_{\parallel,i}$, is negligible and the change in velocity perpendicular to the PBH becomes,

$$\mathbf{\Delta V}_{\perp,i} = \frac{2GM_\mathrm{p}}{V_\mathrm{rel} b_i} \frac{\mathbf{b}_i}{b_i}, \tag{2.24}$$

which is the same as equations used in previous work [e.g. Ref. 101, Eq. (3)].

This change in velocity leads to a change in the binary energy [101, Eq. (4)],

$$\Delta\mathcal{E} = \mathbf{V} \cdot (\Delta\mathbf{V}_1 - \Delta\mathbf{V}_2) + \frac{1}{2}|\Delta\mathbf{V}_1 - \Delta\mathbf{V}_2|^2, \tag{2.25}$$

where $\mathbf{V} = \mathbf{V}_1 - \mathbf{V}_2$ is the relative velocity between the two binary stars.

Weinberg et al. [101] calculate the average value of $\Delta\mathcal{E}$ for two cases: the single kick limit where $b \ll a$ and the tidal limit where $b \gg a$. In the single kick limit the velocity change applies predominantly to one of the binary components, whereas in the tidal limit the total energy change is dependent on the difference between the velocity changes experienced by the two stars. The direction from which the perturber approaches the binary is completely randomised, this makes the direction of the velocity kick, $\Delta\mathbf{V}_1 - \Delta\mathbf{V}_2$, uncorrelated with the direction of the binary's orbit $\mathbf{V}$. Given that this is the case, when averaging over $\Delta\mathcal{E}$ the first term in Eq. (2.25) averages to zero. The average energy change is [101],

$$\langle\Delta\mathcal{E}\rangle = \begin{cases} 2\left(\frac{GM_\mathrm{p}}{bV_\mathrm{rel}}\right)^2, & \text{for } b \ll a, \\ \frac{7}{3}\left(\frac{GM_\mathrm{p}}{bV_\mathrm{rel}}\right)^2 \left(\frac{a}{b}\right)^2, & \text{for } b \gg a. \end{cases} \tag{2.26}$$

In Sec. 3.2.1, I test the accuracy of the impulse approximation, and in Sec. 3.5.1, I test the accuracy of Eq. (2.26) for a variety of impact parameter values including $b \sim a$.

2.3.2 Diffusive and catastrophic encounters

Encounters between a perturber and binary star can be divided into two regimes: diffusive, where binary evolution is determined by the cumulative effects of multiple encounters; and catastrophic, where the binary is broken by

a single encounter.

To find the disruption rate in either regime, we first need to find the rate at which binaries interact with perturbers. The encounter rate, $\dot{C}$, at an impact parameter between b and $b + \mathrm{d}b$ and with relative velocity between V_{rel} and $V_{\mathrm{rel}} + \mathrm{d}V_{\mathrm{rel}}$ is given by [12, Eq. (8.47)],

$$\dot{C} = n_p V_{\mathrm{rel}} 2\pi b \, \mathrm{d}b \, \mathrm{d}P, \tag{2.27}$$

where n_p is the number density of PBHs and $\mathrm{d}P$ is the probability that the binary star and PBH have relative velocity between V_{rel} and $V_{\mathrm{rel}} + \mathrm{d}V_{\mathrm{rel}}$.

We use an isotropic Maxwellian velocity distribution for the velocities of the PBHs and for the centre of mass velocities of the binary stars. The relative velocity distribution is then given by [12, Eq. (8.46)]:

$$\mathrm{d}P = \frac{4\pi V_{\mathrm{rel}}^2 \, \mathrm{d}V_{\mathrm{rel}}}{\left(2\pi\sigma_{\mathrm{rel}}^2\right)^{3/2}} \exp\left(-\frac{V_{\mathrm{rel}}^2}{2\sigma_{\mathrm{rel}}^2}\right), \tag{2.28}$$

where σ_{rel} is the relative velocity dispersion which is found by adding the velocity dispersions of the two populations in quadrature. Therefore Eq. (2.27) becomes [12, Eq. (8.47)],

$$\dot{C} = \frac{2\sqrt{2\pi} n_p b \, \mathrm{d}b}{\sigma_{\mathrm{rel}}^3} \exp\left(-\frac{V_{\mathrm{rel}}^2}{2\sigma_{\mathrm{rel}}^2}\right) V_{\mathrm{rel}}^3 \, \mathrm{d}V_{\mathrm{rel}}. \tag{2.29}$$

The following theory, from Binney and Tremaine [12], assumes the distant tide approximation ($b \gg a$) and the impulse approximation. In the diffusive regime, the rate of energy increase for binaries with semi-major axis, a, is,

$$\dot{\mathcal{E}} = \dot{C}\langle\Delta\mathcal{E}\rangle = \frac{14}{3}\sqrt{2\pi}\frac{G^2 M_{\mathrm{p}}^2 n_p a^2}{\sigma_{\mathrm{rel}}} \int \frac{\mathrm{d}b}{b^3}, \tag{2.30}$$

where the average energy change, $\langle\Delta\mathcal{E}\rangle$, is given by Eq. (2.26) and to find the encounter rate Eq. (2.29) has been integrated over V_{rel} between 0 and ∞. By integrating Eq. (2.30) over b between b_{min} and ∞, we can estimate the disruption time of a binary due to diffusive encounters with compact objects,

$$t_{\mathrm{d,diff}} \simeq \frac{|\mathcal{E}|}{\dot{\mathcal{E}}} \simeq 0.085\frac{\sigma_{\mathrm{rel}} M_{\mathrm{b}} b_{\mathrm{min}}^2}{G M_{\mathrm{p}}^2 n_p a^3}, \tag{2.31}$$

setting $b_{\rm min} \sim a$ because for impact parameters smaller than this the distant tide approximation fails,

$$t_{\rm d,diff} \simeq k_{\rm diff} \frac{\sigma_{\rm rel} M_{\rm b}}{G M_{\rm p} \rho a}, \tag{2.32}$$

where $k_{\rm diff} \equiv 0.085 (b_{\rm min}/a)^2$. Monte Carlo simulations of diffusive encounters have found that in practice, $k_{\rm diff} \approx 0.002$ [39]. For our canonical parameters, Eq. (2.32) evaluates to,

$$t_{\rm d,diff} \sim 200 \text{ Gyr } \left(\frac{k_{\rm diff}}{0.002}\right) \left(\frac{\sigma_{\rm rel}}{220 \text{km s}^{-1}}\right) \left(\frac{M_{\rm b}}{M_\odot}\right) \times \left(\frac{M_{\rm p}}{1 M_\odot}\right)^{-1} \left(\frac{\rho}{0.009 M_\odot \text{ pc}^{-3}}\right)^{-1} \left(\frac{a}{10^4 \text{ au}}\right)^{-1}. \tag{2.33}$$

This timescale is much larger than the age of the Milky Way, suggesting that, for perturber mass $M_{\rm p} \sim 1 M_\odot$, we are unlikely to find binaries that have broken only due to the diffusive effects of many encounters. It's worth noting, however, that after each encounter the binary's semi-major axis increases, reducing the diffusive disruption timescale.

In the catastrophic regime, where perturbers are massive enough to break a binary in a single encounter, the disruption time is equal to the average time between encounters,

$$t_{\rm d,cat} \simeq \frac{1}{\dot{C}} \simeq k_{\rm cat} \frac{M_{\rm b}^{1/2}}{G^{1/2} \rho a^{3/2}}, \qquad (k_{\rm cat} \approx 0.07), \tag{2.34}$$

where Eq. (2.29) has been integrated over b between 0 and b_1, the impact parameter for which $\langle \Delta \mathcal{E} \rangle = |\mathcal{E}|$. Notably, the disruption timescale in the catastrophic regime is independent of perturber mass, $M_{\rm p}$. This is because the effect of the decreased number density for more massive perturbers is cancelled out by a larger value of b_1. For our parameters,

$$t_{\rm d,cat} \sim 10 \text{ Gyr } \left(\frac{k_{\rm cat}}{0.07}\right) \left(\frac{M_{\rm b}}{M_\odot}\right)^{\frac{1}{2}} \left(\frac{\rho}{0.009 M_\odot \text{ pc}^{-3}}\right)^{-1} \left(\frac{a}{10^4 \text{au}}\right)^{-\frac{3}{2}}. \tag{2.35}$$

By equating $t_{\rm d,diff}$ and $t_{\rm d,cat}$ we can find the critical perturber mass, $M_{\rm crit}$,

which separates the two regimes,

$$M_{\rm crit} = \frac{k_{\rm diff}}{k_{\rm cat}} \left(\frac{\sigma_{\rm rel}^2 M_{\rm b} a}{G} \right)^{1/2}, \\ \sim 20 M_\odot \left(\frac{\sigma_{\rm rel}}{220 {\rm km\ s^{-1}}} \right) \left(\frac{M_{\rm b}}{M_\odot} \right)^{\frac{1}{2}} \left(\frac{a}{10^4 {\rm au}} \right)^{\frac{1}{2}}. \quad (2.36)$$

The diffusive regime applies for encounters with perturbers less massive than $M_{\rm crit}$, and the catastrophic regime applies for more massive perturbers.

From these estimates, we expect to find that for perturber masses smaller than $\sim 20 M_\odot$, binaries are very unlikely to be broken but may increase in semi-major axis over the duration of our simulations. For perturber masses larger than this, however, we expect a large number of binaries to be disrupted.

2.4 Previous work

In Sec. 2.4.1, I discuss previous work on wide binary disruption. This work was not a means to constrain compact objects but many of the methods used in these papers are relevant to our work. In Sec. 2.4.2, I provide a comprehensive review of previous papers which used wide binaries to constrain compact objects in the halo, and in Sec. 2.4.3, I outline how we intended to improve on this work going into this project.

2.4.1 Studies of wide binary disruption in the Galactic disk

These studies consider effects like the Galactic tide and encounters with giant molecular clouds that are likely negligible for our work.

Bahcall et al. [39] 1985

Bahcall et al. [39] use the existence of wide binaries in the Galactic disk to show that 'unseen disk objects' (a dark matter theory from the 1980s), which constitute half of the local mass density, must have mass less than $2 M_\odot$. They use Monte Carlo simulations of encounters between binary stars and point-like massive objects ('disk things', written as DTs) to find the half-life of a binary

as a function of its semi-major axis and the mass of the DTs.

In their simulations, they assume that binaries form with equal probability per unit logarithmic interval in semi-major axis. Binary disruption is modelled by placing individual binaries in a sea of point particles (DTs), with velocities drawn from an isotropic Maxwellian distribution. The impulse approximation is used to model encounters, and justified by the fact that a 'typical encounter' only lasts for 0.1% of the binary's orbital period.

The effects of Galactic tidal fields, other passing stars and giant molecular clouds have not been taken into account for simplicity. Bahcall et al. [39] justify the omission of these effects by stating that including them would only tighten their constraint on the mass of the unseen disk objects.

Weinberg et al. [101] 1987

Weinberg et al. [101] simulate encounters between binaries and passing stars and giant molecular clouds in the solar neighbourhood. Encounters with large impact parameters are treated statistically while encounters with small impact parameters are treated individually. Their Monte Carlo method uses the mean and variance of the energy change due to an encounter to predict the overall effect of encounters in the diffusive regime, where encounters have a small but cumulative effect.

Their simulations are used to estimate the characteristic lifetime of a binary due to diffusive encounters from passing stars and giant molecular clouds. The Galactic tide is modelled with a tidal cutoff at $a = 1\text{pc}$, binaries with semi-major axes larger than this are considered broken. They conclude that the existence of objects in the disk that can break wide binaries on a timescale similar to the age of the Galaxy is unlikely but not impossible.

Jiang and Tremaine [102] 2010

Jiang and Tremaine [102] predict effects of passing field stars on the distribution of semi-major axes of wide binaries in the Galactic disk. Rather than

using a tidal cutoff to simulate the Galactic tidal field, they use an approximation of the Galactic potential to find the centre of mass velocity of each binary system and the individual velocities of the stars due to the Galactic disk. Another feature of their simulations is the inclusion of unbound binaries.

For binaries with small semi-major axes, where the effect of the Galactic tide is small compared with the force between the two stars, the evolution is simulated with the diffusion equation. The diffusion equation [101], which requires that the energy change due to encounters is much smaller than the binding energy of the binary, provides an analytical expression for the binary energy after a given amount of time. They find that the Galactic tide causes a minimum in the semi-major axis distribution at $\sim$ 8pc rather than a cut-off, binaries that have broken can become rebound and the small relative velocities between broken binary members mean they can be mistaken for bound binaries by observations.

2.4.2 Constraints on the halo fraction of compact objects

These are the previous studies constraining the halo fraction of compact objects using wide binary disruption.

Yoo et al. [84] 2004

Yoo et al. [84] compare Monte Carlo simulations with the observed halo binary distribution using data from Chanamé and Gould [103], who constructed a catalogue of binary stars using data from the New Luyten Two Tenths catalog [104, 105] and categorised each as either a disk or halo binary.

They use the impulse approximation and ignore effects from Galactic tides and molecular clouds arguing that they can disregard these effects because they are modelling halo binaries rather than disk binaries. Ionised binaries are included but do not contribute significantly to their results and they ignore variation in the dark matter density along binary Galactic orbits.

Yoo et al. [84] conclude that MACHOs with masses $M > 43M_{\odot}$ are ex-

cluded at the 95% confidence level, and that this almost completely closes the only remaining mass window for MACHOs.

Quinn et al. [85] 2009

Quinn et al. [85] evaluate the validity of the binaries used by Yoo et al. [84], then recalculate the constraints on the MACHO mass. They confirm that three of the four widest halo binaries are genuine, by measuring the radial velocities of the binary components and checking that they are within measurements errors, and follow the method from Yoo et al. [84] leaving out the spurious binary. From their radial velocity measurements, they calculated Galactic orbits for the three confirmed binaries and found that the average dark matter density along these Galactic orbits is much less than the local dark matter density. They suggest that their constraints could be shifted upwards by a factor of 5 to take this into account. Their amendments move the upper limit on the MACHO mass from $43M_{\odot}$ to $\sim 500M_{\odot}$, but they conclude that this is too small a sample to place meaningful constraints on the MACHO mass.

Monroy-Rodríguez and Allen [86] 2014

Monroy-Rodríguez and Allen [86] use 251 candidate halo binaries from a more recent catalog [106] to determine a new upper bound for the MACHO mass. More details on this catalog are given in Sec. 4.5. They closely follow the method of Yoo et al. [84] with a few adjustments: they use a time averaged halo density found by averaging over the Galactic orbits of the binaries and the effect of the Galactic disk is estimated by calculating the fraction of time each binary spends in the disk and finding constraints from those binaries that spend the least time in the disk.

From the 25 most halo-like binaries, which spend on average 8% of their lifetimes in the disk, Monroy-Rodríguez and Allen [86] give an upper limit on the MACHO mass of $(3 - 12)M_{\odot}$. This range of masses comes from the different statistics used to calculate them. This limit almost completely rules

out MACHOs as the sole component of dark matter in the halo.

2.4.3 Improvements

Our work is primarily a discussion on the approximations made in these previous papers: which of these are accurate and which would benefit from more complex simulations. Going into this project our main concern was the initial semi-major axis distribution, the log flat distribution used in previous work is not physically motivated and could be updated to match current theories on wide binary formation mechanisms. We found that other changes, such as the inclusion of unbound and rebound binaries, also have a large impact on our final constraints. We discuss the approximations we made in Sec. 3.2.

Chapter 3

Simulations

In this chapter, after a brief overview of how our simulation works (Sec. 3.1), we will discuss what approximations we have made and how they compare to those made in previous work (Sec. 3.2), the details of our simulations (Sec. 3.3), the numerical accuracy of our simulations (Sec. 3.4), the resulting semi-major axis distributions (Sec. 3.5) and their comparison to previous results (Sec. 3.5.1).

3.1 Overview of simulation

We simulate the effect of gravitational encounters on a population of binary stars. Each binary evolves independently of the others and is defined by its semi-major axis and eccentricity. After generating the initial semi-major axis and eccentricity of a binary, we draw the number of encounters it will experience over 10Gyr from a Poisson distribution. The impact parameter and relative velocity of each encounter are calculated as described in Sec. 3.3.3 and then, after calculating the position and velocity of the two components of the binary, the encounter is implemented by applying the impulse approximation. The semi-major axis and eccentricity are recalculated and the next encounter is simulated. The time at which each encounter happens isn't necessary to calculate, except for in the case of unbound binaries which is described in detail in Sec. 3.3.4. Our simulation code can be found here.

3.2 Methods and approximations

Here we discuss the approximations made in order to simulate the evolution of binaries in a sea of perturbers. The effects considered here are the impulse approximation (Sec. 3.2.1), unbound binaries (Sec. 3.2.2), the maximum impact parameter (Sec. 3.2.3), a non-uniform dark matter density (Sec. 3.2.4), binary interactions with the Galactic disk (Sec. 3.2.5), encounters with other stars, interactions with the Galactic tide and the effect of giant molecular clouds (Sec. 3.2.6).

3.2.1 Accuracy of the impulse approximation

Previous papers have justified using the impulse approximation by stating that the duration of the encounter is much less than the period of the binary or that the relative velocity dispersion is much larger than the relative speed of the binary stars [39, 84, 101, 102].

The duration of the encounter can be approximated as,

$$t_{\rm enc} \sim \frac{2b}{\sigma_{\rm rel}}, \tag{3.1}$$

where b is the impact parameter of the encounter and $\sigma_{\rm rel}$ is the relative velocity dispersion. The period of the binary is,

$$P = 2\pi\sqrt{\frac{a^3}{GM_{\rm b}}}, \tag{3.2}$$

where a is the semi-major axis of the binary and $M_{\rm b}$ is the total mass of the binary. For the most extreme encounters, at the maximum impact parameter (see Sec. 3.2.3), the ratio of encounter duration to binary period is,

$$\frac{t_{\rm enc}}{P} \sim 0.00142 \left(\frac{\delta}{10^{-3}}\right)^{-\frac{1}{2}} \left(\frac{a}{10^4 {\rm au}}\right)^{-\frac{3}{4}} \left(\frac{\sigma_{\rm rel}}{220 {\rm km\ s^{-1}}}\right)^{-\frac{3}{2}} \left(\frac{M_{\rm b}}{M_\odot}\right)^{\frac{1}{4}} \left(\frac{M_{\rm p}}{M_\odot}\right)^{\frac{1}{2}}, \tag{3.3}$$

where δ, used to derive an expression for the maximum impact parameter, is the largest possible fractional change in semi-major axis a binary will experience due to an encounter at the maximum impact parameter. In practice,

$\delta = 10^{-3}$ is small enough to capture the full effects of wide binary evolution and we use this value in our simulations, see Sec. 3.2.3 for more details. Since $\frac{t_{\rm enc}}{P}$ is very small, the stars move a negligible amount during the encounters and the impulse approximation is likely to be valid.

In order to confirm that the impulse approximation gives sufficiently accurate results, we compared the semi-major axis after an encounter calculated using Eqs. (2.20) and (2.21) with the final semi-major axis calculated from a three body integration code. Our three body integration code uses a fourth order Hermite integrator and dynamic time steps as described by Dehnen and Read [107]. The dynamic time steps used are given by the Aarseth criterion [107, Eq. (25)], the time step for the ith body is,

$$\Delta t_i = \left(\eta \frac{|\mathbf{a}_i||\ddot{\mathbf{a}}_i| + |\dot{\mathbf{a}}_i|^2}{|\dot{\mathbf{a}}_i||\dddot{\mathbf{a}}_i| + |\ddot{\mathbf{a}}_i|^2} \right)^{1/2}, \tag{3.4}$$

where $\eta = 0.02$, $\mathbf{a}_i$ is the acceleration of body i and dots denote differentiation with respect to time. We take the minimum value of this time step for the three objects as the time step for the system.

The simulation starts when the ratio of the force between the PBH and its nearest star and the force between the two stars is 10^{-6}, it finishes when the force ratio returns to 10^{-6}. If the PBH is never close enough to the binary for the ratio of forces to be 10^{-6} or larger, then the encounter is considered to be negligible and the semi-major axis and eccentricity are unchanged.

The impact parameter chosen here is the minimum likely impact parameter, $b_{\rm min}$, which is derived by requiring that only one encounter per binary is expected with an impact parameter equal to or less than the minimum impact parameter over the lifetime of the Galaxy. This gives the expression,

$$\begin{aligned} b_{\rm min} &= \sqrt{\frac{M_{\rm p}}{\pi \rho \sigma_{\rm rel} T}}, \\ &= 800{\rm au} \left(\frac{M_{\rm p}}{M_\odot} \right)^{\frac{1}{2}} \left(\frac{\rho}{0.009 M_\odot {\rm pc}^{-3}} \right)^{-\frac{1}{2}} \left(\frac{\sigma_{\rm rel}}{220{\rm km\ s}^{-1}} \right)^{-\frac{1}{2}} \left(\frac{T}{10{\rm Gyr}} \right)^{-\frac{1}{2}}. \end{aligned} \tag{3.5}$$

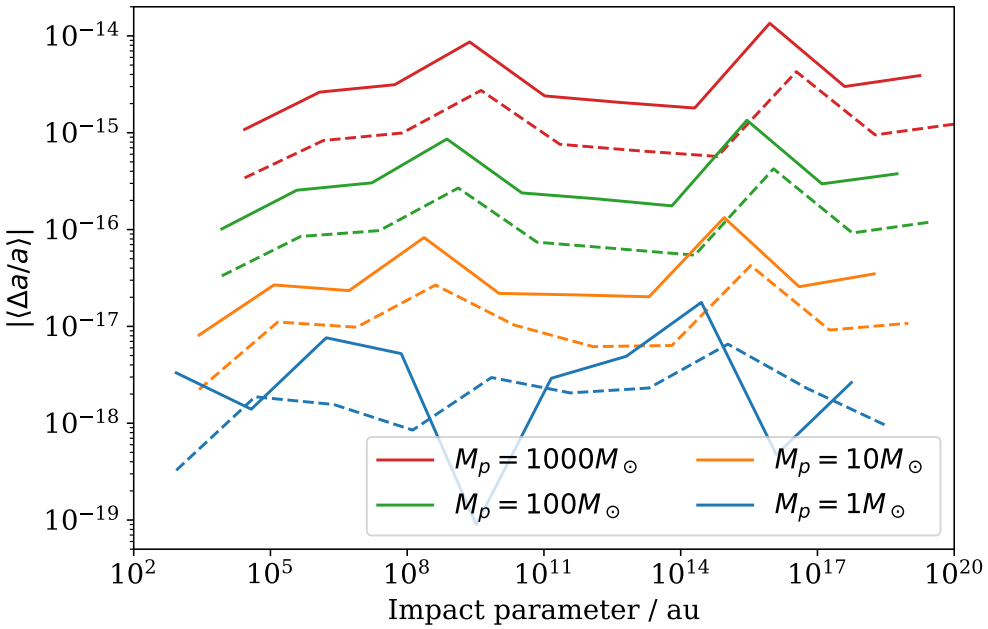

Figure 3.1: The absolute average (of 100 encounters) fractional error in the final semi-major axis a, after an encounter, calculated using the impulse approximation. It's evaluated here at 10 impact parameters logarithmically spaced between the minimum likely and maximum impact parameter (see text) for different perturber masses M_p. The solid lines are simulations with initial semi-major axis $a = 10^4$au and the dashed lines are simulations with initial semi-major axis $a = 10^5$au.

where ρ is the mass density of compact objects and T is the total simulation time.

The resulting average fractional error in the final semi-major axis is shown in Fig. 3.1. For typical parameters, the change in semi-major axis calculated using the impulse approximation is correct to 14 significant figures showing that it is valid in this parameter space.

3.2.2 Unbound binaries

Once a binary becomes unbound there are two ways in which it could affect our results:

1. An unbound binary might 'look' like a bound binary in observational data since the two stars might still be near each other and have similar peculiar velocities. In this case it might be necessary to keep the unbound binaries as part of our final distribution of binary semi-major axes.

2. An unbound binary could become rebound again after subsequent encounters with perturbers.

Two previous relevant works that have discussed unbound binaries are Yoo et al. [84] and Jiang and Tremaine [102]. Yoo et al. [84] provide an analytical argument for why omission of unbound binaries will not significantly affect their results and a prescription for including unbound binaries in their simulations which they use to show that unbound binaries have a negligible contribution. Their analytical argument shows that two previously bound stars moving away from each other will be disrupted by the Galactic tide in less that 0.13Gyr after becoming unbound, this would mean that only binaries disrupted in the last $\sim$1% of the age of the Galaxy could be confused with bound systems. To include unbound binaries in their simulations they assume that the two stars in an unbound binary drift away from each other in a random direction with a constant relative velocity given by their escape velocity. The stars then continue to experience perturbations until the end of the simulation time. Yoo et al. [84] find that unbound binaries have no significant effect on their final distribution of binary separations.

Between encounters with a perturber, Jiang and Tremaine [102] evolve their binary stars by integrating their orbits in the Galactic potential and the binary's potential. Their approach is valid for unbound as well as bound binaries and they keep unbound binaries in the simulations. They find that the components of unbound binaries have small relative velocities allowing them to be detected as binaries by large astrometric surveys. The difference in conclusion between these two papers could be because Jiang and Tremaine [102] studied the disruption of disk binaries in the solar neighbourhood while Yoo et al. [84] studied halo binaries. Our method for simulating binaries, including the differences for simulating unbound binaries is described in Sec. 3.3.

Simulation results from unbound binaries

Figure 3.2 shows the distribution of unbound binary separations after 10Gyr of evolution in a sea of perturbers with mass $M_{\rm p}$, where the separation is the physical distance between the two stars in the binary. This simulation used a log flat distribution for the initial semi-major axes of the 10^6 binary star systems.

Allen and Monroy-Rodríguez [106] provide a catalog of halo wide binary candidates. The largest semi-major axis of any of their candidate binaries is $\sim$ 1.7pc. Figure 3.2 shows that $\lesssim$ 100 binaries (out of 10^6 binaries in the simulation) are unbound with separations $\sim$ 1.7pc at the end of the simulation. This is small compared to the total number of binaries, however, in order to check that the number of unbound binaries at this separation is negligible it's necessary to compare with the number of bound binaries at this separation.

Figure 3.3 is as in Fig. 3.2 with binaries that were bound throughout the simulation (solid lines), are unbound at the end of the simulation (dotted lines) and have been unbound at some point during the simulation but are bound at the end (dashed lines) plotted separately. Below a separation of $\sim$ 1.7pc the number of unbound binaries is much less than the number of bound binaries, indicating that unbound binaries can be left out of the final separation distribution for comparisons with observational data. However, as shown by the dashed lines in Fig. 3.3, at a separation of 0.1pc the number of rebound binaries is only 10 times less than the number of always bound binaries, this is possibly large enough to have an effect on results.

While the number of unbound binaries in the range of separations we're interested in (below $\sim$ 1.7pc) is relatively low, the number of rebound binaries is large enough to affect the distribution of binary separations. Figure 3.4 shows the difference in final semi-major axis distribution after 10Gyr of evolution. Since there is a large difference between the 'always bound' (solid lines) distribution and the distribution for the whole population (dot-dashed lines),

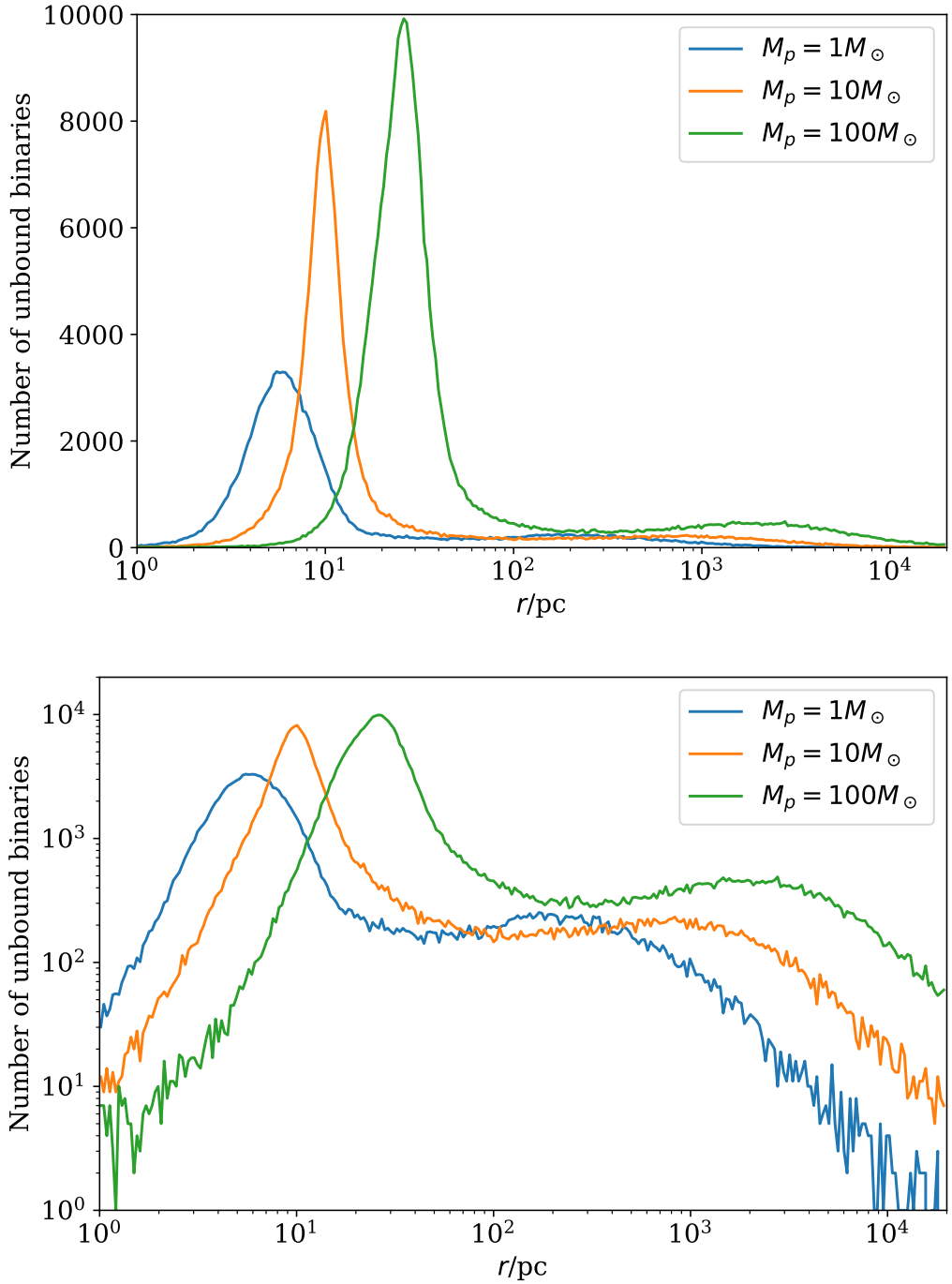

Figure 3.2: The number of unbound binaries with separation r after 10Gyr of evolution in a sea of perturbers with mass M_p, dark matter density $\rho = 0.009 M_\odot \mathrm{pc}^{-3}$ and relative velocity dispersion $\sigma_\mathrm{rel} = 220\mathrm{km\ s}^{-1}$. The 10^6 binaries in the simulation had initial semi-major axes drawn from a log flat distribution. Binaries with a separation larger than 10^4pc, which is large enough to assume that the binary is realistically broken, are removed from the simulation to keep computation time low. The two plots are identical other than the y-axis which is linear in the top panel and logarithmic in the bottom panel.

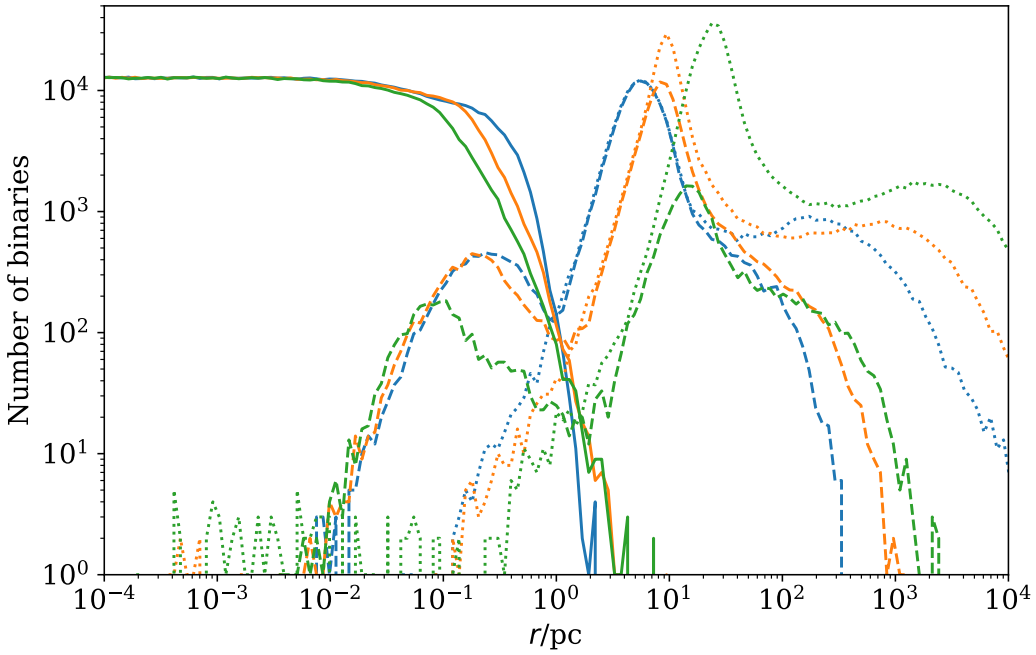

Figure 3.3: The number of unbound binaries with separation r after 10Gyr of evolution in a sea of perturbers with mass $1M_\odot$ (blue lines), $10M_\odot$ (orange lines) or $100M_\odot$ (green lines); dark matter density $\rho = 0.009M_\odot\text{pc}^{-3}$ and relative velocity dispersion $\sigma_{\text{rel}} = 220\text{km s}^{-1}$. The 10^6 binaries in the simulation had initial semi-major axes drawn from a log flat distribution. Binaries with a separation larger than 10^4pc, which is large enough to assume that the binary is realistically broken, are removed from the simulation to keep computation time low. Binaries that were bound for the duration of the simulation (solid lines), binaries that are unbound at the end of the simulation (dotted lines) and binaries that were broken at least once during the simulation but are bound at the end (dashed lines) are plotted separately.

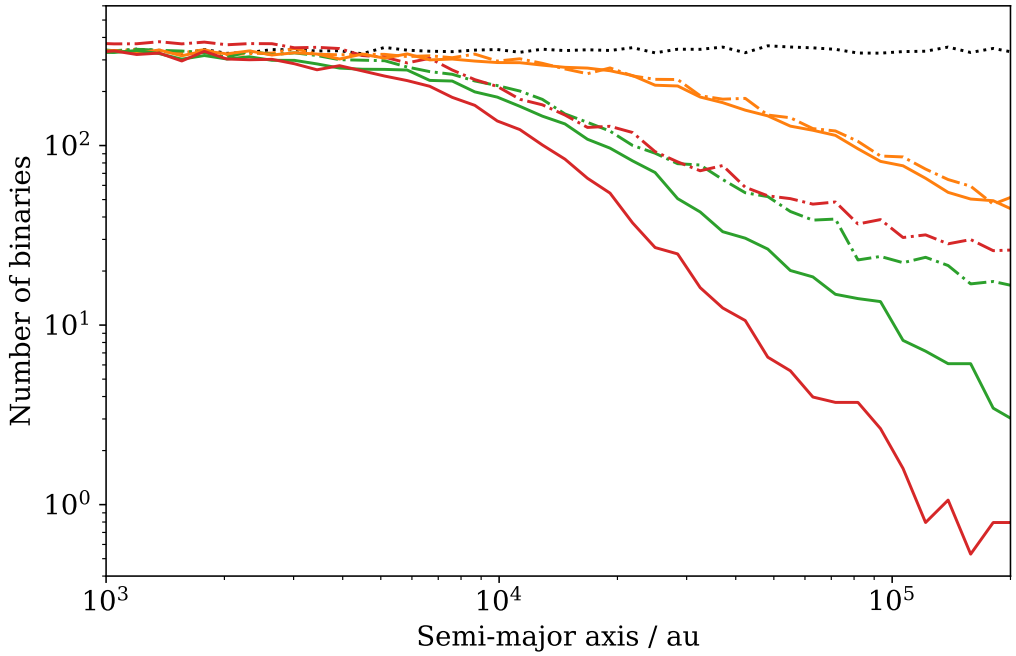

Figure 3.4: The semi-major axis distribution of 10^5 binaries with total binary mass $M_{\rm b} = 1M_{\odot}$ after 10Gyr of evolution in a sea of perturbers with masses $10M_{\odot}$ (orange lines), $100M_{\odot}$ (green lines) and $1000M_{\odot}$ (red lines); perturber density $0.009M_{\odot}{\rm pc}^{-3}$ and relative velocity dispersion $\sigma_{\rm rel} = 220{\rm kms}^{-1}$. The distribution of the binary semi-major axes before the 10Gyr of evolution is given by the black dotted line. The solid lines correspond to binaries that were bound for the entirety of the simulation, the dot-dashed lines correspond to the entire population of binaries.

it is necessary to include unbound binaries in our simulations.

3.2.3 Maximum impact parameter

The maximum impact parameter should be large enough that all encounters which have a notable effect on the binary system are simulated, but small enough such that no computing time is wasted since the number of encounters that a binary system experiences is proportional to $b_{\rm max}^2$.

The expression for $b_{\rm max}$ used in these simulations requires that the fractional change in semi-major axis due to an encounter at $b_{\rm max}$ is less than a small

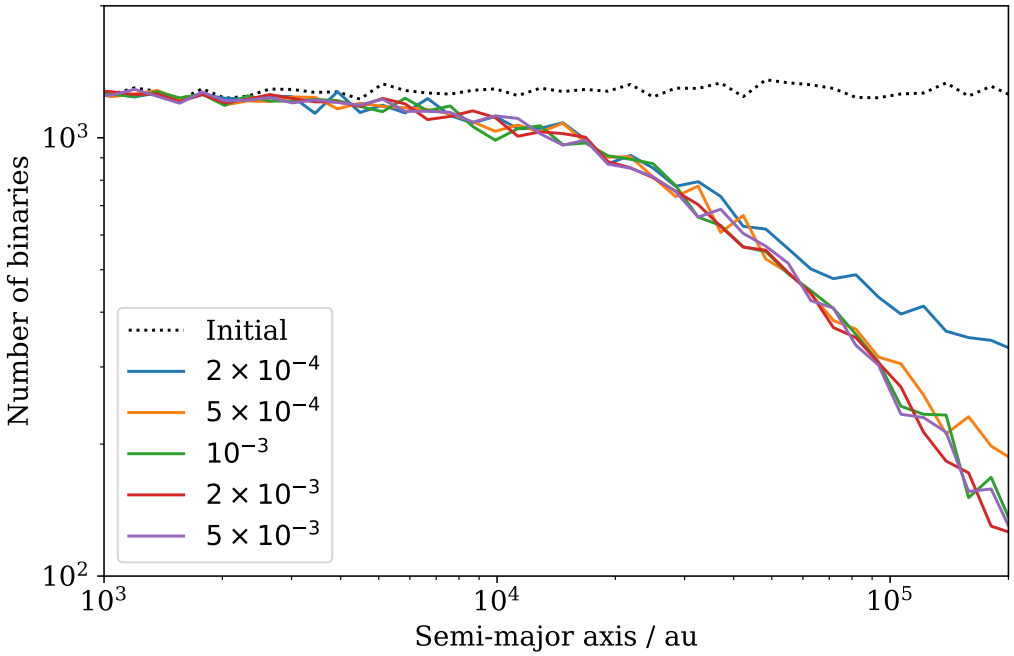

Figure 3.5: The distribution of semi-major axes of 10^5 binaries with mass $1M_\odot$ after 10Gyr of evolution in a sea of PBHs with mass $10M_\odot$, mass density $0.009M_\odot \mathrm{pc}^{-3}$, and relative velocity dispersion $200\mathrm{kms}^{-1}$. The dotted line is the initial distribution of semi-major axes. The solid lines are distributions for different values of δ. The blue, orange, green, red and purple lines are simulations with δ equal to 0.2, 0.5, 1.0, 2.0 and 5.0 times 10^{-3} respectively.

number δ (see Appendix A for derivation):

$$\begin{aligned} b_{\max} &= \left(\frac{64GM_\mathrm{p}^2a^3}{M_\mathrm{b}\sigma_\mathrm{rel}^2\delta^2}\right)^{\frac{1}{4}}, \\ &= 0.1\mathrm{pc}\left(\frac{\delta}{10^{-3}}\right)^{-\frac{1}{2}}\left(\frac{M_\mathrm{p}}{M_\odot}\right)^{\frac{1}{2}}\left(\frac{M_\mathrm{b}}{M_\odot}\right)^{-\frac{1}{4}}\left(\frac{a}{10^4\mathrm{au}}\right)^{\frac{3}{4}}\left(\frac{\sigma_\mathrm{rel}}{220\mathrm{kms}^{-1}}\right)^{-\frac{1}{2}}, \end{aligned} \tag{3.6}$$

where M_p is the mass of the PBHs, M_b is the total mass of the binary system, a is the semi-major axis of the binary system and σ_rel is the relative velocity dispersion between the binary stars and PBHs. We tested the effects of changing δ on the final binary semi-major axis distribution in order to find the best value by increasing δ until the distribution stopped changing, our results are plotted in Fig. 3.5. The plot shows that $\delta = 2 \times 10^{-4}$ is much too small, but $\delta = 10^{-3}$ gives a large enough maximum impact parameter to include all encounters that have a non-negligible effect.

3.2.4 Non-uniform dark matter density

The Galactic orbits of the halo binaries we studied [106] have pericentres as small as 0.1kpc and apocentres as large as 100kpc. It's not obvious that the time-averaged dark matter densities along the binary Galactic orbits will be similar enough to the local density for the effect of variable density to be ignored. Yoo et al. [84] find that the time-averaged dark matter density along their Galactic orbits is higher than the value at the solar radius. Since including the non-uniform dark matter density in this case would lead to more disruption and therefore stronger constraints, Yoo et al. [84] ignore this effect and approximate the density to be constant and equal to the density at the solar radius.

These Galactic orbits were then recalculated by Quinn et al. [85] using model I from Dehnen and Binney [108]. The mean time-averaged dark matter density is found to be between 10% and 45% of the density at the solar radius. They suggest re-scaling their final constraints to take this difference into account.

Monroy-Rodríguez and Allen [86] calculate the Galactic orbits for their binary catalog [106] using the Galactic halo mass distribution from Allen and Santillan [109]. They find that the mean time-averaged dark matter density along their orbits is not very different from the density at the solar radius and only has a small effect on their final constraints.

It's appropriate to use the time-averaged density here because the only place in the simulations where the dark matter density appears is the calculation of the encounter rate. Using the time-averaged density along the orbit as the density for a particular binary would therefore provide exact results.

We calculated the binary Galactic orbits again for the Allen and Monroy-Rodríguez [106] catalog using the `galpy` python package [110]. We used the MWPotential2014 model from the package. This model is provided by the `galpy` package for convenience and not intended to be used as the current

best Galactic potential so we will justify our use of it here. Any uncertainty in the parameters used to fit the model will be subdominant to other sources of uncertainty in our study and is beyond the scope of this paper. Also, the model is not out of date since the best fit parameters for the Galactic model haven't changed significantly since 2014 [see e.g. Ref. 111].

From our binary Galactic orbits we find that the mean time-averaged dark matter density is $0.0106 M_{\odot}\mathrm{pc}^{-3}$, a little larger than the density at the solar radius ($0.00754 M_{\odot}\mathrm{pc}^{-3}$). The differences found between our average density and those found by previous authors may be accounted for by the fact that we find very different Galactic orbits for two of the binaries in the sample: NLTT 10536 and NLTT 16394. Orbits for four of our binaries are plotted in Fig. 3.6, these orbits can be compared with the orbits from [85] Fig. 4. Our orbit for NLTT 10536 agrees with the orbit calculated by Monroy-Rodríguez and Allen [86] but disagrees with Quinn et al. [85]'s calculation, this is likely explained by the large difference between their distance and line of sight data when compared with data from SIMBAD for this binary. We found that the orbit for NLTT 10536 has a maximum z coordinate of around 5kpc, whereas Quinn et al. [85] find it to be around 40kpc. This might explain the different mean time-averaged dark matter density calculated by Quinn et al. [85]. We also believe that Monroy-Rodríguez and Allen [86] and Quinn et al. [85] used an incorrect value for the starting distance from the Sun for NLTT 16394, as a result we were unable to reproduce this orbit.

The probability density of the time-averaged dark matter densities for the 160 binaries we can calculate Galactic orbits for is shown in Fig. 3.7. The orange line indicates the dark matter density at the solar radius for our Galactic model and parameters, $0.00754 M_{\odot}\mathrm{pc}^{-3}$, which is slightly smaller than the mode of the time-averaged dark matter density distribution (blue line). Since the peak of the dark matter density distribution is narrow, with a full-width-half-maximum of 0.00693, re-scaling our constraints should give a good estimate of the effect of a variable dark matter density, this process is described

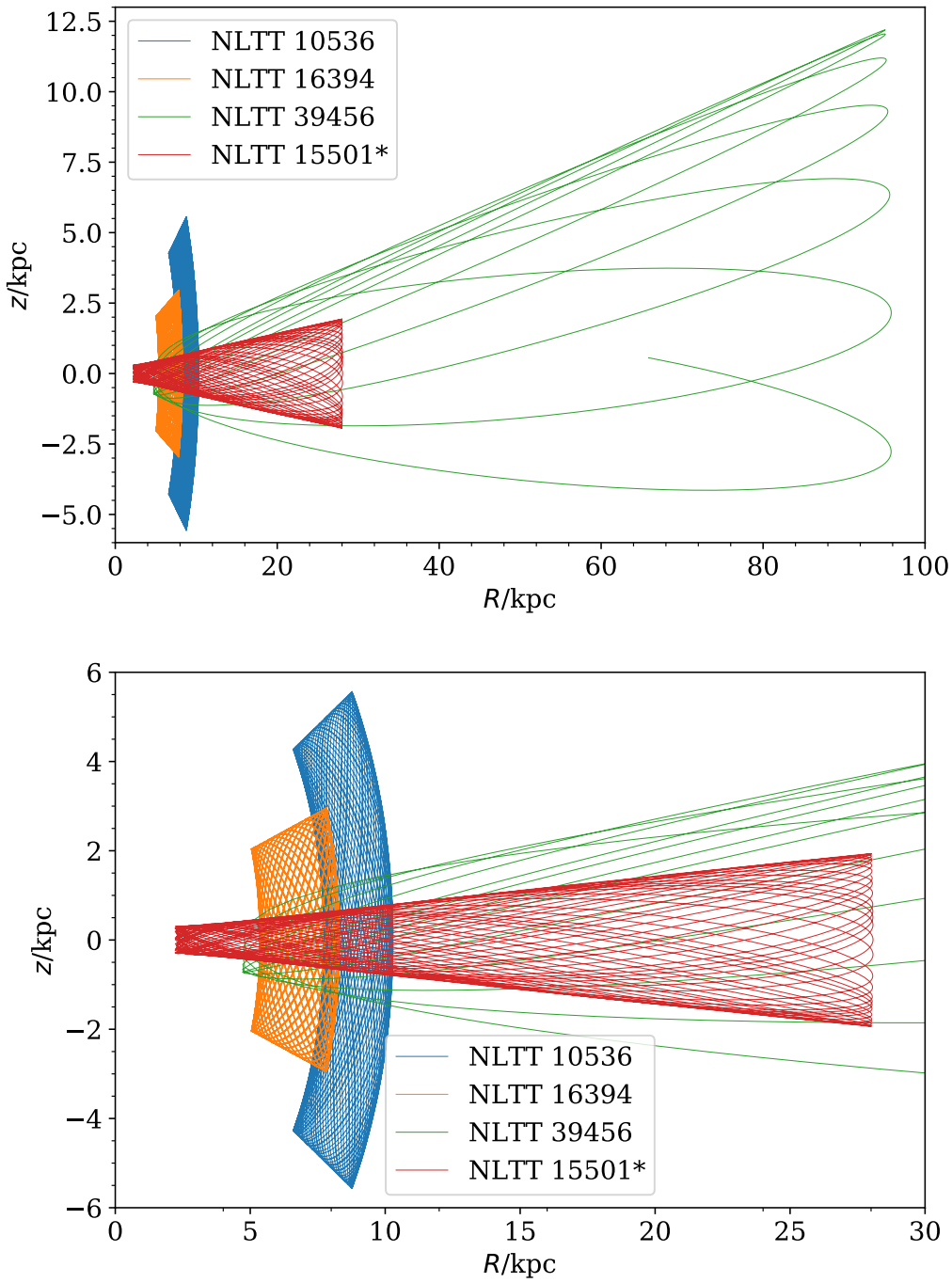

Figure 3.6: Galactic orbits for four of the wide binaries in our catalog for a duration of -10Gyr. Calculated and plotted using the `galpy` python package [110] with the MWPotential2014 Galactic potential. The initial conditions are from the SIMBAD database for NLTT 10536, 16394 and 39456. *The initial conditions for NLTT 15501 are from Quinn et al. [85] Table 1. The bottom plot is the same as the top plot but zoomed in on the smaller orbits.

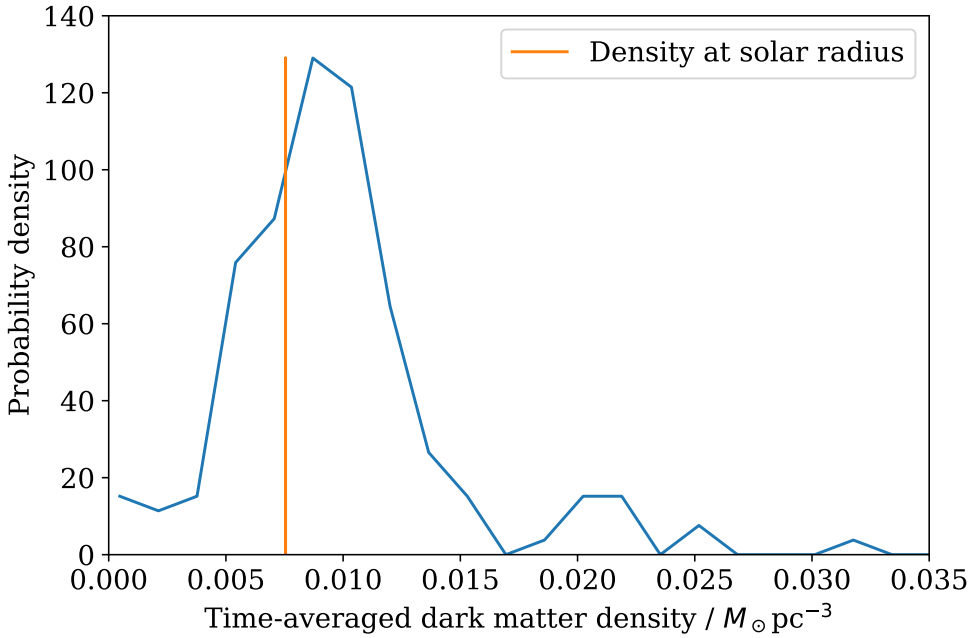

Figure 3.7: Probability density of the time-averaged dark matter density calculated along the Galactic orbits of 160 binaries from Allen and Monroy-Rodríguez [106] over 10Gyr. The orange vertical line shows the dark matter density at the solar radius, $0.00754 M_\odot \mathrm{pc}^{-3}$. The orbits and densities were calculated using the `galpy` python package and the MWPotential2014 Galactic potential [110].

in more detail in Sec. 4.6. For more information on the wide binary catalog we used see Sec. 4.5.

3.2.5 Interaction with the Galactic disk

Yoo et al. [84] estimate the effect of a binary passing through the Galactic disk by equating the change in the z-velocity of a binary passing through the disk with its internal velocity. The critical semi-major axis found this way, above which the binary is susceptible to breaking when passing through the disk, is,

$$a_{\mathrm{crit}} = \left(\frac{M_{\mathrm{b}} v_z^2}{16\pi^2 G \Sigma^2} \right)^{1/3}, \tag{3.7}$$

where M_{b} is the total mass of the binary, v_z is the velocity with which binaries cross the disk and Σ is the surface density of the disk. They find that in the solar neighbourhood this semi-major axis limit is ≈ 2pc. This is only a little larger than their largest projected separation so they conclude that the effect of the Galactic disk is non-negligible. However, since the effect of including

the Galactic disk is to make their constraints more conservative, they ignore the effects of the disk in their simulations.

Monroy-Rodríguez and Allen [86] calculate the amount of time that 150 of their 251 binaries spend in the disk and evaluate different upper limits for the PBH mass depending on which binaries are used to calculate the constraint. They find that for the 25 most halo-like binaries, i.e. the 25 binaries that spend the least amount of their time in the disk, their constraints are much stronger than for the 100 most halo-like binaries. This trend is consistent for the intervening numbers and supports the assumption that ignoring the effects of the Galactic disk is a conservative approximation. We perform a similar analysis of the effects of the Galactic disk to Monroy-Rodríguez and Allen [86], the method and results of this analysis are given in Sec. 4.7.

We find that our constraints for the 25 most halo-like binaries are tighter than those for the larger population of binaries, however, these constraints are weaker than those calculated by Monroy-Rodríguez and Allen [86] and we are unsure of the validity of calculating constraints from a sample of 25 binaries. We conclude that simulations of the Galactic potential [e.g. Ref. 102] would be preferable in order to calculate less conservative constraints.

3.2.6 Other approximations

We will be assuming that encounters with passing stars, the Galactic tide and molecular clouds are negligible. In this section I will briefly discuss how this has been justified in previous work and why ignoring these effects is a conservative approximation.

Encounters with stars

In Sec. 2.4.1, we described three papers that studied the disruption of wide binaries in the solar neighbourhood. Bahcall et al. [39] studied the disruption of wide binaries by compact objects while Weinberg et al. [101] and Jiang and Tremaine [102] studied disruption by passing stars. Given that passing stars

have such a large effect on disk binaries we will justify leaving them out of our simulations. Bahcall et al. [39] ignore this effect for simplicity and state that including the effect of passing stars would cause their binaries to break faster, which means that without this effect their constraint on the mass of compact objects in the disk is conservative. Our justification is the same, with the addition that since we are looking at the disruption of halo binaries rather than disk binaries, and the stellar density in the halo is much lower than that in the disk, the effect of stellar encounters is much smaller and in our case the approximation is more accurate.

Galactic tide

Wide binaries in the Galactic halo could be affected by tidal forces as they orbit the Galaxy. The tidal force arises when the gravitational force between the binary and Galactic centre becomes larger than the force between the two binary stars. The binary separation above which the binary is susceptible to tidal forces is called the Jacobi radius. Jiang and Tremaine [102, Eq. (43)] give an expression for the Jacobi radius of a binary orbiting the Galaxy at the solar Galactic radius,

$$r_J = 1.70\text{pc}\left(\frac{M_\text{b}}{2M_\odot}\right)^{1/3} = 1.35\text{pc}\left(\frac{M_\text{b}}{M_\odot}\right)^{1/3}, \tag{3.8}$$

where M_b is the total mass of the binary star. If a binary has separation larger than r_J it is susceptible to disruption by tidal forces. This equation only applies at the solar radius but it should still be appropriate because our most closely orbiting binaries have pericentres at approximately this distance. Yoo et al. [84] estimate this critical radius to be around 2pc, this is larger than most of the binaries in their catalog but not by much. They acknowledge that these effects are likely to be non-negligible and leave them out for simplicity, stating that this approximation only makes their constraints more conservative.

Bahcall et al. [39] ignore the effect of Galactic tides for simplicity, but Weinberg et al. [101] take Galactic tides into account with a tidal cut-off at

1pc. If a binary star has a semi-major axis of 1pc or larger at any point during their simulations it is discarded and considered to be broken. Weinberg et al. [101] found that their binaries had shorter characteristic lifetimes than those simulated by Bahcall et al. [39].

Jiang and Tremaine [102] fully simulate the binary stars in the Galactic potential, taking into account Galactic tides. While our Jacobi radius of 1.35pc is small enough that Galactic tides are likely to have some effect on our binaries, we have left out the effect of Galactic tides for simplicity. Jiang and Tremaine [102] are studying binaries that spend all of their time close to the solar radius, whereas our binaries spend the majority of their time much further away from the Galactic centre. This is an important difference since the effect of the Galactic tide is greatly reduced further from the centre of the Galaxy. We are also not using a tidal cut-off for the same reason that we are keeping unbound binaries in our simulations: it is possible and not unlikely that further interactions with perturbers will rebind the binary or decrease it's separation to below the Jacobi radius. Since the effect of the Galactic tide is to disrupt orbiting binaries, ignoring this effect is a conservative approximation.

Giant Molecular clouds

Only one of the six papers described in Sec. 2.4 takes into account perturbations from Giant Molecular Clouds (GMCs). Weinberg et al. [101] calculate the effect of GMCs using the same equations used to calculate the effect of passing stars. They predict that only encounters where the binary passes through the GMC are likely to have any effect since the GMCs have radius similar to the largest impact parameter used in the simulations. While encounters with stars have a mostly diffusive effect, they find that the main effect of GMCs is to break binaries that pass through the GMC and approach one of the GMC subclumps, especially when the binary has had its binding energy decreased through diffusive encounters. Weinberg et al. [101] find that encounters with GMCs are important for most wide binaries.

Yoo et al. [84] justify leaving GMCs out of their simulations in two ways, firstly, the low density of GMCs ($\sim 0.07\rho_{\rm DM}$) means they will have a fairly low impact on halo wide binaries and secondly, the minimum likely impact parameter (Eq. (3.5)) is considerably smaller than the size of a typical GMC. Like Yoo et al. [84], we will be ignoring encounters with GMCs for simplicity. Once again, since they may be a disruptive force for wide binaries, leaving out GMCs will make our constraints more conservative.

3.3 Simulation details

In this section we describe our method for simulating the evolution of binary stars in a sea of massive perturbers. For equations on orbital mechanics see Sec. 2.1.

3.3.1 Parameters

The following parameters remain constant throughout this paper: the total mass of the binary stars $M_{\rm b} = 1M_\odot$ (each star has mass $0.5M_\odot$); the relative velocity dispersion of the Galactic halo $\sigma_{\rm rel} = 220{\rm kms}^{-1}$ [12]; and the duration of the simulation $T = 10{\rm Gyr}$, which is the approximate age of the Galaxy [12]. These parameters are consistent with previous work [e.g. Ref. 84].

The initial binary semi-major axes are drawn from a log flat distribution between 10au and $10^{5.5}$au. This distribution was chosen to allow direct comparison with the results from Yoo et al. [84]. The choice of initial distribution here is somewhat unimportant because, like Yoo et al. [84], we use a scattering matrix to analyse the final distributions and compare them to the observed binary distribution. The scattering matrix allows us convert any initial binary semi-major axis distribution into a vector which gives the expected number of binaries in each final separation bin, this means we can test different initial distributions without having to re-run the simulations. This is possible because each binary evolves independently of all other binaries in the simulation, see Sec. 4.1 for more details. Following Yoo et al. [84] and Jiang and Tremaine

[102], the initial eccentricity squared e^2 is distributed uniformly between 0 and 1.

3.3.2 Encounter rate

Once the initial binary population has been generated, we draw the number of encounters each binary will experience from a Poisson distribution. To find the encounter rate we integrate Eq. (2.29) over $V_{\rm rel}$ between 0 and $100\sigma_{\rm rel}$ and over b between 0 and $b_{\rm max}$ (see Sec. 3.2.3). For each binary we draw the number of encounters it will experience from a Poisson distribution with mean equal to the encounter rate multiplied by the total simulation time, $T = 10$Gyr.

3.3.3 Impact parameter and relative velocity vectors

For each encounter between a binary and PBH we need to find the relative velocity and impact parameter vectors. The magnitudes of the relative velocity and impact parameter are given by the distributions in Eq. (2.29), the relative velocity $V_{\rm rel}$ has probability density,

$$P(V_{\rm rel}) = \frac{V_{\rm rel}^3}{2\sigma_{\rm rel}^4} \exp\left(-\frac{V_{\rm rel}^2}{2\sigma_{\rm rel}^2}\right). \tag{3.9}$$

We draw $V_{\rm rel}$ from this distribution using a Monte Carlo Rejection method [112]. Note the extra factor of $V_{\rm rel}$ between Eq. (2.28) and Eq. (3.9). This extra factor of $V_{\rm rel}$, which is visible in Eq. (2.29), is necessary because geometrically it is more likely for binaries to encounter faster moving PBHs.

The impact parameter probability density is given by,

$$f(b) = \frac{2b}{b_{\rm max}^2}. \tag{3.10}$$

As with the distribution of $V_{\rm rel}$ we found the b distribution by using the dependency on b from Eq. (2.29) and then the prefactor is found by normalisation. The impact parameter for each encounter is then found by,

$$b = b_{\rm max}\sqrt{x}, \tag{3.11}$$

where x is a random number between 0 and 1.

Since the PBH velocity distribution is isotropic, the velocity and impact parameter vectors should be in a random, unweighted direction. By definition of the impact parameter, the two vectors should also be perpendicular. We find two random vectors, the first vector is the velocity vector and the second vector is crossed with the first to find the direction of the impact parameter vector, random and perpendicular to the velocity.

3.3.4 Evolving the binary forward in time

Before each encounter, the binary needs to be evolved in time. For bound binaries we do this by randomising the mean anomaly since the time between encounters is much longer than the period of the binary. The mean anomaly is drawn from a uniform distribution between 0 and 2π.

For unbound binaries, since hyperbolic orbits are not periodic it wouldn't be appropriate to randomise their position in their orbit so instead we evolve the binaries in time exactly. The variable that we evolve is the eccentric anomaly which is easily moved forward in time through association with the mean anomaly and easily calculated after an encounter from the binary stars' positions and velocities.

Before each encounter we check if the binary is unbound, if it is, the eccentric anomaly is evolved forwards in time with the following method,

1. The mean motion is calculated:

$$n = \sqrt{\frac{GM_{\rm b}}{a^3}}, \tag{3.12}$$

   where G is the Gravitational constant, $M_{\rm b}$ is the total mass of the binary star and a is the semi-major axis of the binary star.

2. The mean anomaly is calculated:

$$M = e\sinh(E) - E, \tag{3.13}$$

where E is the eccentric anomaly and e is the eccentricity (see Eq. (2.12) for comparison).

3. The mean anomaly is evolved forward in time:

$$M = M + nt, \tag{3.14}$$

where t, the amount of time that has passed since the last encounter, is drawn from an exponential distribution with mean equal to the mean time between encounters (1 / rate).

4. The new eccentric anomaly is calculated numerically from Eq. (3.13) using the Newton-Raphson method.

Occasionally the numerical solution to Eq. (3.13) fails to converge due to a bad initial guess. In these cases the binary is evolved forward in time using 2 body integration code.

3.3.5 Opening the binary

In order to implement an encounter the binary needs to be 'opened', this means finding position and velocity vectors for the two binary stars from their semi-major axes, eccentricities and phases. For bound binaries we calculate the eccentric anomaly E from the mean anomaly M using Eq. (3.13) by applying the Newton-Raphson method [e.g. Ref. 112].

We then find the true anomaly f from Eq. (2.13) and the physical separation of the binary stars r is (see Eq. (2.6)),

$$r = \frac{a(1-e^2)}{1+e\cos f}. \tag{3.15}$$

The relative positions and velocities of the binary stars are,

$$\mathbf{x_1} - \mathbf{x_2} = (r\cos f, \qquad r\sin f, \qquad 0)\,, \tag{3.16}$$

$$\mathbf{v_1} - \mathbf{v_2} = \left(-\frac{na}{\sqrt{1-e^2}} \sin f, \qquad \frac{na}{\sqrt{1-e^2}}(e + \cos f), \qquad 0 \right), \tag{3.17}$$

where n is the mean motion calculated from Eq. (3.12).

For unbound binaries we calculate the positions and velocities directly from the eccentric anomaly. The relative position and velocities of the binary stars are,

$$\mathbf{x_1} - \mathbf{x_2} = \Big(a(\cosh(E) - e), \qquad a\sqrt{e^2-1}\sinh(E), \qquad 0 \Big), \tag{3.18}$$

$$\mathbf{v_1} - \mathbf{v_2} = \left(\frac{na\sinh(E)}{e\cosh(E) - 1}, \qquad \frac{na\sqrt{e^2-1}\cosh(E)}{e\cosh(E) - 1}, \qquad 0 \right). \tag{3.19}$$

These equations can be derived from Eq. (2.6) by substituting in the hyperbolic functions ($x = a(e - \cosh E)$, $y = b\sinh E$) rather than the elliptical functions ($x = a\cos E$, $y = b\sin E$), where b here is the semi-minor axis.

In both cases, the first star is stationary and at the origin, the second star is given the position and velocity from the vectors above, then the vectors are moved into the centre of mass rest frame. We don't randomise the orientation of the binaries here; random orientations would have no effect since the velocity vector of the PBH is randomised and isotropic. At the end of the simulations the binary orientations are randomised in order to calculate the projected separation of the binaries from their physical separation.

3.3.6 Application of the impulse approximation

We implement the encounter by adding Eqs. (2.20) and (2.21) to the binary star velocities. The positions of the binaries are unaffected by an encounter in the impulse approximation.

3.3.7 Closing the binary

After the encounter the binary is 'closed' again. We calculate the binary's new eccentricity and semi-major axis from Eqs. (2.17) and (2.18) respectively, and in the case of unbound binaries, the new eccentric anomaly is found by,

$$E = \operatorname{arcosh}\left(\frac{r/a + 1}{e} \right), \tag{3.20}$$

where the binary separation $r = |\mathbf{x_1} - \mathbf{x_2}|$. The derivation of Eq. (3.20) from Eq. (3.18) is straightforward. If at this point the binary has a separation r larger than 10^4pc, an unrealistically large separation, the binary is removed from the simulation and considered to have become permanently unbound.

3.4 Numerical accuracy

The energy change of a binary due to an encounter is given by Eq. (2.25). Over many encounters the first term in this equation should average to zero while the smaller second term should contribute a cumulative positive change to the binary's energy. The second term is much smaller than the first term which is usually smaller than the binary energy, so it is important that the simulations are accurate enough to capture a few significant figures of the second term.

We tested our code to find the number of significant figures of the second term that are accurate in practice. Our original code in python kept zero significant figures of the second term in the most extreme case while our new code written in C++ and using long doubles (x86 extended precision format) keeps 4 significant figures in the most extreme case and many more than 4 in most cases.

3.5 Simulation results

Figure 3.8 shows the resulting distribution from our simulations, excluding unbound binaries (solid lines), along with the final distributions from Yoo et al. [84] (dashed lines) and Monroy-Rodríguez and Allen [86] (dot-dashed). Here, 10^5 binaries were evolved for 10Gyr in a sea of PBHs with masses $10M_\odot$ (orange lines), $100M_\odot$ (green lines) and $1000M_\odot$ (red lines). When we only keep binaries that are bound for the duration of the simulation, our results are in good agreement with those from previous work. The initial distribution used here is a log flat distribution shown by the black dotted line. Binaries with larger semi-major axes are broken faster, and larger mass perturbers have

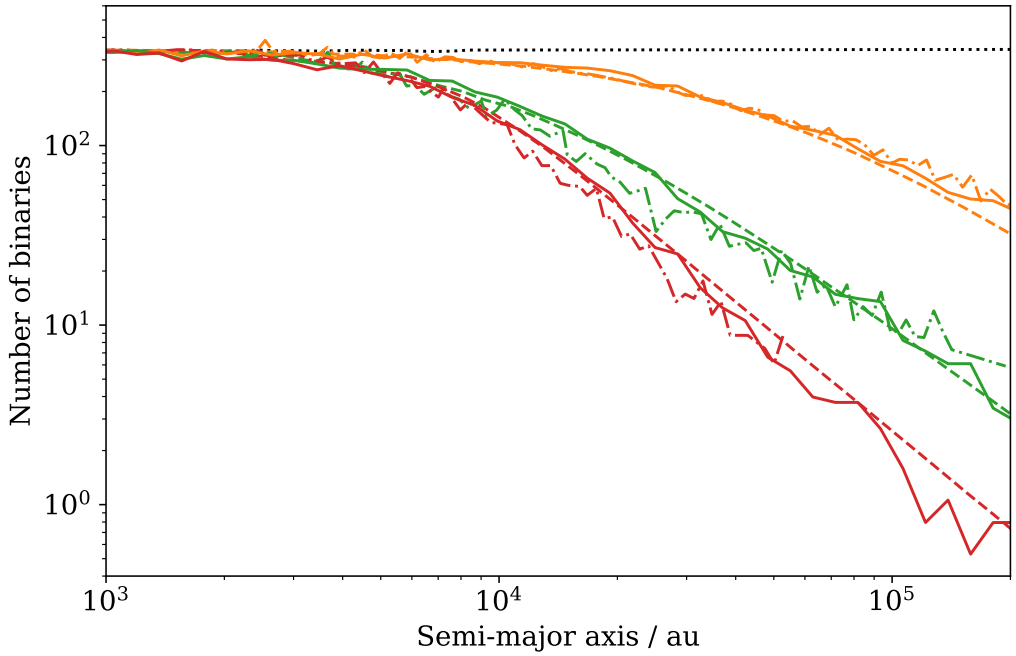

Figure 3.8: The semi-major axis distribution of 10^5 binaries with total binary mass $M_\mathrm{b} = 1M_\odot$ after 10Gyr of evolution in a sea of perturbers with masses $10M_\odot$ (orange lines), $100M_\odot$ (green lines) and $1000M_\odot$ (red lines); perturber density $0.009M_\odot\mathrm{pc}^{-3}$ and relative velocity dispersion $\sigma_\mathrm{rel} = 220\mathrm{kms}^{-1}$. The distribution of the binary semi-major axes before the 10Gyr of evolution is given by the black dotted line. The dashed lines show final results from Yoo et al. [84], the dot-dashed lines show results from Monroy-Rodríguez and Allen [86] and the solid lines show our own results for binaries that are bound for the duration of the simulation.

a larger effect.

The effect of including unbound and rebound binaries is non-negligible however, as can be seen in Fig. 3.9. For the larger PBH masses shown in this figure ($100M_\odot$ and $1000M_\odot$), including unbound and rebound binaries drastically increases the number of binaries present at larger semi-major axes. This will have the effect of weakening our final constraints. Because of this significant difference, unbound and rebound binaries will be kept in our final analysis. In Chapter 4 we describe how constraints on the halo dark matter fraction are calculated using these semi-major axis distributions.

3.5.1 Reproduction of previous results

Our attempts to reproduce previous work are given in this section. We were able to reproduce the transition separation and final distributions from Yoo

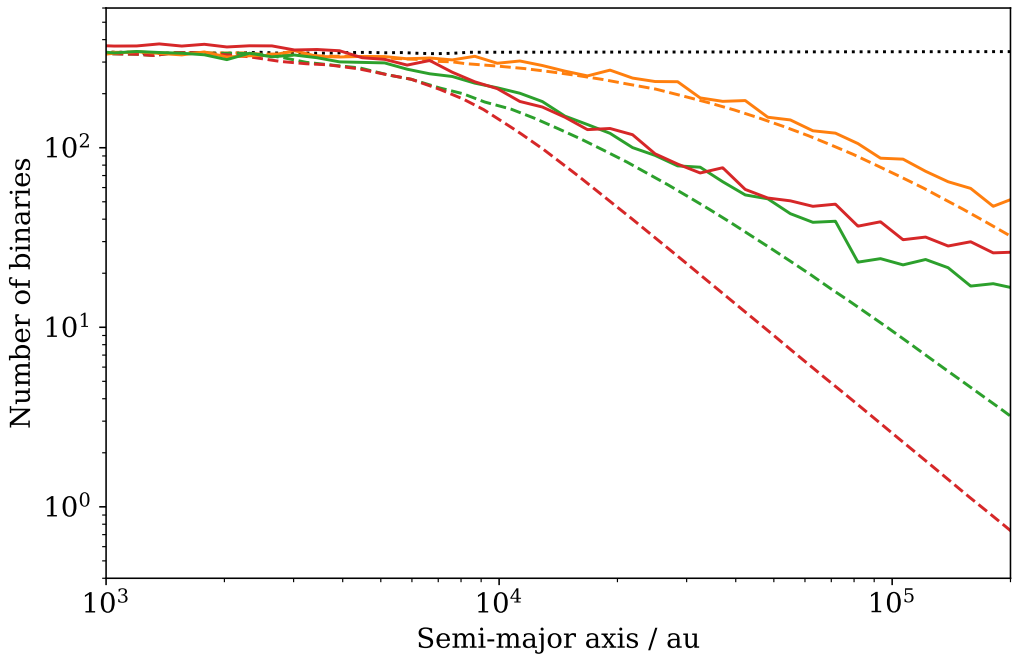

Figure 3.9: The semi-major axis distribution of 10^5 binaries with total binary mass $M_\mathrm{b} = 1M_\odot$ after 10Gyr of evolution in a sea of perturbers with masses $10M_\odot$ (orange lines), $100M_\odot$ (green lines) and $1000M_\odot$ (red lines); perturber density $0.009M_\odot\mathrm{pc}^{-3}$ and relative velocity dispersion $\sigma_\mathrm{rel} = 220\mathrm{kms}^{-1}$. The distribution of the binary semi-major axes before the 10Gyr of evolution is given by the black dotted line. The dashed lines show final results from Yoo et al. [84] and the solid lines show our own results for all binaries, including those that are unbound for any part of the simulation.

et al. [84] and the survival probability as a function of time from Bahcall et al. [39]. We also test the accuracy of the average energy change equations given in Weinberg et al. [101] and the validity of including only the 100 closest encounters between binaries and perturbers.

Transition separation

The transition separation a_t is the semi-major axis below which binaries are insensitive to encounters with PBHs, as defined by Yoo et al. [84]. Yoo et al. [84] find an expression for the transition separation by equating the change in velocity of a star due to an encounter at $b_{\min}$ in the tidal regime ($b_{\min} \gg a$) with the internal velocity of the binary system,

$$\frac{2GM_{\rm p}a}{b_{\min}^2 V_{\rm rel}} \sim \sqrt{\frac{GM_{\rm b}}{a}}, \tag{3.21}$$

where the right hand side is an approximation of Eq. (2.9) and the left hand side is an approximation of Eq. (2.24) in the tidal regime where the impact parameters $\mathbf{b}_i$ are almost equal and the velocity change of the system $\Delta\mathbf{V}$ is dependent on the difference between the two impact parameters $\mathbf{b}_1 - \mathbf{b}_2 \sim a$. Substituting in Eq. (3.5) for $b_{\min}$ gives [84],

$$a_t \sim \left(\frac{M_{\rm b}}{4\pi^2 G\rho^2 T}\right)^{1/3}, \qquad b_{\min} \gg a. \tag{3.22}$$

In the Coulomb regime, the velocity change is given by multiplying Eq. (2.29) by Eq. (2.26) and integrating over b between $b_{\min}$ and a. Equating the resulting expression with the internal velocity of the binary gives,

$$a_t \sim \frac{16\pi G^2 \rho M_{\rm p} T}{V_{\rm rel}} \ln\Lambda, \qquad b_{\min} \ll a, \tag{3.23}$$

where $\ln\Lambda \equiv \ln a/b_{\min}$ is the Coulomb logarithm. For our canonical parameters, and approximating $\ln\Lambda = 1$, the transition separation evaluates to,

$$a_t \sim \begin{cases} 3000\text{au}\left(\frac{M_{\rm p}}{1000M_\odot}\right)^{-1}, & M_{\rm p} < 700M_\odot, \\ 18000\text{au}, & M_{\rm p} > 700M_\odot, \end{cases} \tag{3.24}$$

for a total binary mass of $1M_{\odot}$. In the tidal regime, where $b_{\min} \gg a$, the binary is affected most by the closest encounter so binaries with separation smaller than the transition separation are unlikely to experience a large semi-major axis change and are unlikely to be broken during simulations. When we plot this equation in Fig. 3.10 we choose the value of the Coulomb logarithm to make it continuous.

Figure 3.10 shows results from our own simulations: the fraction out of 1000 binaries that are broken from a single encounter at the minimum impact parameter (Eq. (3.5)), plotted against perturber mass and semi-major axis. Binaries in the white region are insensitive to perturbations since they are not broken by a single encounter at the minimum impact parameter. This plot agrees well with the predictions of Eq. (3.24), also plotted on Fig. 3.10: below $\sim 700M_{\odot}$ the transition separation goes as the inverse of the perturber mass, while for perturber masses larger than $\sim 700M_{\odot}$, the transition separation remains constant at ~ 18000au.

Figure 3.11 shows the fraction of times a binary with a given separation will break at that separation, this is the break frequency (blue line). For low separations this is zero, because these binaries have separation smaller than the transition separation. The break frequency increases with increasing separation after $r \sim 1$pc, up to a value of $r \sim 30$pc, dropping to zero when the binary separation becomes large enough to move the encounters back into the diffusive regime. This frequency is reflected in the separation frequency distribution (orange line). Where binaries are not easily broken by perturbers, the separation frequency is large, and where the break frequency is smaller but non-zero, there are small numbers of binaries with the corresponding separations over the 10Gyr simulation.

Survival probability

Bahcall et al. [39] predict the probability of a binary's survival as a function of time. They use Eq. (2.24) to approximate the half-life of the binaries and

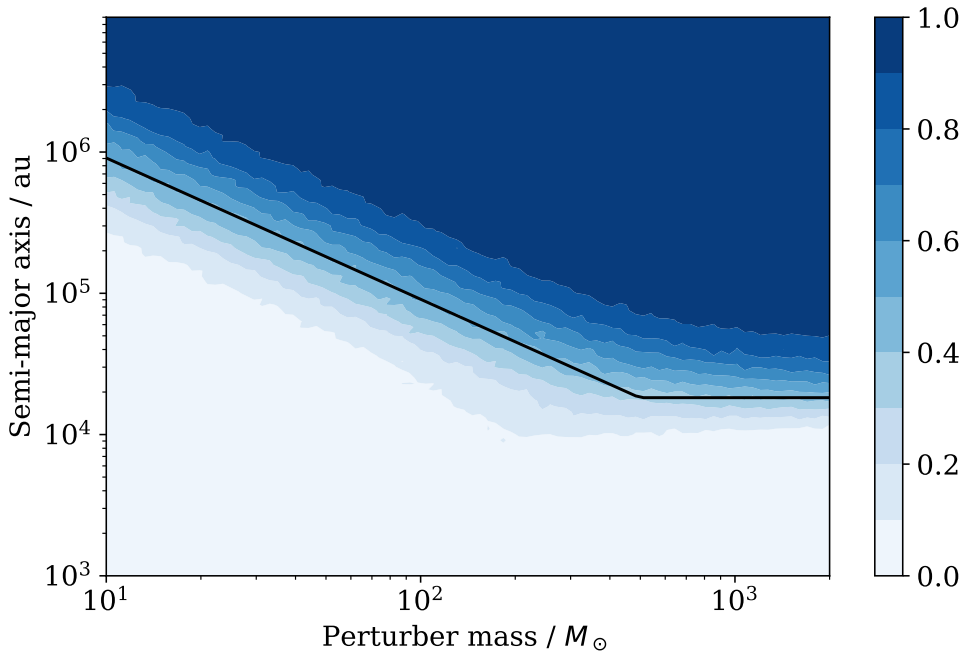

Figure 3.10: The fraction out of 1000 binaries that are broken from a single encounter with a PBH at the minimum likely impact parameter, $b_{\rm min}$ (Eq. (3.5)), plotted against perturber mass and binary semi-major axis for a total binary mass of $M_{\rm b} = 1M_\odot$, binary eccentricity $e = 0.7$, PBH velocity dispersion $\sigma_{\rm rel}$ =220kms^{-1} and perturber density $\rho = 0.009M_\odot{\rm pc}^{-3}$. The black line is the transition separation given by Eq. (3.24). The low-mass part of Eq. (3.24) has been multiplied by 4 for continuity with the high-mass part.

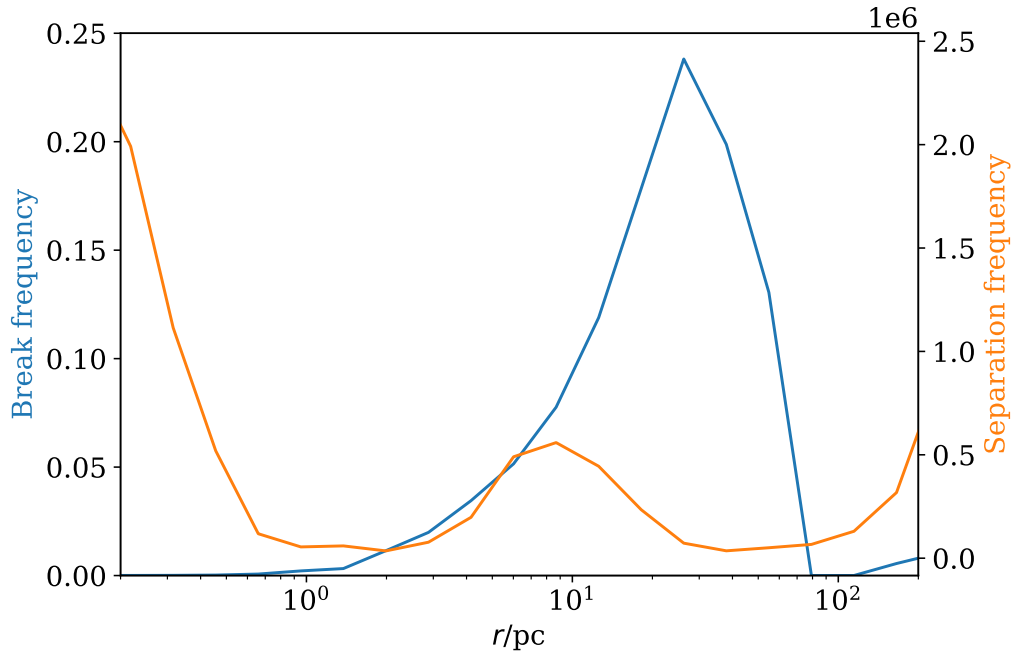

Figure 3.11: The fraction of times a binary with separation r breaks at separation r (blue line) and the total number of times all binaries, with initial semi-major axis 1pc, have had separation r (orange line) over 10Gyr in a sea of perturbers with mass $M_{\rm p} = 100M_\odot$, density $\rho = 0.009M_\odot{\rm pc}^{-3}$ and velocity dispersion $\sigma_{\rm rel} = 220{\rm km\ s}^{-1}$.

predict an exponential decay function for the survival probability using the calculated half-lives. In the small impact parameter regime they find that their simulation results agree with this prediction but the exponential decay doesn't take into account the effects of diffusive encounters. Figure 3.12 shows their simulation results and the results from our simulations.

In our simulations less binaries are broken than in simulations by Bahcall et al. [39]. We believe that the reason for this discrepancy is the distribution from which the relative speed of the PBH and binary during an encounter is drawn. Bahcall et al. [39] draw their relative encounter speed from a Maxwellian distribution, we are reasonably sure that an extra factor of $V_{\rm rel}$ should be included in the probability density distribution to take into account the fact that faster perturbers travel further and have proportionally more encounters. Our results with (blue line) and without (orange line) the extra factor of $V_{\rm rel}$ are shown in Fig. 3.12. The orange line is remarkably consistent with Bahcall et al. [39]'s results, within random variation.

Average energy change

We tested our simulations further by calculating the average energy change of large numbers of encounters and comparing this average with the theoretical values given by Eq. (2.24), which only apply for either very large or very small impact parameters. The energy change due to an encounter (Eq. (2.25)) can be split into two parts, the first order part and the second order part. Theoretically the first order term averages to zero so calculations of the average energy change only need to include the second order term. The variance of the energy change is large however, so to see the first order term average to zero at large impact parameters we would need to simulate more encounters than is practical. The second order term converges much more quickly, so we compared the average of the second order term of the energy change for 10^6 encounters with the theoretical energy change from Weinberg et al. [101], the results are shown in Fig. 3.13.

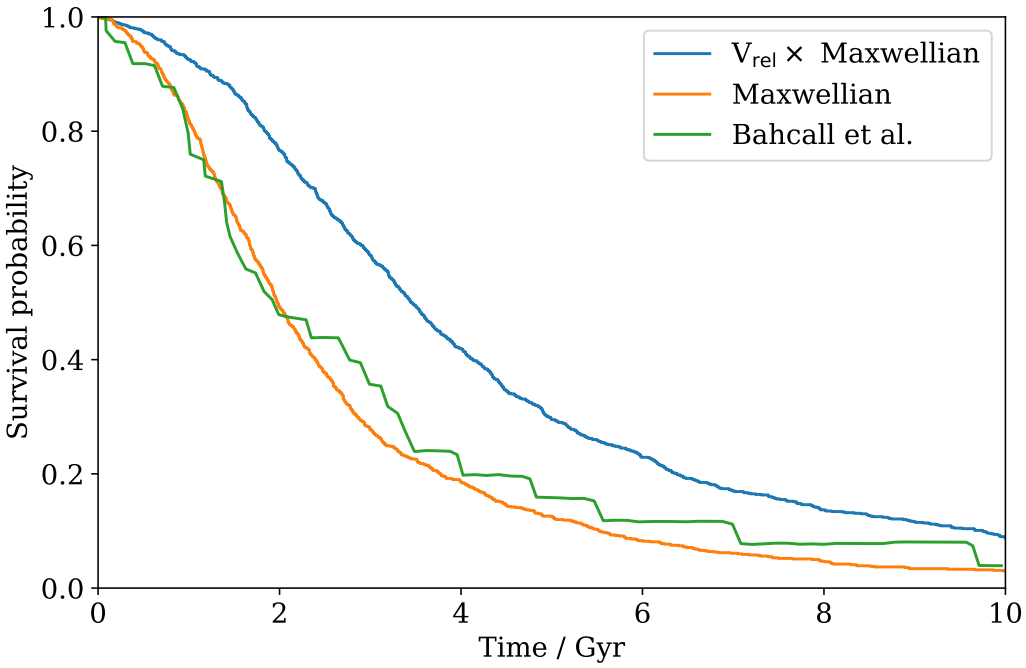

Figure 3.12: The survival probability or fraction of binaries that have survived in a sea of perturbers with mass $3M_\odot$, as a function of time. The binaries start with a semi-major axis of 0.1pc and eccentricity of 0.7, their total mass is $M_b = 2M_\odot$, the relative velocity dispersion of the PBHs is $\sigma_{rel} = (100/\sqrt{3})\text{kms}^{-1}$ and the perturber density is $\rho = 0.1M_\odot\text{pc}^{-3}$, these parameters were chosen to match Bahcall et al. [39]. The blue line is our simulation results for relative encounter speeds drawn from a distribution $\propto V_{rel}^3 \exp\left(-V_{rel}^2/\sigma_{rel}^2\right)$, the orange line is the same as the blue line but with one fewer factor of V_{rel} (i.e. Maxwellian), and the green line is the simulation results from Bahcall et al. [39].

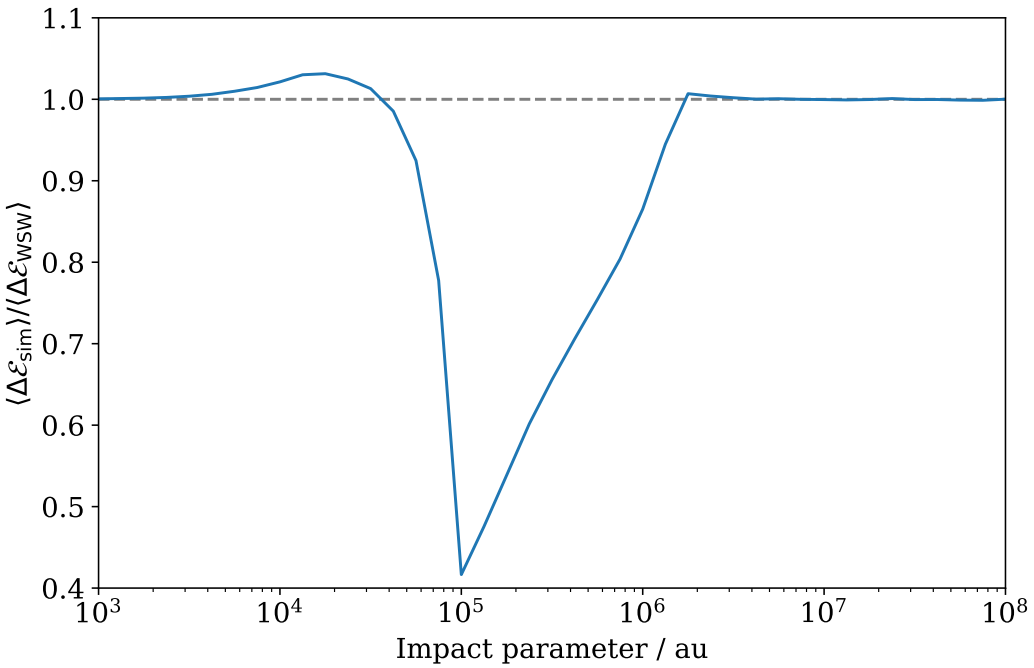

Figure 3.13: The average energy change calculated from simulations of 10^6 encounters divided by the theoretical average energy change from Weinberg et al. [101] plotted against impact parameter. The simulations use perturber mass $M_{\rm p} = 3M_\odot$, relative velocity dispersion $\sigma_{\rm rel} = 220{\rm kms}^{-1}$, total binary mass $M_{\rm b} = 2M_\odot$, dark matter density $\rho = 0.009M_\odot{\rm pc}^{-3}$ and binary semi-major axis $a = 10^5$au.

From Fig. 3.13, the approximation that the impact parameter b is much larger or smaller than the binary semi-major axis a only holds for $b \lesssim 0.01a$ and $b \gtrsim 10a$. The discontinuity at 10^5au is due to the change in regime between the two equations, but we are unsure as to the cause of the discontinuity at $\sim 2\times10^6$au. It is likely to be an artefact of the low resolution of this simulation in impact parameter space.

For the parameters used in Fig. 3.13, the minimum likely impact parameter is $0.0141a$ and the maximum impact parameter is $2.70a$. Since all relevant encounters have $0.01a < b < 10a$, the equations for the average energy change from Weinberg et al. [101] are invalid for detailed simulations of binary disruption. This confirmation that our average energy change is correct for $b \gg a$ and $b \ll a$ has given us further confidence that our simulations are working correctly.

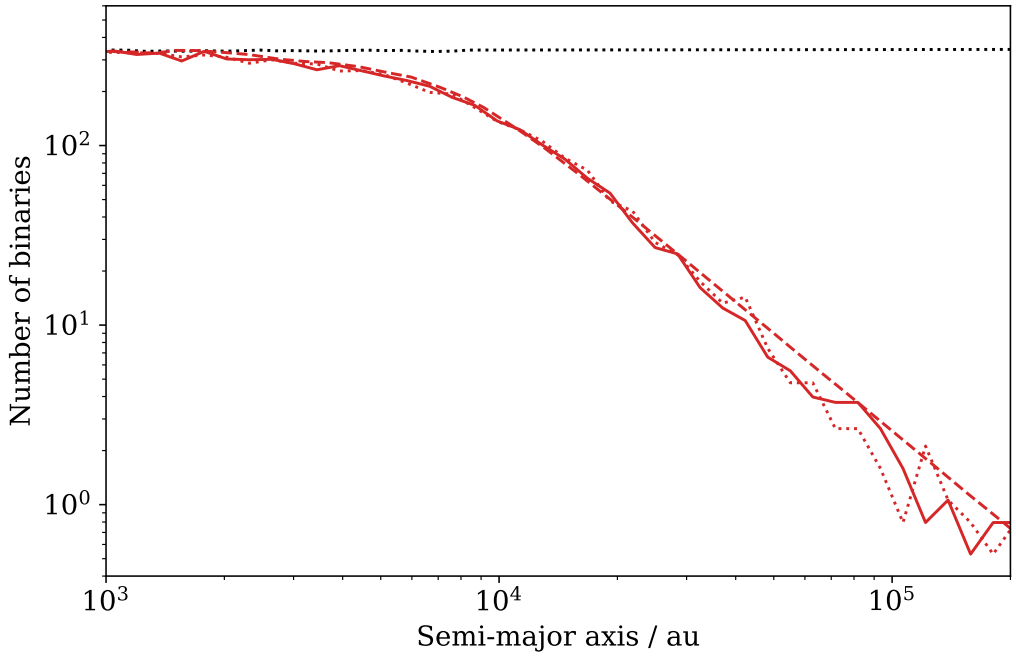

Figure 3.14: Our simulation of only the 100 closest encounters for perturber mass $M_\mathrm{p} = 1000 M_\odot$ (red dotted line), for comparison with results from Yoo et al. [84] (red dashed line) and our simulations for all encounters out to b_max (red solid line). For our simulations here, unbound binaries have been removed. Each binary has a total mass of $M_\mathrm{b} = 1 M_\odot$, the PBHs have mass density $\rho = 0.009 M_\odot \mathrm{pc}^{-3}$ and relative velocity dispersion is $\sigma_\mathrm{rel} = 200 \mathrm{km\ s}^{-1}$.

100 closest encounters

Figure 3.14 shows results from simulating only the 100 closest encounters for the $M_\mathrm{p} = 1000 M_\odot$ case in order to compare directly with Yoo et al. [84]. Their initial distribution is shown by the black dotted line in Fig. 3.14, the fitted curves for their evolved distribution is the dashed line. In the tidal regime ($M_\mathrm{p} \gtrsim 700 M_\odot$), where Yoo et al. [84] simulate only the 100 closest encounters, their simulations give similar results to both our simulations that compute encounters out to b_max (solid line) and our simulations of only the 100 closest encounters (dotted line). This suggests that their approximation that only the 100 closest encounters contribute in the tidal regime is valid.

Chapter 4

Calculating Constraints

In this chapter we discuss our method for calculating constraints on the PBH dark matter fraction from the simulated binary distribution. In Sec. 4.1, we describe how we calculated and use our scattering matrix, allowing us to test many different initial binary distributions quickly. The initial distributions that we test are discussed in Sec. 4.2, and our statistical analysis, a modified version of the χ^2 method, is given in Sec. 4.3. In Sec. 4.4, we justify our use of binary projected separations to compare our simulated and observed binaries and we discuss an appropriate lower cut-off to apply to the observed binaries in Sec. 4.5. We discuss the re-scaling of our constraints to take into account the non-uniform dark matter density in Sec. 4.6. Our final constraints are discussed in Sec. 4.8, along with the current status of constraints on PBHs as dark matter. Results from our analysis using only the 25 most halo-like binaries are given in Sec. 4.7.

4.1 Scattering matrix

Since the initial semi-major axis distribution of halo wide binaries isn't well known [See introduction of 113] we need a way to test different initial distributions quickly without re-running our simulations. To do this we use a scattering matrix $\mathbf{S}$, following Yoo et al. [84], where $S_{ij}(M_{\rm p}, \rho)$ is the number of binaries with initial semi-major axis a_i that have final projected separation r_j for a simulation with perturber mass $M_{\rm p}$ and dark matter density ρ. We're able to

do this because each simulated binary evolves independently, allowing us to effectively put together whichever combination of simulated binaries we need in order to create the correct initial semi-major axis distribution. To calculate the expected number of binaries with projected separation r_j, $P(r_j, M_\mathrm{p}, \rho)$, we multiply the scattering matrix by the initial semi-major axis distribution [84, Eq. (15)] and normalise the resulting vector so that its sum across the bins in which there are observed binaries is equal to the number of observed binaries in our sample,

$$P(r_j, M_\mathrm{p}, \rho) \propto S_{ij}(M_\mathrm{p}, \rho) a_j q(a_j), \tag{4.1}$$

where a, is the array of semi-major axis bins and $q(a)$, is the probability density of the initial semi-major axis distribution. The extra factor of a_j is necessary here because our semi-major axis bins are logarithmically spaced. To test our scattering matrix we compared the final projected separation distribution directly from the simulations with the corresponding $P(M_\mathrm{p}, \rho)$, using a log flat initial semi-major axis distribution as used in our simulations and confirmed that the two distributions match.

4.2 Initial semi-major axis distribution

The scattering matrix allows us to test any initial semi-major axis distribution but we need to choose a parameterisation. Previous work on wide binary disruption [84–86, 101, 102] used a power law distribution, $\propto a^{-\alpha}$, the simplest generalisation of Oepik's Law: a log flat distribution found to theoretically model dynamical equilibrium [114]. Oepik's law has also been found to match the distribution of several different samples of wide binaries out to semi-major axes of $\sim$ 3000au [115].

One problem with this distribution, however, is that it isn't motivated by formation mechanisms of halo wide binaries. For very wide binaries, with semi-major axis $>$ 10000au, the mechanisms are not well understood but binaries this wide are expected to be very rare with a distribution that falls off steeper

$F_{\rm dim}$	α
1.6	0.90
2.0	0.71
2.6	-0.36
3.0	-0.80

Table 4.1: The fitted power law α to Griffiths [116] Fig. 5.7 for the different values of the fractal dimension of the simulated star cluster.

than log flat. Griffiths [116] investigates possible mechanisms for binaries with such large semi-major axes and finds that formation from the dissolution of large clusters is able to contribute to some of the wide binary population. Binaries formed in this way become bound when a cluster of stars disperses and the binding force between the stars and the cluster becomes smaller than the force between the two stars.

We found that a power law distribution is a good fit to the wide binary distributions from Griffiths [116] Fig. 5.7, which are calculated based on simulations of cluster dissolution. Our power law fits are given in Table 4.1 and plotted in Fig. 4.1. The first column in Table 4.1 is the fractal dimension of the initial star cluster. Increasing the fractal dimension decreases the amount of substructure, with $F_{\rm dim} = 3$ describing an initially homogeneous distribution [113]. The second column is the power law we fitted to the distribution, α. When we vary α to fit our simulated distributions to observational data we will allow it to vary between 0.7 and 2, since in reality, $F_{\rm dim}$ is no larger than 2, and the best fit distribution never has α as large as 2. This range will take into account contributions to the initial distribution from this formation mechanism.

This distribution is not complete without a primordial binary population. Primordial binaries are formed during star formation from the fragmentation of pre-stellar cores [e.g. Ref. 116]. The primordial population is included by adding a log normal distribution with mean $\mu = 100$au and log width $\sigma = 1.5$

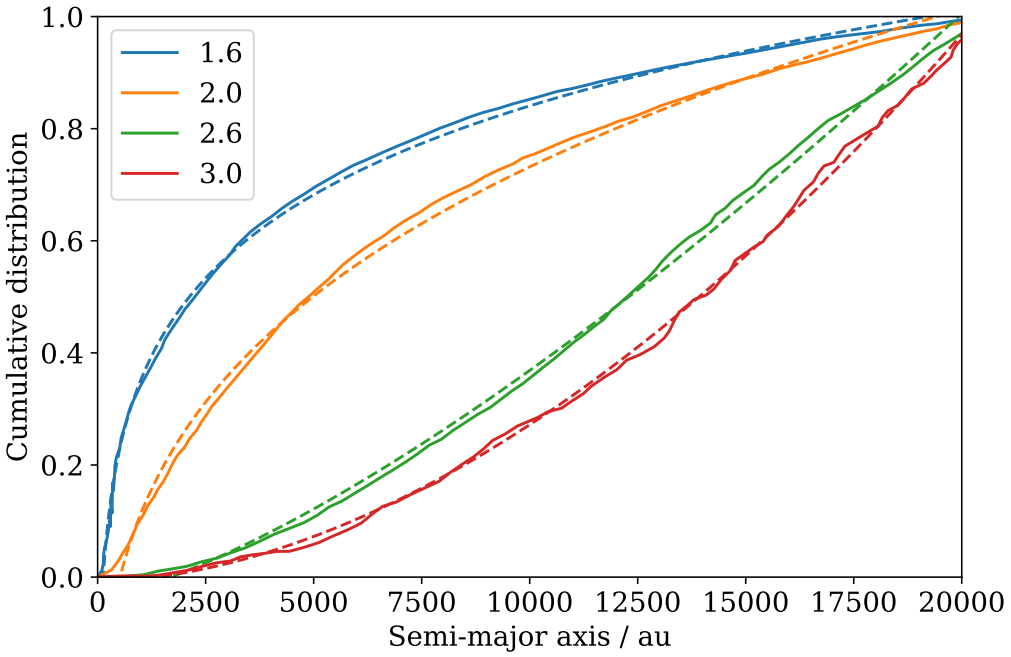

Figure 4.1: Power law fits to Griffiths [116] Fig. 5.7 semi-major axis cumulative distribution function for different values of the fractal dimension, F_{dim}, of the simulated star cluster. The blue, orange, green and red lines correspond to fractional dimensions 1.6, 2.0, 2.6 and 3.0, respectively. The solid lines are from Ref. [116] Fig. 5.7 and the dashed lines are our power law fits. The fitted power law exponents, α, are given in Table 4.1.

[117]. The resulting form of the initial semi-major axis probability density is,

$$q(a) = \begin{cases} \frac{A(a/\mathrm{au})^{-\alpha}}{\log(a_{\max}/a_{\min})} \\ \qquad + \frac{1-A}{\sqrt{2\pi}\sigma(a/\mathrm{au})} \exp\left(-\frac{(\log(a/\mathrm{au})-\mu)^2}{2\sigma^2}\right), & \text{if } \alpha = 1, \\ \frac{A(1-\alpha)(a/\mathrm{au})^{-\alpha}}{(a_{\max}/\mathrm{au})^{1-\alpha}-(a_{\min}/\mathrm{au})^{1-\alpha}} \\ \qquad + \frac{1-A}{\sqrt{2\pi}\sigma(a/\mathrm{au})} \exp\left(-\frac{(\log(a/\mathrm{au})-\mu)^2}{2\sigma^2}\right), & \text{otherwise,} \end{cases} \tag{4.2}$$

where A and α are parameters we will fit for during our analysis, A is a measure of how much of the distribution is log normal ($A = 0$ corresponds to all log normal, $A = 1$ corresponds to all power law) and α is the power law exponent. The parameters $a_{\min}$ and $a_{\max}$ are the minimum and maximum semi-major axes of the distribution, used for normalisation. We use $a_{\min} = 30\mathrm{au}$ and $a_{\max} = 2 \times 10^4 \mathrm{pc}$ in order to be able to accommodate all the results from our simulations for a variety of different parameters. Since the distribution from the scattering matrix is normalised to match the number of observed binaries across the observed bins, the only effect of altering $a_{\min}$ and $a_{\max}$ is to re-scale A.

The best fit values for α and A as a function of perturber mass and halo density are plotted in Fig. 4.2. See Sec. 4.3 for a description of the statistics used to determine the best fits. The white cross shows the global best fit at $M_{\mathrm{p}} = 30M_{\odot}$ and $\rho = 0.012M_{\odot}\mathrm{pc}^{-3}$, the maximum density we simulated, the value of the local dark matter density is well measured and unlikely to be larger than this [118]. For the majority of the parameter space a pure power law distribution is preferred ($A = 1$) with $1.20 \lesssim \alpha \lesssim 1.65$, but for mid-range perturber masses ($M_{\mathrm{p}} \sim 200M_{\odot}$) a partially log normal distribution is favoured, with a power law $\alpha \lesssim 1$.

Figure 4.3 shows an example of our hybrid distribution. We find that for a perturber mass of $100M_{\odot}$ and a dark matter density of $0.009M_{\odot}\mathrm{pc}^{-3}$ the initial distribution parameters that produce a final distribution which best matches the observed distribution are $\alpha = 0.98$ and $A = 0.89$. These parameters were

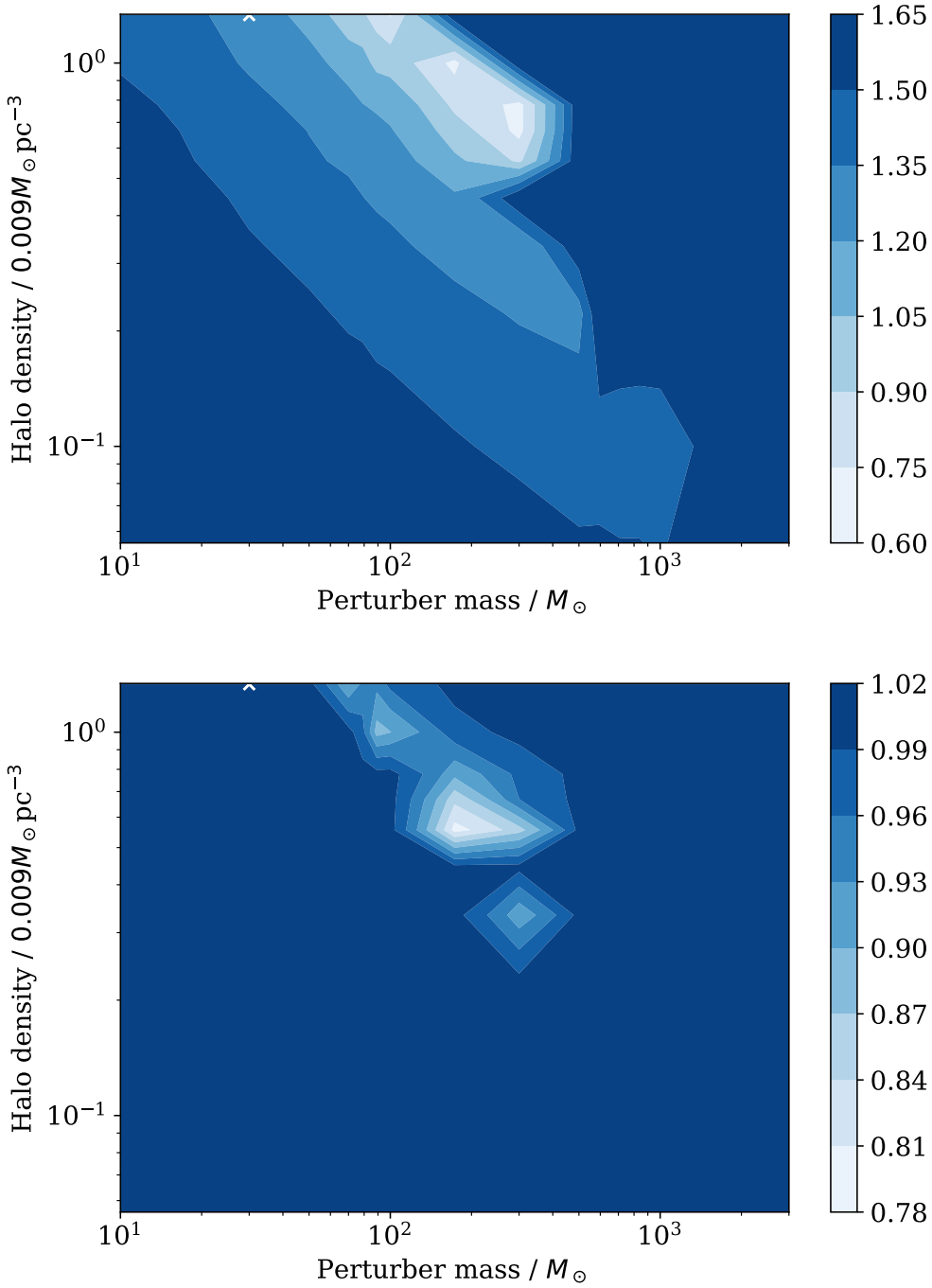

Figure 4.2: The best fit values of α (top) and A (bottom) as a function of perturber mass M_p and dark matter density ρ. The best fit at any given pair of M_p and ρ corresponds with the minimum value of Y^2 (see text) for those parameters. The global best fit is the white cross at $M_\mathrm{p} = 30M_\odot$ and $\rho = 0.012M_\odot\mathrm{pc}^{-3}$.

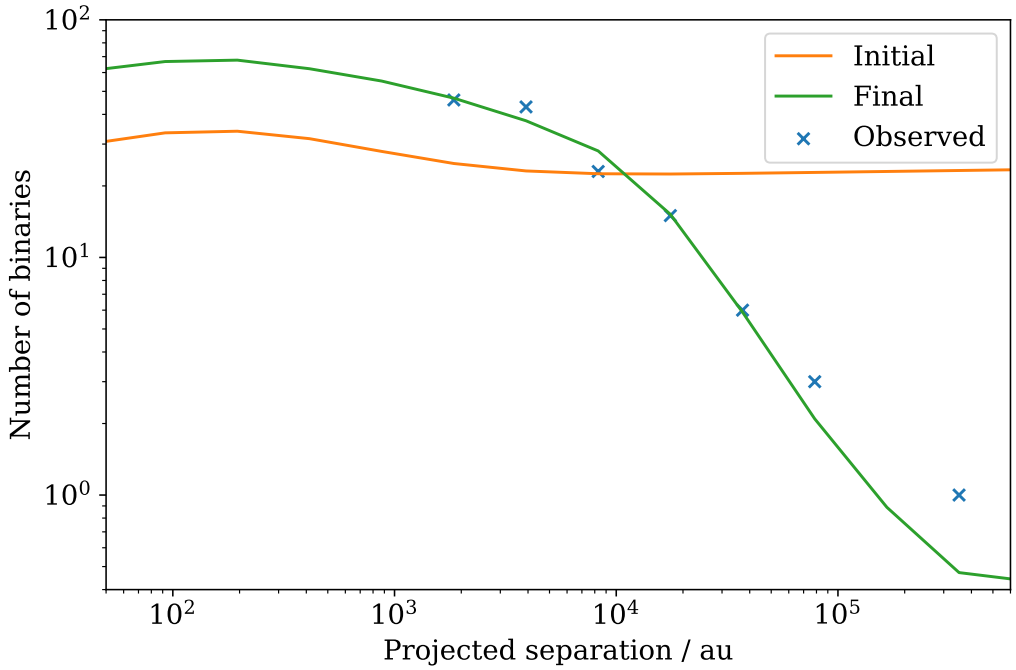

Figure 4.3: The best fit projected separation distribution for perturber mass $M_{\rm p} = 100M_{\odot}$ and dark matter density $\rho = 0.009M_{\odot}{\rm pc}^{-3}$ (green line). The corresponding initial distribution (orange line) has parameters $\alpha = 0.98$ and $A = 0.89$. The blue crosses show the observed binary distribution.

chosen because the best fit for this perturber mass and density has a value of A that is noticeably smaller than 1. The initial distribution, described by these parameters, is shown by the orange line, the green line is the corresponding final distribution and the blue crosses are the observed binary distribution. This projected separation distribution is demonstrative of the semi-major axis distribution because semi-major axes and projected separations are approximately proportional to each other. For projected separations less than about 1000au, the initial distribution is dominated by the log normal part, this drops off at larger projected separations leaving the power law part of the distribution. We will be using this hybrid distribution for the rest of our analysis, our final results will allow A to vary between 0 and 1 but for comparison with previous results we have set $A = 1$ where stated.

4.3 Chi-squared like analysis

Previous work on wide binary disruption used a likelihood analysis [84] or K-S test [86] to compare simulated distributions with observed binary distributions. Both of these methods have weaknesses: likelihood analysis doesn't easily give p-values, and the K-S test is less sensitive to differences in the extremes of distributions. This sensitivity is important because it is often the widest binaries in the sample that contribute most to tightening the constraints in this context.

Here we have chosen to use a modified version of the χ^2 test. The χ^2 test readily provides p-values, allowing us to calculate 2σ and 3σ contours and it is equally sensitive at the extremes of the distributions as at the median. The χ^2 test has its own weaknesses, however, it compares binned data and it is invalid if the number of samples in those bins is small ($\lesssim 5$). The χ^2 statistic is given by [112, Eq. (14.3.1)],

$$\chi^2 = \sum_i \frac{(N_i - n_i)^2}{n_i}, \tag{4.3}$$

where N_i is the number of observed binaries in the ith bin and n_i is the expected number of binaries in the ith bin, calculated from the scattering matrix. The sum is over all bins with non-zero N_i.

Since we're dealing with small numbers of binaries in some cases, we use a modified version of the χ^2 test: the Y^2 test [119]. The Y^2 statistic re-scales the χ^2 statistic so that its variance is fixed to be equal to twice its mean, even in the case where there are small numbers of binaries [see 112, Sec. 14.3.2 for more details]. The Y^2 statistic [119, Eq. (5)],

$$Y^2 = \nu + \sqrt{\frac{2\nu}{2\nu + \Sigma_i n_i^{-1}}} \left(\chi^2 - \nu\right), \tag{4.4}$$

where ν, the number of degrees of freedom, is equal to the number of bins that are compared minus one if the n_i's have been normalised to match the N_i's and minus one for each fitted parameter.

Our analysis is as follows, first we calculate Y^2 for every combination of

perturber mass $M_{\rm p}$, dark matter density ρ, A and α. Then for each $M_{\rm p}$, ρ pair we find the minimum value of Y^2: $Y^2_{\rm min}(M_{\rm p}, \rho)$. We confirm that the absolute best fit is a sufficiently good fit by comparing the absolute minimum Y^2: $Y^2_{\rm min}$, which is the minimum value of $Y^2_{\rm min}(M_{\rm p}, \rho)$, with the number of degrees of freedom for the analysis, ν. In this case ν is the number of bins compared (7) minus one because we have normalised the simulated distribution to match the observed one, minus two for the two parameters we have fitted (A and ρ). Our minimum Y^2 value is less that 3, so the best fit distribution is a good fit and we can continue our analysis.

To obtain constraints on the dark matter density as a function of perturber mass we need to compare the variation in Y^2 from the minimum value,

$$\Delta Y^2(M_{\rm p}, \rho) = Y^2_{\rm min}(M_{\rm p}, \rho) - Y^2_{\rm min}, \tag{4.5}$$

with the variation that corresponds to contours of 2σ and 3σ:

$$\Delta Y^2_{2\sigma} = \text{inverse}\left(1 - \text{cdf}(0.0455)\right), \tag{4.6}$$

$$\Delta Y^2_{3\sigma} = \text{inverse}\left(1 - \text{cdf}(0.00270)\right), \tag{4.7}$$

where cdf is the cumulative distribution function of the χ^2 distribution with 2 degrees of freedom. The two degrees of freedom correspond to the two dimensions of parameter space we are calculating the contours in ($M_{\rm p}$ and ρ). To calculate the position of the 2σ contour for a particular $M_{\rm p}$ we find the value of ρ that gives $\Delta Y^2(M_{\rm p}, \rho) = \Delta Y^2_{2\sigma}$. The p-values calculated by this method as a function of perturber mass and halo density are plotted in Fig. 4.4. The black solid and black dotted lines correspond to p-values of 0.05 and 0.003, or equivalently, 2σ and 3σ constraints, respectively. The overall best fit distribution to the observed binaries is indicated by a white cross, with the p-values decreasing outwards from that point.

Due to time constraints we were unable to achieve very high resolution in ρ, making it unlikely that we would find values of $\Delta Y^2(M_{\rm p}, \rho)$ that are almost

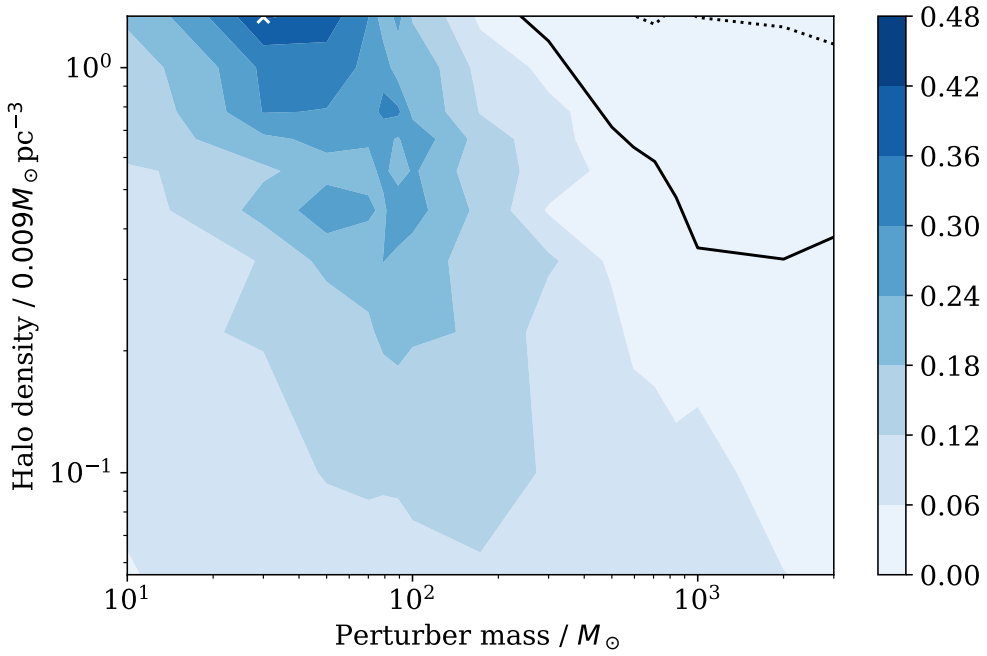

Figure 4.4: P-values calculated from Y^2 (see text) as a function of perturber mass M_p and halo density ρ. Values below 0.05 and 0.003, shown by the black solid and dotted lines, are excluded at 2σ and 3σ, respectively. The best fit to the observed binary distribution is indicated with a white cross. The values of the initial distribution parameters, α and A, are chosen to minimise Y^2, see Fig. 4.2.

equal to $\Delta Y^2_{2\sigma}$ and $\Delta Y^2_{3\sigma}$. To combat this, for each perturber mass, we fitted a power law to $\Delta Y^2(M_\mathrm{p}, \rho)$ as a function of ρ and inverted the resulting function to give ρ evaluated at $\Delta Y^2_{2\sigma}$ and $\Delta Y^2_{3\sigma}$. This method gives us much smoother and more accurate constraints plots. Other than this interpolation, the main weakness of this analysis method is the use of binned data.

4.4 Projected separation analysis

Previous papers have compared the observed angular separation [e.g. Ref. 84] or semi-major axis [e.g. Ref. 86] distributions with the simulated distributions, but both of these methods have disadvantages. Angular separation is measurable for the observed binaries, but to calculate the angular separation distribution for simulated binaries it's necessary to introduce a distribution for the distances between us and the binaries. Semi-major axes are directly readable from the simulations but to find semi-major axes for the observed

distribution it's necessary to use an eccentricity distribution and randomised viewing angles for the observed binaries.

Projected separations are easily calculated from distance and angular separation measurements for the observed binaries (Eq. (2.19)) and for the simulated binaries we only need to randomise the viewing angles for the binaries in order to find the projected separation from the absolute separation since we are already using an eccentricity distribution as part of the simulations. Comparing projected separations only requires the assumption that the simulated binaries are randomly oriented in the sky.

We tested our analysis code by running it with different random seeds to confirm that the best fit perturber mass is consistent. The resulting ranges of best fit perturber mass are plotted in Fig. 4.5. The median value of the best fit perturber mass is shown by the orange lines for three different versions of our analysis. The first is the projected separation analysis, where the simulated and observed projected separations are compared. The second is the angular separation analysis where the simulated binary distances are drawn from the distance distribution of our observed binary catalog. The third is the angular separation analysis assuming that all binaries are at a fixed distance of 100pc from us, this is only for comparison here in order to check which randomised parameter causes any variability in best fit values.

The best fit perturber mass varies across the entire range of our parameter space for the angular separation analysis indicating that this method is too random for the sample sizes we're using. We find that when we don't randomise the binary distances, by either comparing projected separations or picking an example distance of 100pc, the range of best fits narrows dramatically giving us sufficiently consistent results. Therefore, our final analysis is made by comparing the projected separations of the observed and simulated binaries in order to introduce the least amount of uncertainty in our results.

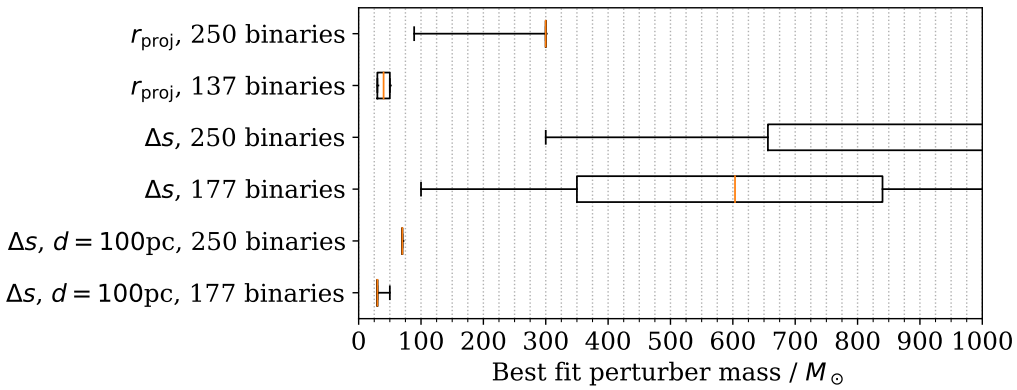

Figure 4.5: The range of best fit perturber masses calculated by comparing projected separations, angular separation with distance drawn from the distribution of observed binary distances, and angular separations with the distance fixed to 100pc. Also shown is the effect of using different projected separation or angular separation cut-offs. The group of 137 binaries is the result of a lower projected separation cut-off of 1273au and the 177 binaries are from a lower angular separation cut-off of 4.7". The whiskers show the full range of the best fit mass values, the boxes show the lower and upper quartiles and the orange lines show the median values.

4.5 Observational data

We use the halo wide binary catalog put together by Allen and Monroy-Rodríguez [106] to calculate our constraints. They searched the literature for high velocity, metal-poor wide binaries, since these are the most likely to be halo binaries. Proper motions were taken from the SIMBAD database and pairs whose proper motions were different by more than the measurement errors were removed. The catalog consists of 111 halo binaries from Allen et al. [120], 110 from Chanamé and Gould [103], 23 from Zapatero Osorio and Martín [121] and 7 from Ryan [122]. The majority of the binaries are originally from Luyten's NLTT catalog [104] which is complete up to a visual magnitude of 19 and for proper motions larger than 180 mas/yr. As a magnitude limited sample it is subject to Malmquist (preferential detection of bright stars), kinematical and Lutz-Kelker (the assumption that stars are distributed uniformly in space) biases. We removed a binary from the catalog that we believe to be a duplicate, the binary with primary star NLTT 29553 and secondary HIP 58962.

Figure 4.6 shows the angular separation and projected separation distributions for 250 of the 251 Allen and Monroy-Rodríguez [106] binaries. To obtain a complete binary sample it is necessary to discard binaries with an angular separation or projected separation below a cut-off. Yoo et al. [84] use a cut-off of 3.5" to ensure their sample of halo wide binaries is complete. A cut-off of a few arcsec reflects the resolving power of the telescope used to observe the sample.

For the binaries that are relevant here (with semi-major axis $>$ 100au), which have a monotonically decreasing initial semi-major axis distribution, the semi-major axis distribution, and therefore the angular separation and projected separation distributions, should decrease monotonically with increasing semi-major axis. Since we are using projected separations for our analysis we will choose a projected separation cut-off rather than an angular separation cut-off. Our cut-off is chosen such that the number of binaries per logarithmically spaced projected separation bin decreases with increasing projected separation, and where the cut-off would split up a projected separation bin, the cut-off has been increased so that no bins are partially filled. The resulting cut-off is at 1273au, we keep binaries with projected separations larger than this leaving us with 137 binaries for our analysis.

Figure 4.7 is a plot of distance against separation for the 250 binaries. Each blue cross represents a binary star and the orange vertical line indicates our lower projected separation cut-off. The white space in the top left corner is due to the resolution of the observations used to put together the catalog, binaries with a low angular separation are not detected. This plot shows that our choice of projected separation cut-off effectively removes this incompleteness.

A final confirmation that this is a suitable choice of lower projected separation cut-off comes from values of Y^2 for populations of binaries with different cut-offs. We found that decreasing the lower cut-off increases the value of Y^2_{min}, and our choice of cut-off at 1273au is the lowest value that allows the observational data to match the simulation results with a sufficiently good fit.

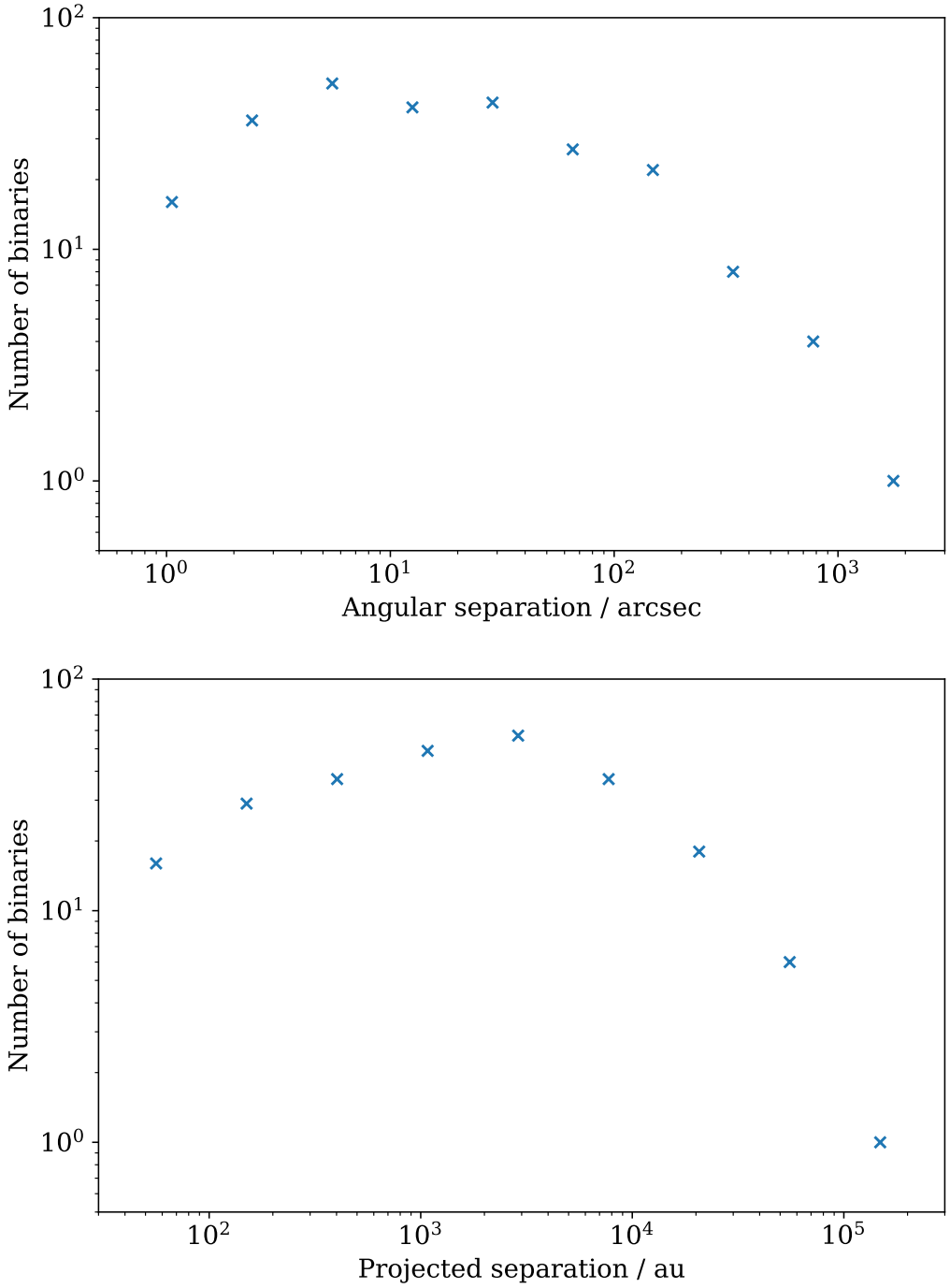

Figure 4.6: The angular separation (top) and projected separation (bottom) distributions of 250 binaries from the Allen and Monroy-Rodríguez [106] catalog.

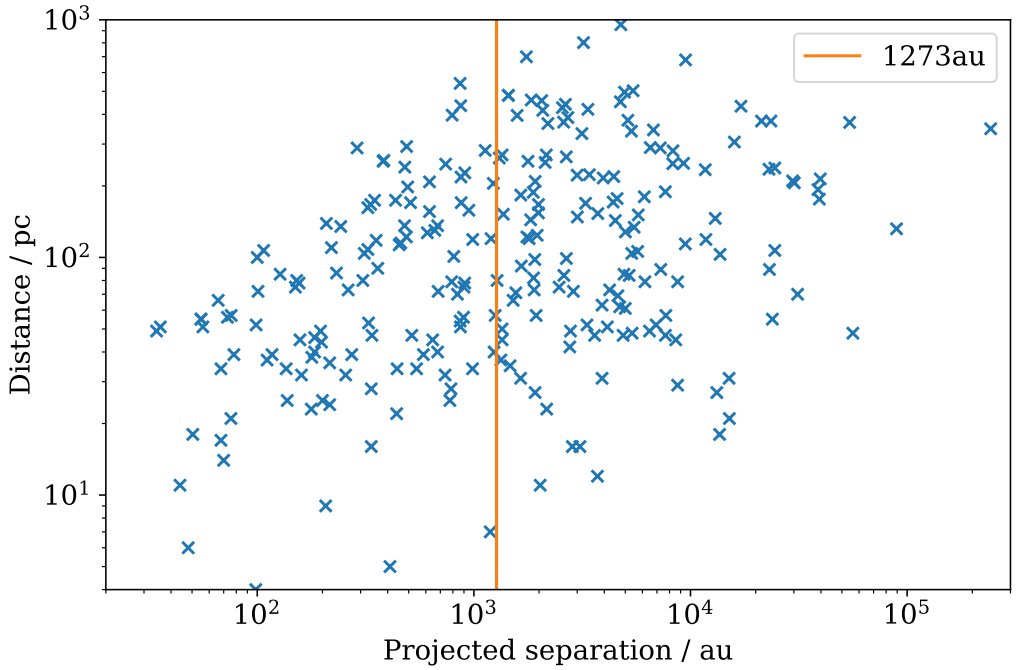

Figure 4.7: Distance plotted against projected separation for the 250 binaries from the Allen and Monroy-Rodríguez [106] catalog. Each blue cross represents a single binary star. The orange line is the projected separation 1273au, the lower cut-off used in our analysis.

Our best fit distribution is shown in Fig. 4.8. This plot shows the distribution which has the smallest Y^2 value (green line) in comparison with the observed distribution (blue crosses). This distribution has perturber mass $M_{\rm p} = 30M_{\odot}$, perturber density $\rho = 0.012M_{\odot}{\rm pc}^{-3}$, and initial distribution parameters $\alpha = 1.26$ and $A = 1.00$. The initial distribution for these values of α and A is also plotted (orange line).

4.6 Re-scaling of constraints

In Sec. 3.2.4 we discussed the necessity of re-scaling our constraints to take into account the variable dark matter density along Galactic orbits. This re-scaling has been suggested before by Quinn et al. [85]. We calculated the time-averaged dark matter density along each binary Galactic orbit, for the binaries in our catalog that have enough data, and found that the mean time-averaged density is $0.0106M_{\odot}{\rm pc}^{-3}$, a little larger than the dark matter density at the solar radius for our model: $0.00754M_{\odot}{\rm pc}^{-3}$. We found that the distribution of

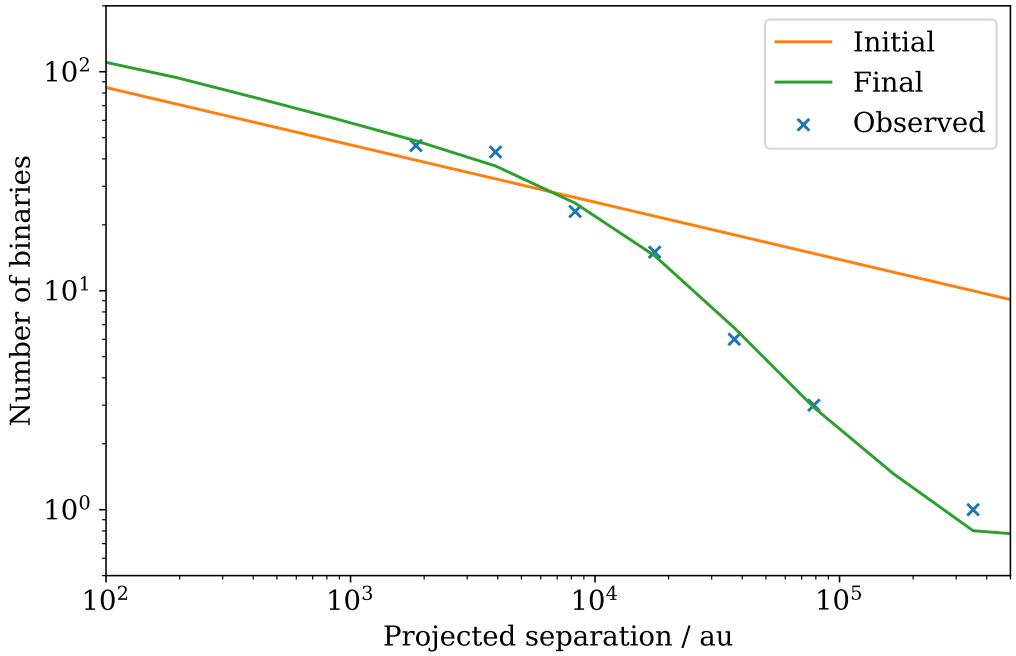

Figure 4.8: The best fit final projected separation distribution (green line) to the observed binary distribution (blue crosses) and the corresponding initial distribution (orange line) which has parameters $\alpha = 1.26$ and $A = 1.00$. The best fit perturber mass is $M_\mathrm{p} = 30 M_\odot$ and the best fit perturber density is $\rho = 0.012 M_\odot \mathrm{pc}^{-3}$.

time-averaged densities is narrow, making this method of re-scaling an accurate approximation. We have re-scaled our constraints by $0.00754/0.0106 = 0.711$ as a result of this, making them slightly tighter.

4.7 25 most halo-like binaries

In Sec. 3.2.5 we discussed how Monroy-Rodríguez and Allen [86] take into account the effects of the Galactic disk by calculating constraints from binaries that spend less time near the Galactic plane. They find that the constraints for their x most halo-like binaries get increasingly tighter as x decreases.

We replicated this analysis by calculating Galactic orbits for the 160 binaries in our sample that have sufficient data in the SIMBAD astronomical database [123]. We used the MWPotential2014 Galactic potential in the `galpy` package [110] to integrate the orbits of 160 binaries back in time by 10Gyr, calculating the fraction of their time they spend within 500pc of the Galactic plane.

Since only 46 binaries in our sample have both projected separation larger than our cut-off (1273au) and enough data to calculate the fraction of time they spend in the disk, we were only able to calculate constraints for the 25 most halo-like binaries for comparison with Monroy-Rodríguez and Allen [86] and not the 50 and 100 most halo-like. The best fit for our 25 most halo-like binaries has a sufficiently small $Y^2_{\rm min}$ value to be a good fit. As shown in Figs. 4.9 and 4.10, our constraints are much weaker than those calculated by Monroy-Rodríguez and Allen [86] but still tighter than those for our full population of 137 binaries.

We tested how variable the best fit perturber mass and halo densities are for random populations of 25 binaries. Our results showed that not only did the best fit perturber mass vary drastically for the different populations, the minimum Y^2 value varied too, sometimes above the allowed value for valid constraints. More tests need to be made to confirm that calculating constraints for the most halo-like binaries in this way is accurate. It's possible that 25 is too small a number of binaries to give trustworthy results. If we had more time we would like to test how the constraints are affected by the number of binaries in the population. It would also be interesting to see how the constraint depends on the widest binary in the sample, since previous studies have found that it's often the widest binary that has the largest effect [e.g. Ref. 85].

It is likely that taking into account interactions with the Galactic disk would make constraints much tighter since the wide binaries would be passing through areas of high density, and a more direct model, such as simulating the Galactic potential [e.g. Ref. 102], might provide more accurate results. This doesn't change our main conclusion: when the effects of unbound binaries and more realistic initial distributions are considered, the constraints become weaker and more information and sophisticated simulations are needed to make progress here.

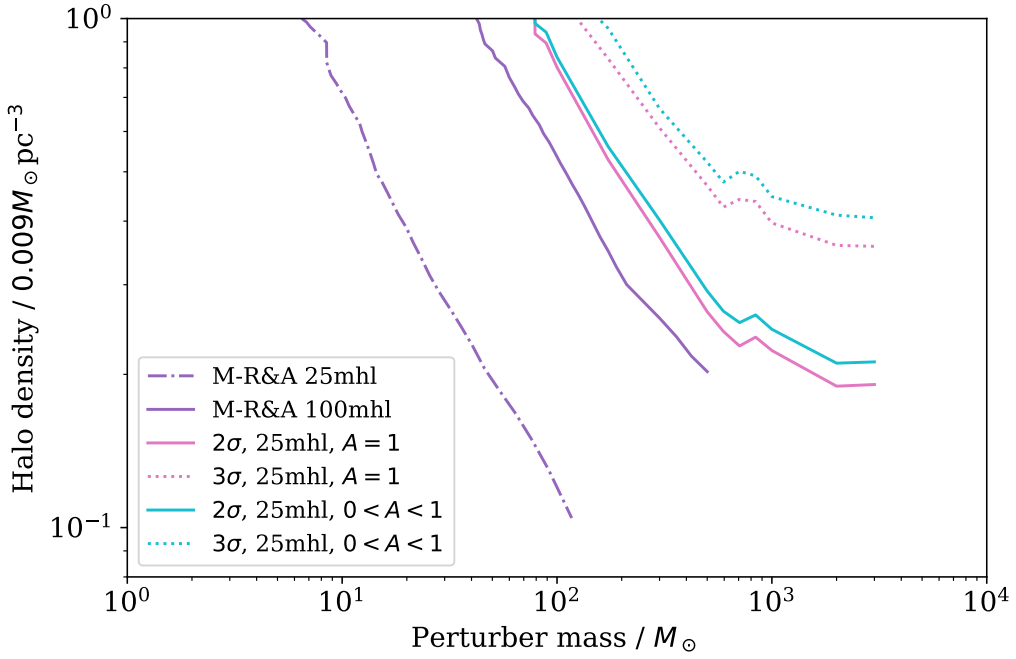

Figure 4.9: The maximum allowed fraction of the halo dark matter density made up of PBHs as a function of the PBH mass. The purple lines are constraints from Monroy-Rodríguez and Allen [86] for their 25 most halo-like (dash-dot line) and 100 most halo-like (solid line) binaries. Our constraints from the 25 most halo-like binaries with projected separation larger than 1273au are plotted in pink, for $A = 1$, and cyan, for $0 < A < 1$. The solid lines are 2σ constraints and the dotted lines are 3σ constraints. A binary is more halo-like if it spends less of its lifetime within 500pc of the Galactic plane [86].

4.8 Constraints

Our final constraints are shown in Figs. 4.10 and 4.11. Figure 4.10 shows our 2σ and 3σ constraints for a power law initial semi-major axis distribution ($A = 1$) and our hybrid distribution ($0 < A < 1$) along with constraints from previous work on wide binaries. The parameter space above the lines is excluded at either the 2σ or 3σ level, as indicated by the caption. Our constraints are much weaker than those calculated by Yoo et al. [84] and Monroy-Rodríguez and Allen [86], being more similar to the constraints calculated by Quinn et al. [85]. We can see that using the hybrid distribution makes the constraints slightly weaker but this effect is very minor. The large difference between our constraints and those calculated previously could be explained by the inclusion of unbound binaries, more realistic initial distributions and the use of a χ^2-like analysis. The inclusion of unbound binaries leads to less perturbed final distributions, this decrease in effectiveness of PBH encounters means that larger mass perturbers are no longer rejected by the constraints.

Our 2σ constraint with $0 < A < 1$ is shown in context with current constraints on PBHs as dark matter in Fig. 4.11. The dynamical constraint on this plot is the 25 most halo-like binaries constraint from Monroy-Rodríguez and Allen [86]. As shown in the previous plot, our constraint is much weaker than previous constraints calculated using wide binaries, and as a result, our new dynamical constraint only excludes a small amount of this PBH mass window. In order to find less conservative constraints on the dark matter fraction of PBHs, it would be necessary to know more information about the initial semi-major axis distribution of halo wide binaries or to use more sophisticated simulations that take into account effects of the Galactic disk and the Galactic tide, perhaps using a simulation of the Galactic potential similar to Jiang and Tremaine [102].

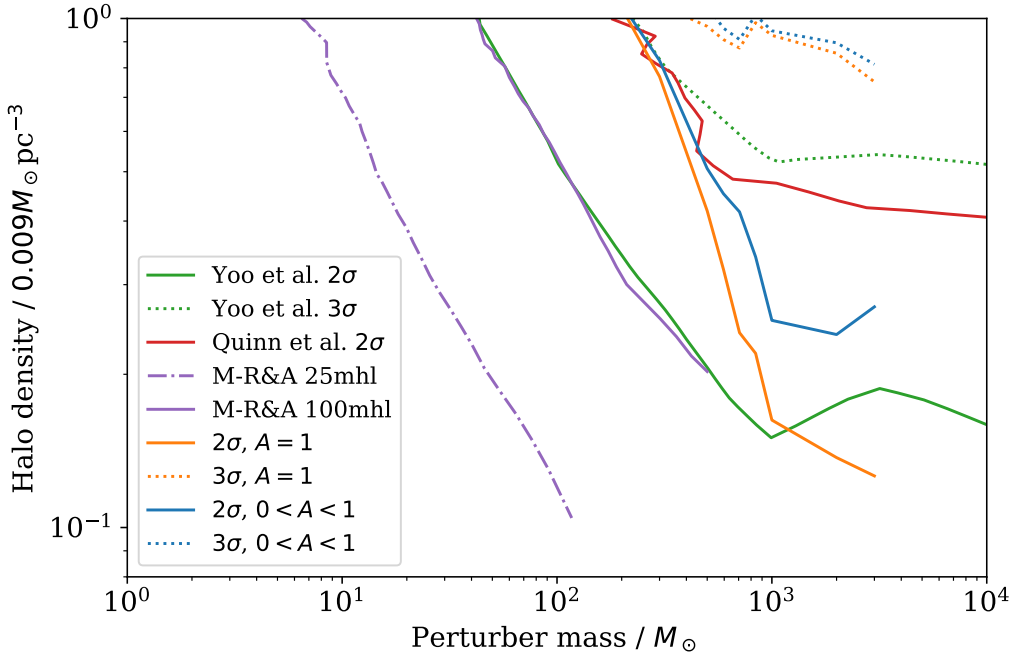

Figure 4.10: As in Fig. 4.9 but our constraints are calculated from the full population of 137 binaries with projected separation larger than 1273au. The green solid and dotted lines are the 2σ and 3σ constraints found by Yoo et al. [84], respectively. The red line is the 2σ constraint calculated by Quinn et al. [85]. The purple dash-dot and solid lines are constraints from Monroy-Rodríguez and Allen [86] for their 25 and 100 most halo-like binaries, respectively. The orange solid and dotted lines are our own 2σ and 3σ constraints from a power law initial semi-major axis distribution. The blue solid and dashed lines are the 2σ and 3σ constraints from our hybrid initial semi-major axis distribution (see text).

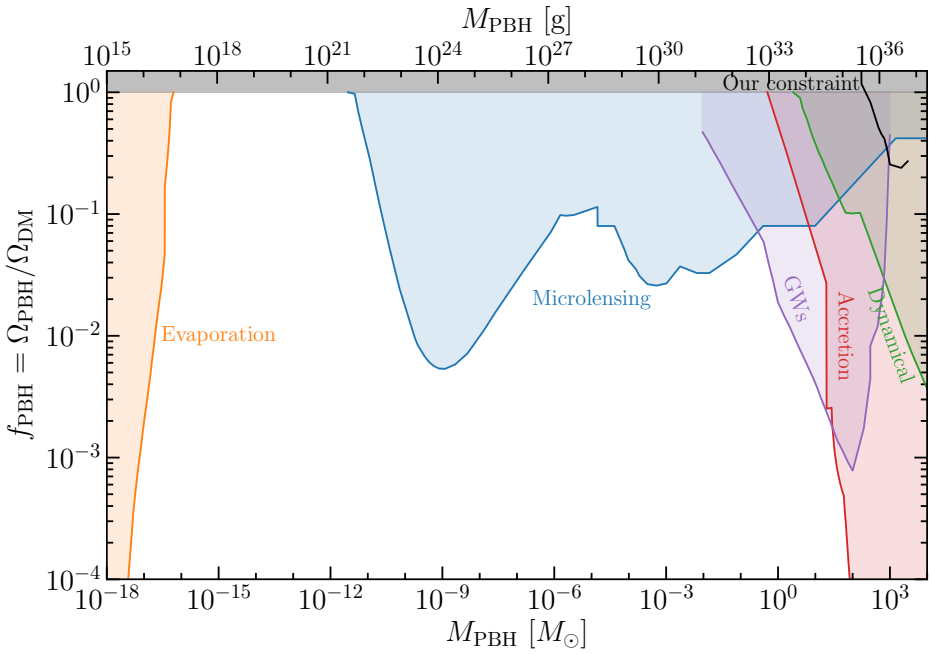

Figure 4.11: From Green and Kavanagh [56] with our own constraint added. A summary of the current constraints on the fraction of dark matter made up of PBHs $f_{\rm PBH}$ as a function of PBH mass $M_{\rm PBH}$. The black line is our own constraint as in Fig. 4.10. The dynamical constraint is the 25 most halo-like constraint from Monroy-Rodríguez and Allen [86]. See Sec. 1.2.2 for more detail about the other constraints.

Chapter 5

Summary

In this chapter I will recap the motivation and methods used in this thesis (Sec. 5.1), summarise the improvements we were able to make to previous work on wide binary disruption (Sec. 5.2), list our main conclusions (Sec. 5.3) and describe a few ways in which our work could be improved or expanded upon (Sec. 5.4).

5.1 This thesis

We set out to find more reliable constraints on the PBH halo fraction following the work of Refs. [39, 85, 86]. Our main goal was to use a physically motivated initial semi-major axis distribution for our wide binary simulations and confirm whether or not any of the previously used approximations need to be replaced by a more accurate method. We used our simulations to confirm the impulse approximation is sufficiently accurate in our parameter space and we tested the necessity of including binaries that break during the simulation. The non-uniform density experienced by halo binaries was taken into account by re-scaling our constraints by the mean time-averaged dark matter density along their Galactic orbits and we used the method of Monroy-Rodríguez and Allen [86] for including the effects of the Galactic disk. Like previous work [Refs. 12, 84–86], we were unable to include the effects of passing stars, the Galactic tide and giant molecular clouds; although the omission of these effects will only make our final constraints more conservative.

Our Monte Carlo simulations implemented encounters using the impulse approximation for impact parameters out to a maximum value that we confirmed is sufficient through convergence testing. Our resulting semi-major axis distributions are in good agreement with previous work when unbound binaries are left out of the simulations, but when left in, unbound and rebound binaries have a significant impact on the final binary population. We were able to produce some of the effects and results from other work and we have provided explanations for any observed differences.

5.2 Improvements we made

We made various improvements on previous approximations, especially the physically motivated initial semi-major axis distribution and the inclusion of unbound binaries. Including unbound binaries increases the number of binaries in the final binary distribution, either because the binaries became rebound after a subsequent encounter or because the binary never had a large enough separation to be removed, consequently the constraints are much weaker. We were able to include all encounters out to a maximum impact parameter where previously the 100 closest encounters have been implemented [84–86] or the further away encounters are simulated as a single diffusive process [101, 102].

We also used improved statistics to compare the observed and simulated binary distributions. Our modified χ^2 test readily gives p-values whilst also providing a measure of the goodness of the best fit. Previous analyses used likelihood analysis, which does not measure the goodness of the best fit, and the K-S test, which has low sensitivity at the extremes of the compared distributions.

5.3 Our conclusion

We calculated our constraints by comparing the observed and simulated projected separations, which reduces the number of random variables introduced

in the comparison to just the orientation of the simulated binaries. We found this to be necessary for our sample size. We compared the projected separations using a modified χ^2 analysis which gives constraints that take into account the quality of the best fit distribution.

Due to the inclusion of unbound binaries and the extra variable parameter in the initial semi-major axis distribution, our constraints are much weaker than those calculated by [e.g. Ref. 86]. Although we did find constraints for the 25 most-halo like binaries, we are not certain that this method accurately takes into account the effect of the Galactic tide. The small sample size might not provide reliable constraints and given more time we would have liked to test this method more thoroughly.

Our final constraints (Fig. 4.11) are much weaker than other dynamical constraints and other constraints in this mass range. The unrealistic initial distribution used in previous studies may have made those constraints erroneously tight. Many of the approximations we made were conservative so more detailed simulations may be required to find tighter constraints.

5.4 Future work

There are many ways our work could be improved. Firstly, with GAIA DR2's radial velocity measurements it should be possible to construct much larger catalogs of halo wide binaries [124]. At this time there is no confirmed sample of halo binaries from GAIA DR2 with a well defined selection function.

Correa-Otto et al. [125] studied the effect of the Galactic tide on binary stars in the solar neighbourhood. They found that the Galactic tide is unlikely to break a binary, but for binaries with semi-major axes greater than $\sim$ 1000au, the tidal forces can lead to a large increase in the binary's eccentricity. Although the effects of the Galactic tide are likely to be weaker for halo binaries, a large increase in binary eccentricity could lead to much more disruptive encounters with PBHs, making this effect potentially important. A more detailed simulation of Galactic dynamics, such as that used by Jiang and

Tremaine [102] would take into account the effect of the Galactic disk, Galactic tidal forces and the non-uniform dark matter density much more accurately than we were able to.

We might have improved our results by comparing observed and simulated populations without binning. The K-S test, which allows comparison of distributions without binning, doesn't provide high levels of sensitivity at the extremes of the distribution but there are modified versions of the K-S test that have a more even sensitivity across the distribution. Likelihood analysis, however, remains unsuitable because it doesn't provide a goodness of fit measure for the best fit parameters.

Another consideration for the future is black hole binaries. Increasing the number of PBHs in PBH binaries would be expected to have a more disruptive effect on halo wide binaries, but current simulations of structure formation with PBH dark matter are as of yet unable to extrapolate the evolution of PBH binaries to the present day [126].

Appendix A

Derivation of the maximum impact parameter

The maximum impact parameter, $b_{\max}$, is derived by requiring that the fractional change in binary energy due to an encounter at $b_{\max}$ is less than a small number δ. We will do this calculation for each term in Eq. (2.25) separately.

Substituting Eq. (2.24) into Eq. (2.25), setting $V_{\rm rel} = \sigma_{\rm rel}$ and neglecting the second term in Eq. (2.25),

$$\Delta\mathcal{E} = \frac{2GM_{\rm p}}{\sigma_{\rm rel}}(\mathbf{V_1} - \mathbf{V_2}) \cdot \left(\frac{\mathbf{b_1}}{b_1^2} - \frac{\mathbf{b_2}}{b_2^2}\right). \tag{A.1}$$

Then since $|\mathcal{E}| = \frac{GM_{\rm b}}{2a}$,

$$\frac{\Delta\mathcal{E}}{|\mathcal{E}|} = \frac{4M_{\rm p}a}{M_{\rm b}\sigma_{\rm rel}}\,(\mathbf{V_1} - \mathbf{V_2}) \cdot \left(\frac{\mathbf{b_1}}{b_1^2} - \frac{\mathbf{b_2}}{b_2^2}\right). \tag{A.2}$$

The maximum difference in orbital velocity of the two stars is,

$$|\mathbf{V_1} - \mathbf{V_2}| = 2\sqrt{\frac{GM_{\rm b}(1-e)}{a(1+e)}} \approx 2\sqrt{\frac{GM_{\rm b}}{a}}. \tag{A.3}$$

The impact parameter vectors which maximise the difference between impact parameters are,

$$\mathbf{b_1} = (b+a)\hat{\mathbf{b}}, \tag{A.4}$$

$$\mathbf{b_2} = b\hat{\mathbf{b}}, \tag{A.5}$$

therefore,

$$\left|\frac{\mathbf{b_1}}{b_1^2} - \frac{\mathbf{b_2}}{b_2^2}\right| = \frac{a}{b(b+a)}. \tag{A.6}$$

Using Cauchy's inequality and Eqs. (A.2), (A.3) and (A.6),

$$\frac{\Delta\mathcal{E}}{|\mathcal{E}|} \leq \frac{8\sqrt{G}M_{\rm p}a^{3/2}}{\sqrt{M_{\rm b}}\sigma_{\rm rel}b(b+a)}. \tag{A.7}$$

Finally, we change this to an equality, relabel $\Delta\mathcal{E}/|\mathcal{E}|$ to δ and relabel b to $b_{\rm max}$,

$$\delta = \frac{8\sqrt{G}M_{\rm p}a^{3/2}}{\sqrt{M_{\rm b}}\sigma_{\rm rel}b_{\rm max}(b_{\rm max}+a)}, \tag{A.8}$$

which has solutions,

$$b_{\rm max} = -\frac{a}{2} \pm \sqrt{\frac{a^2}{4} + 8G^{\frac{1}{2}}M_{\rm p}M_{\rm b}^{-\frac{1}{2}}a^{\frac{3}{2}}\sigma_{\rm rel}^{-1}\delta^{-1}}. \tag{A.9}$$

By substituting in typical values ($M_{\rm p} = 1M_{\odot}$, $M_{\rm b} = 1M_{\odot}$, $a = 10^4$au, $\sigma_{\rm rel} = 220$km s^{-1}), we find that the second term in the square root is much larger than the first. Neglecting the $a/2$ terms,

$$b_{\rm max} = \left(\frac{64GM_{\rm p}^2a^3}{M_{\rm b}\sigma_{\rm rel}^2\delta^2}\right)^{\frac{1}{4}}. \tag{A.10}$$

For the second term in Eq. (2.25), following the same procedure we find,

$$b_{\rm max} = \left(\frac{4GM_{\rm p}^2a^3}{M_{\rm b}\sigma_{\rm rel}^2\delta}\right)^{\frac{1}{4}}. \tag{A.11}$$

The only differences between Eqs. (A.10) and (A.11) are the prefactor and the dependence on δ. In our simulations we use Eq. (A.10) since this is the larger value.

Bibliography

[1] J. H. Oort, "The force exerted by the stellar system in the direction perpendicular to the galactic plane and some related problems", *Bull. Astron. Inst. Netherlands* **6** August (1932) 249.

[2] F. Zwicky, "Die Rotverschiebung von extragalaktischen Nebeln", *Helvetica Physica Acta* **6** January (1933) 110–127.

[3] S. Smith, "The Mass of the Virgo Cluster", *ApJ* **83** January (1936) 23.

[4] A. Czarnecki, W. J. Marciano, and A. Sirlin, "Neutron Lifetime and Axial Coupling Connection", *Phys. Rev. Lett.* **120** May (2018) 202002, arXiv:1802.01804.

[5] V. Springel, "The cosmological simulation code GADGET-2", *MNRAS* **364** December (2005) 1105–1134, arXiv:astro-ph/0505010.

[6] M. Vogelsberger, S. Genel, V. Springel, P. Torrey, D. Sijacki, D. Xu, G. Snyder, S. Bird, D. Nelson, and L. Hernquist, "Properties of galaxies reproduced by a hydrodynamic simulation", *Nature* **509** May (2014) 177–182, arXiv:1405.1418.

[7] G. R. Blumenthal, S. M. Faber, J. R. Primack, and M. J. Rees, "Formation of galaxies and large-scale structure with cold dark matter.", *Nature* **311** October (1984) 517–525.

[8] M. Davis, G. Efstathiou, C. S. Frenk, and S. D. M. White, "The evolution of large-scale structure in a Universe dominated by cold dark matter", *ApJ* **292** May (1985) 371–394.

[9] V. C. Rubin and W. K. J. Ford, "Rotation of the Andromeda Nebula from a Spectroscopic Survey of Emission Regions", *ApJ* **159** February (1970) 379.

[10] K. C. Freeman, "On the Disks of Spiral and S0 Galaxies", *ApJ* **160** June (1970) 811.

[11] J. P. Ostriker and P. J. E. Peebles, "A Numerical Study of the Stability of Flattened Galaxies: or, can Cold Galaxies Survive?", *ApJ* **186** December (1973) 467–480.

[12] J. Binney and S. Tremaine, "Galactic dynamics", Princeton University Press, second ed., 2008.

[13] B. Ryden, "Introduction to cosmology", Cambridge University Press, 2016.

[14] A. H. Gonzalez, S. Sivanandam, A. I. Zabludoff, and D. Zaritsky, "Galaxy Cluster Baryon Fractions Revisited", *ApJ* **778** November (2013) 14, arXiv:1309.3565.

[15] J. A. Tyson, G. P. Kochanski, and I. P. Dell'Antonio, "Detailed Mass Map of CL 0024+1654 from Strong Lensing", *ApJ* **498** May (1998) L107–L110, arXiv:astro-ph/9801193.

[16] D. Clowe, M. Bradač, A. H. Gonzalez, M. Markevitch, S. W. Randall, C. Jones, and D. Zaritsky, "A Direct Empirical Proof of the Existence of Dark Matter", *ApJ* **648** September (2006) L109–L113, arXiv:astro-ph/0608407.

[17] Planck Collaboration, "Planck 2018 results. VI. Cosmological parameters", *A&A* **641** September (2020) A6, arXiv:1807.06209.

[18] DES Collaboration, "Dark Energy Survey Year 3 Results: Cosmological Constraints from Galaxy Clustering and Weak Lensing", *arXiv e-prints* May 2021 arXiv:2105.13549, arXiv:2105.13549.

[19] C. Hikage, M. Oguri, T. Hamana, S. More, R. Mandelbaum, M. Takada, F. Köhlinger, H. Miyatake, A. J. Nishizawa, H. Aihara, R. Armstrong, J. Bosch, J. Coupon, A. Ducout, P. Ho, B.-C. Hsieh, Y. Komiyama, F. Lanusse, A. Leauthaud, R. H. Lupton, E. Medezinski, S. Mineo, S. Miyama, S. Miyazaki, R. Murata, H. Murayama, M. Shirasaki, C. Sifón, M. Simet, J. Speagle, D. N. Spergel, M. A. Strauss, N. Sugiyama, M. Tanaka, Y. Utsumi, S.-Y. Wang, and Y. Yamada, "Cosmology from cosmic shear power spectra with Subaru Hyper Suprime-Cam first-year data", *PASJ* **71** April (2019) 43, arXiv:1809.09148.

[20] C. Heymans, T. Tröster, M. Asgari, C. Blake, H. Hildebrandt, B. Joachimi, K. Kuijken, C.-A. Lin, A. G. Sánchez, J. L. van den Busch, A. H. Wright, A. Amon, M. Bilicki, J. de Jong, M. Crocce, A. Dvornik, T. Erben, M. C. Fortuna, F. Getman, B. Giblin, K. Glazebrook, H. Hoekstra, S. Joudaki, A. Kannawadi, F. Köhlinger, C. Lidman, L. Miller, N. R. Napolitano, D. Parkinson, P. Schneider, H. Shan, E. A. Valentijn, G. Verdoes Kleijn, and C. Wolf, "KiDS-1000 Cosmology: Multi-probe weak gravitational lensing and spectroscopic galaxy clustering constraints", *A&A* **646** February (2021) A140, arXiv:2007.15632.

[21] K. S. Dawson, J.-P. Kneib, W. J. Percival, S. Alam, F. D. Albareti, S. F. Anderson, E. Armengaud, É. Aubourg, S. Bailey, J. E. Bautista, A. A. Berlind, M. A. Bershady, F. Beutler, D. Bizyaev, M. R. Blanton, M. Blomqvist, A. S. Bolton, J. Bovy, W. N. Brandt, J. Brinkmann, J. R. Brownstein, E. Burtin, N. G. Busca, Z. Cai, C.-H. Chuang, N. Clerc, J. Comparat, F. Cope, R. A. C. Croft, I. Cruz-Gonzalez, L. N. da Costa, M.-C. Cousinou, J. Darling, A. de la Macorra, S. de la

Torre, T. Delubac, H. du Mas des Bourboux, T. Dwelly, A. Ealet, D. J. Eisenstein, M. Eracleous, S. Escoffier, X. Fan, A. Finoguenov, A. Font-Ribera, P. Frinchaboy, P. Gaulme, A. Georgakakis, P. Green, H. Guo, J. Guy, S. Ho, D. Holder, J. Huehnerhoff, T. Hutchinson, Y. Jing, E. Jullo, V. Kamble, K. Kinemuchi, D. Kirkby, F.-S. Kitaura, M. A. Klaene, R. R. Laher, D. Lang, P. Laurent, J.-M. Le Goff, C. Li, Y. Liang, M. Lima, Q. Lin, W. Lin, Y.-T. Lin, D. C. Long, B. Lundgren, N. MacDonald, M. A. Geimba Maia, E. Malanushenko, V. Malanushenko, V. Mariappan, C. K. McBride, I. D. McGreer, B. Ménard, A. Merloni, A. Meza, A. D. Montero-Dorta, D. Muna, A. D. Myers, K. Nandra, T. Naugle, J. A. Newman, P. Noterdaeme, P. Nugent, R. Ogando, M. D. Olmstead, A. Oravetz, D. J. Oravetz, N. Padmanabhan, N. Palanque-Delabrouille, K. Pan, J. K. Parejko, I. Pâris, J. A. Peacock, P. Petitjean, M. M. Pieri, A. Pisani, F. Prada, A. Prakash, A. Raichoor, B. Reid, J. Rich, J. Ridl, S. Rodriguez-Torres, A. Carnero Rosell, A. J. Ross, G. Rossi, J. Ruan, M. Salvato, C. Sayres, D. P. Schneider, D. J. Schlegel, U. Seljak, H.-J. Seo, B. Sesar, S. Shandera, Y. Shu, A. Slosar, F. Sobreira, A. Streblyanska, N. Suzuki, D. Taylor, C. Tao, J. L. Tinker, R. Tojeiro, M. Vargas-Magaña, Y. Wang, B. A. Weaver, D. H. Weinberg, M. White, W. M. Wood-Vasey, C. Yeche, Z. Zhai, C. Zhao, G.-b. Zhao, Z. Zheng, G. Ben Zhu, and H. Zou, "The SDSS-IV Extended Baryon Oscillation Spectroscopic Survey: Overview and Early Data", *AJ* **151** February (2016) 44, arXiv:1508.04473.

[22] D. J. Bacon, A. R. Refregier, and R. S. Ellis, "Detection of weak gravitational lensing by large-scale structure", *MNRAS* **318** October (2000) 625–640, arXiv:astro-ph/0003008.

[23] S. Joudaki, C. Blake, A. Johnson, A. Amon, M. Asgari, A. Choi, T. Erben, K. Glazebrook, J. Harnois-Déraps, C. Heymans, H. Hildebrandt, H. Hoekstra, D. Klaes, K. Kuijken, C. Lidman, A. Mead, L. Miller, D. Parkinson, G. B. Poole, P. Schneider, M. Viola, and C. Wolf, "KiDS-450 + 2dFLenS: Cosmological parameter constraints from weak gravitational lensing tomography and overlapping redshift-space galaxy clustering", *MNRAS* **474** March (2018) 4894–4924, arXiv:1707.06627.

[24] P. J. E. Peebles and M. G. Hauser, "Statistical Analysis of Catalogs of Extragalactic Objects. III. The Shane-Wirtanen and Zwicky Catalogs", *ApJS* **28** November (1974) 19.

[25] B. Hadzhiyska, C. García-García, D. Alonso, A. Nicola, and A. Slosar, "Hefty enhancement of cosmological constraints from the DES Y1 data using a hybrid effective field theory approach to galaxy bias", *J. Cosmology Astropart. Phys.* **2021** September (2021) 020, arXiv:2103.09820.

[26] T. G. Brainerd, R. D. Blandford, and I. Smail, "Weak Gravitational Lensing by Galaxies", *ApJ* **466** August (1996) 623, arXiv:astro-ph/9503073.

[27] B. Bertotti, L. Iess, and P. Tortora, "A test of general relativity using radio links with the Cassini spacecraft", *Nature* **425** September (2003) 374–376.

[28] M. Milgrom, "A modification of the Newtonian dynamics as a possible alternative to the hidden mass hypothesis.", *ApJ* **270** July (1983) 365–370.

[29] W. J. G. de Blok, "The Core-Cusp Problem", *Advances in Astronomy* **2010** January (2010) 789293, arXiv:0910.3538.

[30] E. F. Bell, D. H. McIntosh, N. Katz, and M. D. Weinberg, "A First Estimate of the Baryonic Mass Function of Galaxies", *ApJ* **585** March (2003) L117–L120, arXiv:astro-ph/0301616.

[31] K.-H. Chae, F. Lelli, H. Desmond, S. S. McGaugh, P. Li, and J. M. Schombert, "Testing the Strong Equivalence Principle: Detection of the External Field Effect in Rotationally Supported Galaxies", *ApJ* **904** November (2020) 51, arXiv:2009.11525.

[32] S. S. McGaugh, "A tale of two paradigms: the mutual incommensurability of ΛCDM and MOND", *Canadian Journal of Physics* **93** February (2015) 250–259, arXiv:1404.7525.

[33] M. Milgrom, "The MOND paradigm of modified dynamics", *Scholarpedia* **9** June (2014) 31410.

[34] B. Famaey and S. S. McGaugh, "Modified Newtonian Dynamics (MOND): Observational Phenomenology and Relativistic Extensions", *Living Reviews in Relativity* **15** September (2012) 10, arXiv:1112.3960.

[35] J. D. Bekenstein, "Relativistic gravitation theory for the modified Newtonian dynamics paradigm", *Phys. Rev. D* **70** October (2004) 083509, arXiv:astro-ph/0403694.

[36] V. Savchenko, C. Ferrigno, E. Kuulkers, A. Bazzano, E. Bozzo, S. Brandt, J. Chenevez, T. J. L. Courvoisier, R. Diehl, A. Domingo, L. Hanlon, E. Jourdain, A. von Kienlin, P. Laurent, F. Lebrun, A. Lutovinov, A. Martin-Carrillo, S. Mereghetti, L. Natalucci, J. Rodi, J. P. Roques, R. Sunyaev, and P. Ubertini, "INTEGRAL Detection of the First Prompt Gamma-Ray Signal Coincident with the Gravitational-wave Event GW170817", *ApJ* **848** October (2017) L15, arXiv:1710.05449.

[37] A. Goldstein, P. Veres, E. Burns, M. S. Briggs, R. Hamburg, D. Kocevski, C. A. Wilson-Hodge, R. D. Preece, S. Poolakkil, O. J. Roberts, C. M. Hui, V. Connaughton, J. Racusin, A. von Kienlin, T. Dal Canton, N. Christensen, T. Littenberg, K. Siellez, L. Blackburn, J. Broida, E. Bissaldi, W. H. Cleveland, M. H. Gibby, M. M. Giles, R. M. Kippen, S. McBreen, J. McEnery, C. A. Meegan, W. S. Paciesas, and M. Stanbro, "An Ordinary Short Gamma-Ray Burst with

Extraordinary Implications: Fermi-GBM Detection of GRB 170817A", *ApJ* **848** October (2017) L14, arXiv:1710.05446.

[38] C. Skordis and T. Złośnik, "Gravitational alternatives to dark matter with tensor mode speed equaling the speed of light", *Phys. Rev. D* **100** November (2019) 104013, arXiv:1905.09465.

[39] J. N. Bahcall, P. Hut, and S. Tremaine, "Maximum mass of objects that constitute unseen disk material", *ApJ* **290** March (1985) 15–20.

[40] LIGO Scientific Collaboration and Virgo Collaboration, "Observation of Gravitational Waves from a Binary Black Hole Merger", *Phys. Rev. Lett.* **116** February (2016) 061102, arXiv:1602.03837.

[41] LIGO Scientific Collaboration and VIRGO Collaboration, "GW151226: Observation of Gravitational Waves from a 22-Solar-Mass Binary Black Hole Coalescence", *Phys. Rev. Lett.* **116** June (2016) 241103, arXiv:1606.04855.

[42] M. Sasaki, T. Suyama, T. Tanaka, and S. Yokoyama, "Primordial Black Hole Scenario for the Gravitational-Wave Event GW150914", *Phys. Rev. Lett.* **117** August (2016) 061101, arXiv:1603.08338.

[43] S. Wolfram, "Abundances of new stable particles produced in the early Universe", *Physics Letters B* **82** March (1979) 65–68.

[44] M. Srednicki, R. Watkins, and K. A. Olive, "Calculations of relic densities in the early Universe", *Nuclear Physics B* **310** December (1988) 693–713.

[45] R. J. Scherrer and M. S. Turner, "On the relic, cosmic abundance of stable, weakly interacting massive particles", *Phys. Rev. D* **33** March (1986) 1585–1589.

[46] P. Gondolo and G. Gelmini, "Cosmic abundances of stable particles: improved analysis.", *Nuclear Physics B* **360** August (1991) 145–179.

[47] G. Jungman, M. Kamionkowski, and K. Griest, "Supersymmetric dark matter", *Phys. Rep.* **267** March (1996) 195–373, arXiv:hep-ph/9506380.

[48] G. Arcadi, M. Dutra, P. Ghosh, M. Lindner, Y. Mambrini, M. Pierre, S. Profumo, and F. S. Queiroz, "The waning of the WIMP? A review of models, searches, and constraints", *European Physical Journal C* **78** March (2018) 203, arXiv:1703.07364.

[49] G. Drexlin, V. Hannen, S. Mertens, and C. Weinheimer, "Current Direct Neutrino Mass Experiments", *arXiv e-prints* June 2013 arXiv:1307.0101, arXiv:1307.0101.

[50] J. Lesgourgues and S. Pastor, "Neutrino cosmology and Planck", *New Journal of Physics* **16** June (2014) 065002, arXiv:1404.1740.

[51] S. Vagnozzi, E. Giusarma, O. Mena, K. Freese, M. Gerbino, S. Ho, and M. Lattanzi, "Unveiling ν secrets with cosmological data: Neutrino masses and mass hierarchy", *Phys. Rev. D* **96** December (2017) 123503, arXiv:1701.08172.

[52] B. Shakya, "Sterile neutrino dark matter from freeze-in", *Modern Physics Letters A* **31** January (2016) 1630005, arXiv:1512.02751.

[53] W. Enzi, R. Murgia, O. Newton, S. Vegetti, C. Frenk, M. Viel, M. Cautun, C. D. Fassnacht, M. Auger, G. Despali, J. McKean, L. V. E. Koopmans, and M. Lovell, "Joint constraints on thermal relic dark matter from strong gravitational lensing, the Ly α forest, and Milky Way satellites", *MNRAS* **506** October (2021) 5848–5862, arXiv:2010.13802.

[54] G. G. Raffelt, "Axions in astrophysics and cosmology", in "Proceedings of the XVth Moriond workshop". February 1995. hep-ph/9502358.

[55] F. Chadha-Day, J. Ellis, and D. J. E. Marsh, "Axion Dark Matter: What is it and Why Now?", *arXiv e-prints* May 2021 arXiv:2105.01406, arXiv:2105.01406.

[56] A. M. Green and B. J. Kavanagh, "Primordial black holes as a dark matter candidate", *Journal of Physics G Nuclear Physics* **48** April (2021) 043001, arXiv:2007.10722.

[57] B. Carr, K. Kohri, Y. Sendouda, and J. Yokoyama, "Constraints on Primordial Black Holes", *arXiv e-prints* February 2020 arXiv:2002.12778.

[58] B. Carr, F. Kühnel, and M. Sandstad, "Primordial black holes as dark matter", *Phys. Rev. D* **94** October (2016) 083504, arXiv:1607.06077.

[59] B. Carr and F. Kühnel, "Primordial Black Holes as Dark Matter: Recent Developments", *Annual Review of Nuclear and Particle Science* **70** October (2020) 355–394, arXiv:2006.02838.

[60] B. J. Carr, "The primordial black hole mass spectrum.", *ApJ* **201** October (1975) 1–19.

[61] D. K. Nadezhin, I. D. Novikov, and A. G. Polnarev, "The hydrodynamics of primordial black hole formation", *Soviet Ast.* **22** April (1978) 129–138.

[62] B. J. Carr and J. E. Lidsey, "Primordial black holes and generalized constraints on chaotic inflation", *Phys. Rev. D* **48** July (1993) 543–553.

[63] D. N. Page, "Particle emission rates from a black hole: Massless particles from an uncharged, nonrotating hole", *Phys. Rev. D* **13** January (1976) 198–206.

[64] J. H. MacGibbon, B. J. Carr, and D. N. Page, "Do evaporating black holes form photospheres?", *Phys. Rev. D* **78** Sep (2008) 064043, arXiv:0709.2380.

[65] D. N. Page and S. W. Hawking, "Gamma rays from primordial black holes", *ApJ* **206** May (1976) 1–7.

[66] V. Poulin, J. Lesgourgues, and P. D. Serpico, "Cosmological constraints on exotic injection of electromagnetic energy", *J. Cosmology Astropart. Phys.* **2017** March (2017) 043, arXiv:1610.10051.

[67] S. J. Clark, B. Dutta, Y. Gao, L. E. Strigari, and S. Watson, "Planck constraint on relic primordial black holes", *Phys. Rev. D* **95** April (2017) 083006, arXiv:1612.07738.

[68] S. J. Clark, B. Dutta, Y. Gao, Y.-Z. Ma, and L. E. Strigari, "21 cm limits on decaying dark matter and primordial black holes", *Phys. Rev. D* **98** August (2018) 043006, arXiv:1803.09390.

[69] H. Kim, "A constraint on light primordial black holes from the interstellar medium temperature", *MNRAS* **504** July (2021) 5475–5484, arXiv:2007.07739.

[70] B. J. Carr, K. Kohri, Y. Sendouda, and J. Yokoyama, "New cosmological constraints on primordial black holes", *Phys. Rev. D* **81** May (2010) 104019, arXiv:0912.5297.

[71] G. Ballesteros, J. Coronado-Blázquez, and D. Gaggero, "X-ray and gamma-ray limits on the primordial black hole abundance from Hawking radiation", *Physics Letters B* **808** September (2020) 135624, arXiv:1906.10113.

[72] EROS-2 Collaboration, "Limits on the Macho content of the Galactic Halo from the EROS-2 Survey of the Magellanic Clouds", *A&A* **469** July (2007) 387–404, arXiv:astro-ph/0607207.

[73] C. Alcock, R. A. Allsman, D. R. Alves, T. S. Axelrod, A. C. Becker, D. P. Bennett, K. H. Cook, N. Dalal, A. J. Drake, K. C. Freeman, M. Geha, K. Griest, M. J. Lehner, S. L. Marshall, D. Minniti, C. A. Nelson, B. A. Peterson, P. Popowski, M. R. Pratt, P. J. Quinn, C. W. Stubbs, W. Sutherland, A. B. Tomaney, T. Vandehei, and D. L. Welch, "MACHO Project Limits on Black Hole Dark Matter in the 1-30 $M_{\odot}$ Range", *ApJ* **550** April (2001) L169–L172, arXiv:astro-ph/0011506.

[74] H. Niikura, M. Takada, S. Yokoyama, T. Sumi, and S. Masaki, "Constraints on Earth-mass primordial black holes from OGLE 5-year microlensing events", *Phys. Rev. D* **99** April (2019) 083503, arXiv:1901.07120.

[75] P. Mróz, A. Udalski, J. Skowron, R. Poleski, S. Kozłowski, M. K. Szymański, I. Soszyński, Ł. Wyrzykowski, P. Pietrukowicz, K. Ulaczyk, D. Skowron, and M. Pawlak, "No large population of unbound or wide-orbit Jupiter-mass planets", *Nature* **548** August (2017) 183–186, arXiv:1707.07634.

[76] H. Niikura, M. Takada, N. Yasuda, R. H. Lupton, T. Sumi, S. More, T. Kurita, S. Sugiyama, A. More, M. Oguri, and M. Chiba, "Microlensing constraints on primordial black holes with Subaru/HSC Andromeda observations", *Nature Astronomy* **3** Apr (2019) 524–534, arXiv:1701.02151.

[77] N. Smyth, S. Profumo, S. English, T. Jeltema, K. McKinnon, and P. Guhathakurta, "Updated constraints on asteroid-mass primordial black holes as dark matter", *Phys. Rev. D* **101** March (2020) 063005, arXiv:1910.01285.

[78] LIGO Scientific Collaboration and Virgo Collaboration, "Observation of Gravitational Waves from a Binary Black Hole Merger", *Phys. Rev. Lett.* **116** February (2016) 061102, arXiv:1602.03837.

[79] T. Nakamura, M. Sasaki, T. Tanaka, and K. S. Thorne, "Gravitational Waves from Coalescing Black Hole MACHO Binaries", *ApJ* **487** October (1997) L139–L142, arXiv:astro-ph/9708060.

[80] K. Ioka, T. Chiba, T. Tanaka, and T. Nakamura, "Black hole binary formation in the expanding Universe: Three body problem approximation", *Phys. Rev. D* **58** September (1998) 063003, arXiv:astro-ph/9807018.

[81] B. J. Kavanagh, D. Gaggero, and G. Bertone, "Merger rate of a subdominant population of primordial black holes", *Phys. Rev. D* **98** July (2018) 023536, arXiv:1805.09034.

[82] K. Hayasaki, K. Takahashi, Y. Sendouda, and S. Nagataki, "Rapid merger of binary primordial black holes: An implication for GW150914", *PASJ* **68** August (2016) 66, arXiv:0909.1738.

[83] Y. Ali-Haïmoud, E. D. Kovetz, and M. Kamionkowski, "Merger rate of primordial black-hole binaries", *Phys. Rev. D* **96** December (2017) 123523, arXiv:1709.06576.

[84] J. Yoo, J. Chanamé, and A. Gould, "The End of the MACHO Era: Limits on Halo Dark Matter from Stellar Halo Wide Binaries", *ApJ* **601** January (2004) 311–318, arXiv:astro-ph/0307437.

[85] D. P. Quinn, M. I. Wilkinson, M. J. Irwin, J. Marshall, A. Koch, and V. Belokurov, "On the reported death of the MACHO era", *MNRAS* **396** June (2009) L11–L15, arXiv:0903.1644.

[86] M. A. Monroy-Rodríguez and C. Allen, "The End of the MACHO Era, Revisited: New Limits on MACHO Masses from Halo Wide Binaries", *ApJ* **790** August (2014) 159, arXiv:1406.5169.

[87] T. D. Brandt, "Constraints on MACHO Dark Matter from Compact Stellar Systems in Ultra-faint Dwarf Galaxies", *ApJ* **824** June (2016) L31, arXiv:1605.03665.

[88] S. M. Koushiappas and A. Loeb, "Dynamics of Dwarf Galaxies Disfavor Stellar-Mass Black Holes as Dark Matter", *Phys. Rev. Lett.* **119** Jul (2017) 041102, arXiv:1704.01668.

[89] N. Afshordi, P. McDonald, and D. N. Spergel, "Primordial Black Holes as Dark Matter: The Power Spectrum and Evaporation of Early Structures", *ApJ* **594** September (2003) L71–L74, arXiv:astro-ph/0302035.

[90] R. Murgia, G. Scelfo, M. Viel, and A. Raccanelli, "Lyman-α Forest Constraints on Primordial Black Holes as Dark Matter", *Phys. Rev. Lett.* **123** August (2019) 071102, arXiv:1903.10509.

[91] V. Poulin, P. D. Serpico, F. Calore, S. Clesse, and K. Kohri, "CMB bounds on disk-accreting massive primordial black holes", *Phys. Rev. D* **96** October (2017) 083524, arXiv:1707.04206.

[92] P. D. Serpico, V. Poulin, D. Inman, and K. Kohri, "Cosmic microwave background bounds on primordial black holes including dark matter halo accretion", *Physical Review Research* **2** May (2020) 023204, arXiv:2002.10771.

[93] A. Hektor, G. Hütsi, L. Marzola, M. Raidal, V. Vaskonen, and H. Veermäe, "Constraining primordial black holes with the EDGES 21-cm absorption signal", *Phys. Rev. D* **98** July (2018) 023503, arXiv:1803.09697.

[94] Y. Ali-Haïmoud and M. Kamionkowski, "Cosmic microwave background limits on accreting primordial black holes", *Phys. Rev. D* **95** Feb (2017) 043534, arXiv:1612.05644.

[95] Y. Tada and S. Yokoyama, "Primordial black holes as biased tracers", *Phys. Rev. D* **91** June (2015) 123534, arXiv:1502.01124.

[96] S. Young and C. T. Byrnes, "Signatures of non-gaussianity in the isocurvature modes of primordial black hole dark matter", *J. Cosmology Astropart. Phys.* **2015** April (2015) 034, arXiv:1503.01505.

[97] T. Suyama and S. Yokoyama, "Clustering of primordial black holes with non-Gaussian initial fluctuations", *Progress of Theoretical and Experimental Physics* **2019** October (2019) 103E02, arXiv:1906.04958.

[98] J. C. Niemeyer and K. Jedamzik, "Near-Critical Gravitational Collapse and the Initial Mass Function of Primordial Black Holes", *Phys. Rev. Lett.* **80** June (1998) 5481–5484, arXiv:astro-ph/9709072.

[99] J. C. Niemeyer and K. Jedamzik, "Dynamics of primordial black hole formation", *Phys. Rev. D* **59** June (1999) 124013, arXiv:astro-ph/9901292.

[100] C. D. Murray and S. F. Dermott, "Solar system dynamics", Cambridge University Press, 2000.

[101] M. D. Weinberg, S. L. Shapiro, and I. Wasserman, "The Dynamical Fate of Wide Binaries in the Solar Neighborhood", *ApJ* **312** January (1987) 367.

[102] Y.-F. Jiang and S. Tremaine, "The evolution of wide binary stars", *MNRAS* **401** January (2010) 977–994, arXiv:0907.2952.

[103] J. Chanamé and A. Gould, "Disk and Halo Wide Binaries from the Revised Luyten Catalog: Probes of Star Formation and MACHO Dark Matter", *ApJ* **601** January (2004) 289–310, arXiv:astro-ph/0307434.

[104] W. J. Luyten, "New Luyten catalogue of stars with proper motions larger than two tenths of an arcsecond; and first supplement; NLTT.", Minneapolis 1979, 1979.

[105] W. J. Luyten and H. S. Hughes, "Proper motion survey with the forty-eight inch Schmidt telescope. LV. First supplement to the NLTT catalogue.", *Proper Motion Survey, University of Minnesota* **55** January (1980) 1.

[106] C. Allen and M. A. Monroy-Rodríguez, "An Improved Catalog of Halo Wide Binary Candidates", *ApJ* **790** August (2014) 158, arXiv:1406.5164.

[107] W. Dehnen and J. I. Read, "N-body simulations of gravitational dynamics", *European Physical Journal Plus* **126** May (2011) 55, arXiv:1105.1082.

[108] W. Dehnen and J. Binney, "Mass models of the Milky Way", *MNRAS* **294** March (1998) 429–438, arXiv:astro-ph/9612059.

[109] C. Allen and A. Santillan, "An improved model of the galactic mass distribution for orbit computations.", *Revista Mexicana de Astronomía y Astrofísica* **22** October (1991) 255.

[110] J. Bovy, "galpy: A python Library for Galactic Dynamics", *ApJS* **216** February (2015) 29, arXiv:1412.3451.

[111] A.-C. Eilers, D. W. Hogg, H.-W. Rix, and M. K. Ness, "The Circular Velocity Curve of the Milky Way from 5 to 25 kpc", *ApJ* **871** January (2019) 120, arXiv:1810.09466.

[112] W. H. Press, S. A. Teukolsky, W. T. Vetterling, and B. P. Flannery, "Numerical recipes in C++ : the art of scientific computing", Cambridge University Press, 2002.

[113] M. B. N. Kouwenhoven, S. P. Goodwin, R. J. Parker, M. B. Davies, D. Malmberg, and P. Kroupa, "The formation of very wide binaries during the star cluster dissolution phase", *MNRAS* **404** June (2010) 1835–1848, arXiv:1001.3969.

[114] M. Valtonen, "Wide Binaries from Few-Body Interactions", *Celestial Mechanics and Dynamical Astronomy* **68** May (1997) 27–41.

[115] A. Poveda, C. Allen, and A. Hernández-Alcántara, "The Frequency Distribution of Semimajor Axes of Wide Binaries: Cosmogony and Dynamical Evolution", in "Binary Stars as Critical Tools & Tests in Contemporary Astrophysics", W. I. Hartkopf, P. Harmanec, and E. F. Guinan, eds., vol. 240, pp. 417–425. August 2007. arXiv:0705.2021.

[116] D. Griffiths, "The dynamical evolution of young stellar regions", PhD thesis, University of Sheffield, Sheffield, UK. https://ethos.bl.uk/OrderDetails.do?uin=uk.bl.ethos.772874, September 2019.

[117] G. Duchêne and A. Kraus, "Stellar Multiplicity", *ARA&A* **51** August (2013) 269–310, arXiv:1303.3028.

[118] P. F. de Salas and A. Widmark, "Dark matter local density determination: recent observations and future prospects", *Reports on Progress in Physics* **84** October (2021) 104901, arXiv:2012.11477.

[119] L. B. Lucy, "Hypothesis testing for meagre data sets", *MNRAS* **318** October (2000) 92–100.

[120] C. Allen, A. Poveda, and M. A. Herrera, "Wide binaries among high-velocity and metal-poor stars", *A&A* **356** April (2000) 529–540.

[121] M. R. Zapatero Osorio and E. L. Martín, "A CCD imaging search for wide metal-poor binaries", *A&A* **419** May (2004) 167–180, arXiv:astro-ph/0402310.

[122] S. G. Ryan, "Halo Common Proper Motion Stars: Subdwarf Distance Scale, Halo Binary Fraction, and UBVRI Colors", *AJ* **104** September (1992) 1144.

[123] M. Wenger, F. Ochsenbein, D. Egret, P. Dubois, F. Bonnarel, S. Borde, F. Genova, G. Jasniewicz, S. Laloë, S. Lesteven, and R. Monier, "The SIMBAD astronomical database. The CDS reference database for astronomical objects", *A&AS* **143** April (2000) 9–22, arXiv:astro-ph/0002110.

[124] Gaia Collaboration, "Gaia Data Release 2. Summary of the contents and survey properties", *A&A* **616** August (2018) A1, arXiv:1804.09365.

[125] J. A. Correa-Otto, M. F. Calandra, and R. A. Gil-Hutton, "A new insight into the Galactic potential: A simple secular model for the evolution of binary systems in the solar neighbourhood", *A&A* **600** April (2017) A59, arXiv:1703.04694.

[126] D. Inman and Y. Ali-Haïmoud, "Early structure formation in primordial black hole cosmologies", *Phys. Rev. D* **100** October (2019) 083528, arXiv:1907.08129.